

Design, Fabrication, and Characterization of a 2-D SOI MEMS Micromirror with Sidewall Electrodes for Confocal MACROscope Imaging

by

Yanhui Bai

A thesis
presented to the University of Waterloo
in fulfillment of the
thesis requirement for the degree of
Doctor of Philosophy
in
Systems Design Engineering

Waterloo, Ontario, Canada, 2010

©Yanhui Bai 2010

I hereby declare that I am the sole author of this thesis. This is a true copy of the thesis, including any required final revisions, as accepted by my examiners.

I understand that my thesis may be made electronically available to the public.

Yanhui Bai

Abstract

Micro-Electro-Mechanical Systems (MEMS) micromirrors have been developed for more than two decades along with the development of MEMS technology. They have been used into many application fields: optical switches, digital light projector (DLP), adoptive optics (AO), high definition (HD) display, barcode reader, endoscopic optical coherence tomography (OCT) and confocal microscope, and so on. Especially, MEMS mirrors applied into endoscopic OCT and confocal microscope are the intensive research field. Various actuation mechanisms, such as electrostatic, electromagnetic, electro bimorph thermal, electrowetting, piezoelectric (PZT) and hybrid actuators, are adopted by different types of micromirrors. Among these actuators, the electrostatic is easily understood and simple to realize, therefore, it is broadly adopted by a large number of micromirrors.

This thesis reports the design, fabrication, and characterization of a 2-D Silicon-on-insulation (SOI) MEMS micromirror with sidewall (SW) electrodes for endoscopic OCT or confocal microscope imaging. The biaxial MEMS mirror with SW electrodes is actuated by electrostatic actuators. The dimension of mirror plate is $1000\mu\text{m}\times 1000\mu\text{m}$, with a thickness of a $35\mu\text{m}$. The analytical modeling of SW electrodes, fabrication process, and performance characteristics are described. In comparison to traditional electrostatic actuators, parallel-plate and comb-drive, SW electrodes combined with bottom electrodes achieve a large tilt angle under a low drive voltage that the comb-drive does and possess fairly simple fabrication process same as that of the parallel-plate. A new fabrication process based on SOI wafer, hybrid bulk/surface micromachined technology, and a high-aspect-ratio shadow mask is presented. Moreover, the fabrication process is successfully extended to fabricate 2×2 and 4×4 micromirror arrays. Finally, a biaxial MEMS mirror with SW electrodes was used into Confocal MACROscope for imaging. Studied optical requirements in terms of two optical configurations and frequency optimization of the micromirror, the biaxial MEMS mirror replaces the galvo-scanner and improves the MACROscope. Meanwhile, a new Micromirror-based Laser Scanning Microscope system is presented and allows 2D images to be acquired and displayed.

Acknowledgements

It is a pleasure to thank the many people who made this thesis possible. I would like to express my sincere gratitude to my supervisor, Professor John T.W. Yeow, for his support, encouragement, and guidance. I am also thankful to my co-supervisor, Professor Brian C. Wilson, for his continuous support and patience.

I am thankful to my committee member, Professor Eihab M. Abdel-Rahman, for valuable discussions and suggestions, and to my committee member, Professor John S. Zelek, for strict requirements on my writing. I am also grateful to my committee member, Professor William W. Melek who kindly accepted to take the post from Professor Hamid Jahed, and my external examiner, Professor Muthukumaran Packirisamy from Concordia University, for taking time to review my thesis.

I would like to thank Professor Michael Skvarla from Cornell NanoScale Science and Technology facility, for teaching me to start micromachining in clean room.

I would also like to thank Dr. Savvas Damaskinos and Dr. Paul Constantinou from Biomedical Photometrics Inc. (BPI), Waterloo, ON, for taking me into their lab and providing me the opportunity of learning experimental techniques for adjustment of optical systems.

I would like to thank my lab mates, Sangtak Park, Andrew Logan, Yun Wang, and Fred Sun for valuable discussions and suggestions. I would like to thank Manu Venkataram, Albert Chen, Ashley Ee, and Adrian Spanu, for their assistances in my work. I would also like to thank Weijie Wan, So-Ra, Tracy Bai, Joyce Gao, Mohsen Shahini, and Mehdi Shahini, for enjoyable lab time.

I acknowledge Vicky Lawrence, for her assistances on daily matters.

Finally, no words can describe my gratitude to my parents and to my mother-in-law, and to my beloved wife Lingling without her patience and support this work would have been impossible.

Contents

List of Tables	x
List of Figures	xi
List of Abbreviations	xvi
List of Symbols	xviii
Chapter 1	1
Background and Thesis Overview	1
1.1 Introduction.....	1
1.2 MEMS Mirror Overview	2
1.2.1 Surface & Bulk Micromachining Techniques.....	3
1.2.2 Materials in MEMS Mirrors.....	6
1.2.3 Actuation Mechanisms	7
1.2.3.1 Electro Thermal Bimorph Actuator.....	7
1.2.3.2 Electromagnetic Actuator.....	8
1.2.3.3 Piezoelectric Actuator	9
1.2.3.4 Electrowetting Actuator.....	9
1.2.3.5 Hybrid Microactuator	10
1.2.3.6 Electrostatic Actuators for MEMS Mirrors	10
1.2.4 Single Micromirror & Mirror Array.....	12

1.3 MEMS Mirrors in Endoscopic OCT and Confocal Microscope.....	12
1.3.1 Endoscopy, OCT and Confocal Microscopy.....	14
1.3.1.1 Endoscopy	14
1.3.1.2 OCT System	15
1.3.1.3 Confocal Microscopy	17
1.4 Thesis Organization	17
1.5 Author’s Contributions	17
Chapter 2	20
A Characteristic Study of Micromirror with Sidewall Electrodes	20
2.1 Introduction.....	20
2.2 The Theoretical Modeling of Micromirror with Sidewall Electrodes	21
2.2.1 Building a Theoretical Modeling of Micromirror with Sidewall Electrodes	21
2.2.1.1 Define the Coordinate System.....	22
2.2.1.2 Electrostatic Force on one Element of the Micromirror Plate.....	25
2.2.1.3 Equilibrium between Electrostatic Force and Mechanical Torsion	28
2.2.1.4 Integral Domain on the Micromirror Plate.....	29
2.3 The Characteristics of the Micromirror with Sidewall Electrodes	29
2.3.1 The Open-loop Drive.....	30
2.3.2 The Static Behavior of Micromirror.....	31
2.3.2.1 Linearity and Nonlinearity	31
2.3.2.2 Pull-in Voltage.....	34
2.3.3 The Dynamic Behaviour of Micromirror	39
2.3.3.1 System Dynamical Function Based on Lagrange Equations.....	39

2.3.3.2 Resonant Frequency and Frequency Shifting Phenomena	42
2.3.3.3 Transient Response at a Step Voltage Excitation.....	44
2.4 Conclusion	46
2.5 Summary	47
Chapter 3	48
Design, Fabrication, and Characterization of MEMS Mirror with Sidewall Electrodes	48
3.1 Introduction	48
3.2 Analytical Modeling of MEMS Mirror with Sidewall Electrodes.....	49
3.2.1 Modified Electrostatic Force	51
3.2.1.1 Electrostatic Field Distribution.....	51
3.2.1.2 Electrostatic Force on Gimbal Frame.....	52
3.2.1.3 Equilibrium between Electrostatic Force and Mechanical Torsion	53
3.2.1.4 Dynamic Modeling.....	53
3.2.2 Stiffness of the Serpentine Torsion Bar.....	55
3.3 Fabrication Process	58
3.3.1 Micromirror Plate Fabrication.....	58
3.3.2 Sidewall Electrodes Fabrication	60
3.3.3 Assembly of the Micromirror Plate and SW Electrodes	61
3.4 Simulation and Experiment.....	63
3.4.1 Experiment Configuration	63
3.4.2 Static Characteristics	64
3.4.3 Dynamic Characteristics.....	71
3.4.3.1 Resonance Frequency of the Micromirror.....	71

3.4.3.2 Resonance Frequency Shifting	73
3.5 Conclusions	76
3.6 Summary	77
Chapter 4	78
Design and Fabrication of 2×2 and 4×4 Micromirror Array	78
4.1 Introduction	78
4.2 Design of Micromirror Arrays	80
4.3 Fabrication of 2×2 Micromirror Array	81
4.3.1 Micromirror Array Fabrication	81
4.3.2 Sidewall Electrode Fabrication	86
4.3.3 Assembly of Micromirror Array and SW Electrodes	88
4.4 Fabrication of 4×4 Micromirror Array	91
4.5 Optimization of Design and Fabrication	92
Chapter 5	94
MEMS Mirror with SW Electrodes applied for Confocal MACROscope Imaging	94
5.1 Introduction	94
5.2 Confocal MACROscope Prototype with MEMS Mirrors	96
5.2.1 Two Optical Systems for Confocal MACROscope with MEMS Mirrors	96
5.2.2 MEMS Mirrors in Confocal MACROscope System	99
5.3 Experiments and Imaging	101
5.3.1 Transient Response of the Micromirror	101
5.3.2 Frequency Transient Response of Micromirror under Triangle Waveform	101
5.3.3 Images of Confocal MACROscope with MEMS Mirrors	107

5.3.4 Laser Scanning Microscope System with Micromirror and PIC.....	110
5.4 Conclusion	113
Chapter 6	114
Conclusions and Future Research	114
6.1 Summary and Conclusions.....	114
6.2 Future Works	116
Bibliography	117
Appendices	133
Appendix A	134

List of Tables

Table 1.1: Characteristics of different typical actuators used in the micromirrors	11
Table 2.1: Parameters of the biaxial micromirror	24
Table 2.2: Results from mathematical model method and FEM simulation	35
Table 2.3: The pull-in voltage based on different methods	38
Table 2.4: Modal analysis result: model method and ANSYS modal analysis	42
Table 3.1: Parameters of the biaxial micromirror	50
Table 3.2: Force balance on each segment of the spring (from free end)	56
Table 3.3: α -scan and β -scan resonance frequency values under different bias voltages	75

List of Figures

Figure 1.1: MEMS mirrors based on surface micromachining techniques.....	4
Figure 1.2: Various micromirrors based on hybrid bulk/surface micromachined technologies.	5
Figure 1.3: A simple 1-D micromirror with electrostatic actuators.	6
Figure 1.4: Three scanning ways for Endoscopic OCT and Confocal microscope.	13
Figure 1.5: Schematic of the 3-D endoscopic OCT probe [74]. 2-D scanning MEMS mirror is putted in front of GRIN lens. Sideimaging process	15
Figure 1.6: Schematic OCT system using a fiber-optic implementation of a Michelson interferometer with a laser low coherence light source [66].	16
Figure 1.7: Schematic diagram of a conventional confocal microscope [80].	16
Figure 2.1: Schematic diagram of a biaxial micromirror.....	23
Figure 2.2: Schematic of electrostatic distribution when micromirror lies on an arbitrary tilt angle. ...	24
Figure 2.3: The layout of the four groups of electrodes.....	25
Figure 2.4: Projected angles in between the mirror plate and sidewall electrodes.	27
Figure 2.5: Four projected lines on the micromirror ($\alpha=5^\circ$, $\beta=5^\circ$)	30
Figure 2.6: (a) (b) (c) shows the scanning angle and Z displacement under differential drive voltage, micromirror with bottom and sidewall electrodes. This result presents a linear relationship.	32

Figure 2.7: (a) (b) and (c) show the FEM simulation results: micromirror with bottom and sidewall electrodes under differential drive.....	33
Figure 2.8: Pull-in voltage characteristics during α -scan.	36
Figure 2.9: Pull-in voltage characteristics during β -scan.	36
Figure 2.10: Capacitance versus changeable tilt angle.	37
Figure 2.11: The dynamic response of α -scan (solid line) and β -scan (dotted line) at a bias voltage $V_{bias}=55V$	43
Figure 2.12: Resonant frequency of α -scan at the different bias voltage.	45
Figure 2.13: Resonant frequency of β -scan at the different bias voltage.....	45
Figure 2.14: Transient response of micromirror with sidewall and bottom electrodes. One curve comes from α -scan, another from β -scan. The step voltage is $V_s=65V$	46
Figure 3.1: Cross-section view of the micromirror with SW.....	51
Figure 3.2: SEM of a single MEMS mirror with sidewall electrodes (micromirror with 1.5 μ m torsion bar)	54
Figure 3.3: The micromirror plate fabrication process flow.....	59
Figure 3.4: The sidewall electrodes fabrication process flow.....	61
Figure 3.5: SEM of the sidewall electrodes.....	62
Figure 3.6: Schematic experimental configuration for characterizing the micromirror.	64
Figure 3.7: The linearity of the scanning angle and drive voltage for the micromirror with 3 μ m serpentine torsion bar	65
Figure 3.8: The linearity of the scanning angle and drive voltage for the micromirror with 1.5 μ m serpentine torsion bar	66

Figure 3.9: Scanning angle displacement under simple differential drive method for the micromirror with 3 μ m serpentine torsion bar. One group of curves are from micromirror with 3 μ m torsion bar with SW, the other from a 3 μ m torsion bar micromirror without SW (only bottom electrodes).....67

Figure 3.10: Scanning angle displacement under simple differential drive method. The micromirror with SW is based on different widths of torsion bar, 1.2 μ m, 1.5 μ m, and 2 μ m. The micromirror without SW is based on 1.5 μ m and 2 μ m width torsion bars68

Figure 3.11: Large scan angle tests with simple differential drive method at α - and β - scan70

Figure 3.12: Electrostatic field distribution of one quadrant of the micromirror with SW under different angular deflection71

Figure 3.13: The frequency response of micromirror with 3 μ m torsion bar and 1.5 μ m torsion bar under sinusoidal sweep experiments for a frequency range of 1Hz to 1000Hz72

Figure 3.14: The resonance frequency shifting under different bias voltages (ANSYS and experiments).....74

Figure 3.15: 3D profile of the mirror with SW acquired from an Olympus LEXT OLS3100 confocal microscope, and the distance between the mirror plate and the top of sidewall electrodes.76

Figure 4.1: The structure of 2 \times 2 micromirror array79

Figure 4.2: The fabrication process flow of 2 \times 2 and 4 \times 4 micromirror arrays82

Figure 4.3: The front side features and critical 3-end serpentine torsion bars.....83

Figure 4.4: The backside features of the micromirror array plate after DRIE84

Figure 4.5: The compressive unstressed SiO₂ thin film exposed after DRIE85

Figure 4.6: The fabrication process flow of shadow mask based on dry etching (method I)87

Figure 4.7: The fabrication process flow of shadow mask based on hybrid wet etching and dry etching (method II)88

Figure 4.8: The bulk sidewall electrodes after fabrication process.....89

Figure 4.9: SEM of alignment mark on the SW electrodes90

Figure 4.10: Photograph of 2×2 micromirror array after wire bonding in a chip carrier.....90

Figure 4.11: (a) Assembly of 4×4 micromirror array and SW electrodes; (b) SEM of 4×4 micromirror array; (c) SEM of SW electrode array; (d) 4×4 SW electrodes after shadow mask lift-off; (e) SEM of single micromirror with a broken serpentine torsion bar.92

Figure 5.1: Schematic of MACROscope system with a galvo-scanner (the micromirror instead of the galvo-scanner) [138]. DPC Detector, OFM Spectrometer, and PMT were removed from the MACROscope system during experiments.96

Figure 5.2: Optical System-I: the laser scanning microscope with a 4× beam expander. The micromirror is located at f_1 focus distance, and the entrance pupil of the objective lens at f_2 focus distance. The objective lens is M Plan Apo 5, NA=0.14, f=200.....98

Figure 5.3: Optical System-II: the laser scanning microscope with a unitary telescope. The micromirror is located between Bi-Convex lens, f_2 , and the objective lens (M Plan Apo 5, NA=0.14, f=200). The micromirror requires as close as to the entrance pupil.....98

Figure 5.4: SEM of the micromirror with SW electrodes.....100

Figure 5.5: The transient response of the micromirror with 2μm torsion bars.101

Figure 5.6: The frequency transient response of the micromirror with 2μm torsion bars driven by the triangle waveform under $V_{bias}=50V$ and $V_{ac}=2.5V$. The driving signal actuated the micromirror on α - and β -scan, respectively.....103

Figure 5.7: The frequency transient response of the micromirror with 3μm torsion bars driven by the triangle waveform. The driving signal actuated the micromirror on α - and β -scan, respectively106

Figure 5.8: The pattern scanning from the micromirror with SW electrodes with 2 μ m torsion bars. Examples of scan pattern for various combinations of amplitude and frequency [83]. ...106

Figure 5.9: The images in terms of the galvo-scanner without XYZ-stage movement. Two optical systems: without Beam Expander and with 4 \times Beam Expander. The grate patterns are 5, 10, 20, and 50 μ m. The galvo-scanner works at 40Hz. (Green laser source: $\lambda=532$ nm, the objective lens: M Plan Apo 5, NA=0.14, f=200.)108

Figure 5.10: The 1-D scanning images in terms of the micromirror with 2 μ m torsion bars. The optical system includes a 4 \times beam expander with He-Ne laser source ($\lambda=633$ nm), the objective lens: M Plan Apo 5, NA=0.14, f=200. The sample is 20 μ m metal lines. The micromirror only scans the 1-D scanning, at α -scan, without the stage movement in order to test synchronization under open-loop control. The frequency ranges from 30Hz to 70Hz. ..109

Figure 5.11: 2-D images display 20 μ m metal grate pattern. The micromirror with 2 μ m torsion bars is adopted in the optical system with unitary telescope (Optical System-II). The objective lens is f-theta lens, NA=0.14, f=200mm. The light source is green laser, $\lambda=532$ nm. The frequency of the control signal is 40Hz.....110

Figure 5.12: The laser scanning microscope system with a MEMS micromirror with 2 μ m torsion bars.111

Figure 5.13: The grate pattern images from LSMS on PIC LCD. The frame size is 240 \times 320pixels. 112

List of Abbreviations

2D	Two-dimensional
CLSM	Confocal laser scanning MACROscope
CMP	Chemical-mechanical polishing
DAQ	Data acquisition
DLP	Digital light projector
DMD	Digital Micromirror Device™
DoF	Degree of Freedom
DRIE	Deep reactive ion etching
DSP	Double side polished
EOCT	Endoscopic optical coherence tomography
FEM	Finite element method
FOV	Field of view
LPCVD	low pressure chemical vapor deposition
LSMS	laser scanning microscope system
MEMS	Micro-Electric-Mechanical System
OCT	Optical coherence tomography
ODE	Ordinary differential equation

PECVD	Plasma enhanced chemical vapor deposition
PIC	Programmable interface controller
PSD	Position sensing detector
RIE	Reactive ion etching
SCS	Single crystal silicon
SEM	Scanning electron micrograph
SOI	Silicon-on-insulator
SSP	Single side polished
SW	Sidewall

List of Symbols

d	distance between the micromirror plate and electrodes
D_i	torsional motion damping coefficient about axis i ($i=1$ for x-axis, $i=2$ for y-axis)
dP	electrostatic force acting on the micromirror element area
E	Young's modulus of the mirror plate material, $169GPa$
E	net flux of electrostatic field
E_{eij}	flux of electrostatic field caused by electrodes eij ($i = 1,2,3,4; j=1,2,3$)
f_α	natural frequency of the mirror about x-axis
f_β	natural frequency of the mirror about y-axis
F_{ZM}	mechanical force on the z-axis
F_{Zeij}^E	electrostatic force along z-axis generated by electrodes eij ($i=1,2,3,4; j=1,2,3$)
F_{z0}	mechanical force caused by the mirror plate
g	gap between micromirror plate and bottom electrodes
G	shear modulus of the hinge material, $73GPa$
$G_{f\alpha eij}, G_{f\beta eij}$	integration factor caused by electrodes eij ($i=1,2,3,4; j=1,2,3$)
G_{fZeij}	
I_{pi}	polar moment of inertia of hinge pair i ($i=1$ for x-axis, $i=2$ for y-axis)
J_i	moment of inertia i ($i=1$ for micromirror inertia, $i=2$ for gimbal inertia)
k_i	spring constant of hinge pairs i ($i=1,2$)
l	length of the torsion bars

l_o, l_f, l_p, l_i	segment length of the torsion bars
Le	distance between the parallel sidewall electrodes
L_m	length and width of the micromirror plate
M_o, T_{M0}	mechanical torques caused by the mirror plate
t_b	thickness of the torsion bars
$T_{\alpha M}$	mechanical torsion for x-axis
$T_{\beta M}$	mechanical torsion for y-axis
$T_{\alpha eij}^E$	electrostatic torsion for x-axis caused by electrodes eij ($i=1,2,3,4; j=1,2,3$)
$T_{\beta eij}^E$	electrostatic torsion for y-axis caused by electrodes eij ($i=1,2,3,4; j=1,2,3$)
V_{bias}	DC bias voltage
V_x, V_y	oscillating waveform voltage
V_i	applied voltage (micromirror plate against electrode i) ($i=1,2,3,4$)
w	width of the torsion bars

Greek letters

α	scan angle rotating about x-axis
β	scan angle rotating about y-axis
Γ_α	torque around x-axis
Γ_β	torque around y-axis
ϵ_0	dielectric constant of vacuum, $8.854e-12 F/m$
ζ	individual local coordinate along the axial length
θ	projected angle between the micromirror plate and the bottom electrodes
λ	wavelength
ρ	density of the micromirror plate material, $2329 Kg/m^3$

τ normalized time

φ, ψ projected angle between the micromirror plate and the sidewall electrodes

Chapter 1

Background and Thesis Overview

1.1 Introduction

Micro-Electro-Mechanical Systems (MEMS) micromirrors have been developed for more than two decades along with the development of MEMS technology [1]. Various MEMS devices, such as ink jet printhead, inertial sensors, pressure sensors, accelerators, gyroscopes, RF switches, resonators, and micromirrors, have been exploited. MEMS mirrors are the intensive research field among these devices. They are considered the leading technology for many application fields, such as in adaptive optics (AO), optical switches, digital light projector (DLP), high-definition (HD) laser display, barcode reader, optical coherence tomography (OCT), and confocal microscopes [2–10]. The performances and limitations of these devices are highly dependent on MEMS mirrors in systems. Particularly, there has been intensive research on integrating MEMS mirrors into an endoscopic optical coherence tomography (EOCT) system or confocal microscope. Design and fabrication of a biaxial micromirror that is capable of large 2 Degree-of-Freedom (DoF) angular scans with low driving voltages for endoscopic application and confocal microscope is the motivation of this thesis.

In this thesis, a 2-D Silicon-on-insulator (SOI) MEMS micromirror with sidewall (SW) electrodes for imaging is presented. A theoretical model of SW electrodes for a biaxial micromirror is developed. Subsequently, a novel fabrication process is developed to fabricate a biaxial micromirror with SW electrodes. The static and dynamic characteristics of the micromirror with SW electrodes are

exploited. The process is also extended to fabricate micromirror arrays. Finally, a biaxial micromirror with SW electrodes is applied into Confocal MACROscope (from Biomedical Photometrics Inc. (BPI), Waterloo, ON) for imaging.

1.2 MEMS Mirror Overview

Various MEMS mirrors are achieved through a combination of two broad micromachining technologies, surface or bulk micromachining techniques. They possess a number of attractive features, such as extremely compact structure size, small weight, potential low power and low cost, high reliability, and batched fabrication. MEMS mirrors have a large scale range from several micrometers to millimeters and a wide bandwidth in worked frequency from a low frequency (Hz) to a high frequency (kHz) in terms of different fabrications and applications. Recently, various commercial fabrication processes are developed successfully, such as Poly-MUMPs, SOI-MUMPs&Metal-MUMPs (provided by MUMSCAP), SUMMiT-V, DMD (from Texas Instrument Inc. (Dallas, TX)), Optical iMEMS process (from Analog Devices Inc.), and IntelliSense technology. However, each fabrication process has its own specification and limitation for a certain application. Thus, it is necessary to develop a novel fabrication process for a biaxial micromirror with SW electrodes that is applied into Endoscopic OCT and confocal microscope.

By studying various MEMS mirrors, their basic characters can be derived and listed as the following:

- Fabrication processes based on surface micromachining or hybrid bulk/surface micromachining techniques
- Different materials adopted by micromirrors
- Various actuation mechanisms
- Self-assembly, assembly, or non-assembly processes for micromirrors
- 1-D, 2-D, or 3-D micromirrors with gimbal or gimballess structures
- Micromirror functions in optical systems: Digital, analogue, or fixed mirror

In fact, although developing a sophisticated micromirror is very complicated, it is possible to reach the goal by grasping the fabrication process and actuation mechanism of the micromirror in terms of requirements of an application. A typical micromirror is composed of a movable mirror plate, supporting frames, and actuators.

1.2.1 Surface & Bulk Micromachining Techniques

The main techniques in MEMS technology are composed of surface micromachining and bulk micromachining. Surface micromachining techniques leave the wafer untouched, but add/remove additional layers above the wafer surface, first widely used in 1990's, while bulk micromachining techniques involve removing material from the silicon wafer itself [11]. Figure 1.1(a), (b), and (c) show three types of micromirrors based on surface micromachining. As shown in Figure 1.1(a), the micromirror is fabricated in terms of SUMMiT-V technique. Multiple layers are deposited and patterned [12]. An upper spring and a lower spring support the mirror plate. The bottom electrodes (electrostatic actuators) drive the mirror plate to rotate along two directions. Figure 1.1(b) shows a micromirror array and an electrostatic actuator in a DMD chip. The electrostatic actuator actuates the micromirror to realize "on" or "off" mode [13, 14]. A micromirror in Figure 1.1(c) is fabricated by surface micromachining. The mirror plate is elevated through a self-assembly process after all fabrication processes; therefore, a large gap between the mirror plate and bottom electrodes is created [15]. The main advantage of surface micromachining techniques is that it is compatible with CMOS process easily and suitable to obtain a large micromirror array, however, the thickness of each layer on the substrate has a limitation less than 2-3 μm . As a result, it is difficult to get a thicker mirror plate than deposited layers. The curvature of the mirror plate is large and the scanning angle is small [16, 17]. Moreover, the release process requires a bunch of etching holes on the surface of the mirror plate. Those holes degrade the optical properties [18, 19].

Hybrid bulk/surface micromachining techniques are widely adopted by various micromirrors, as shown in Figure 1.2. Combining with SOI technology, bulk micromachining easily obtains a thick

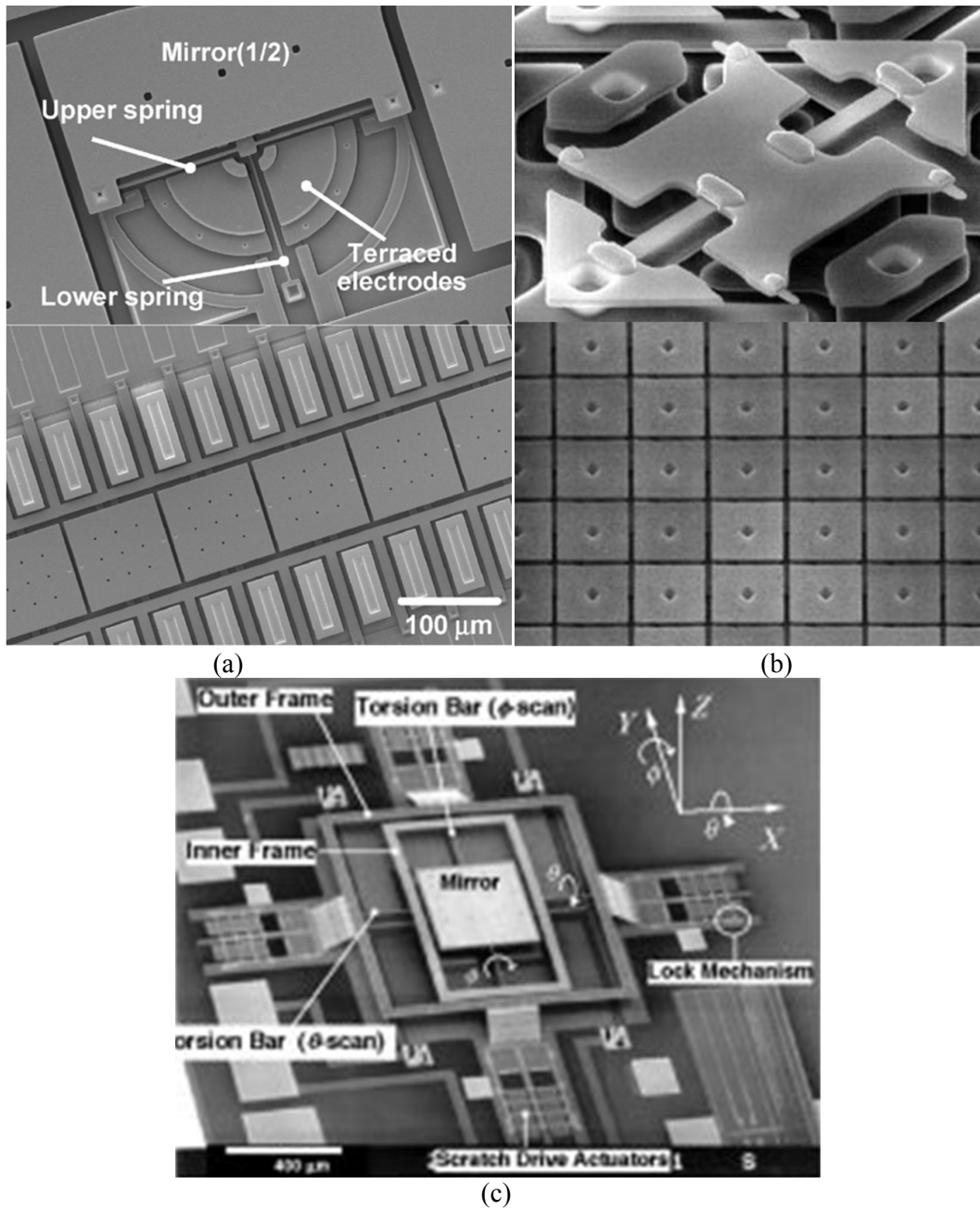


Figure 1.1: MEMS mirrors based on surface micromachining techniques. (a) A micromirror in terms of SUMiMT-V; (b) A DMD from Texas Instrument; (c) A micromirror with elevating self-assembly process.

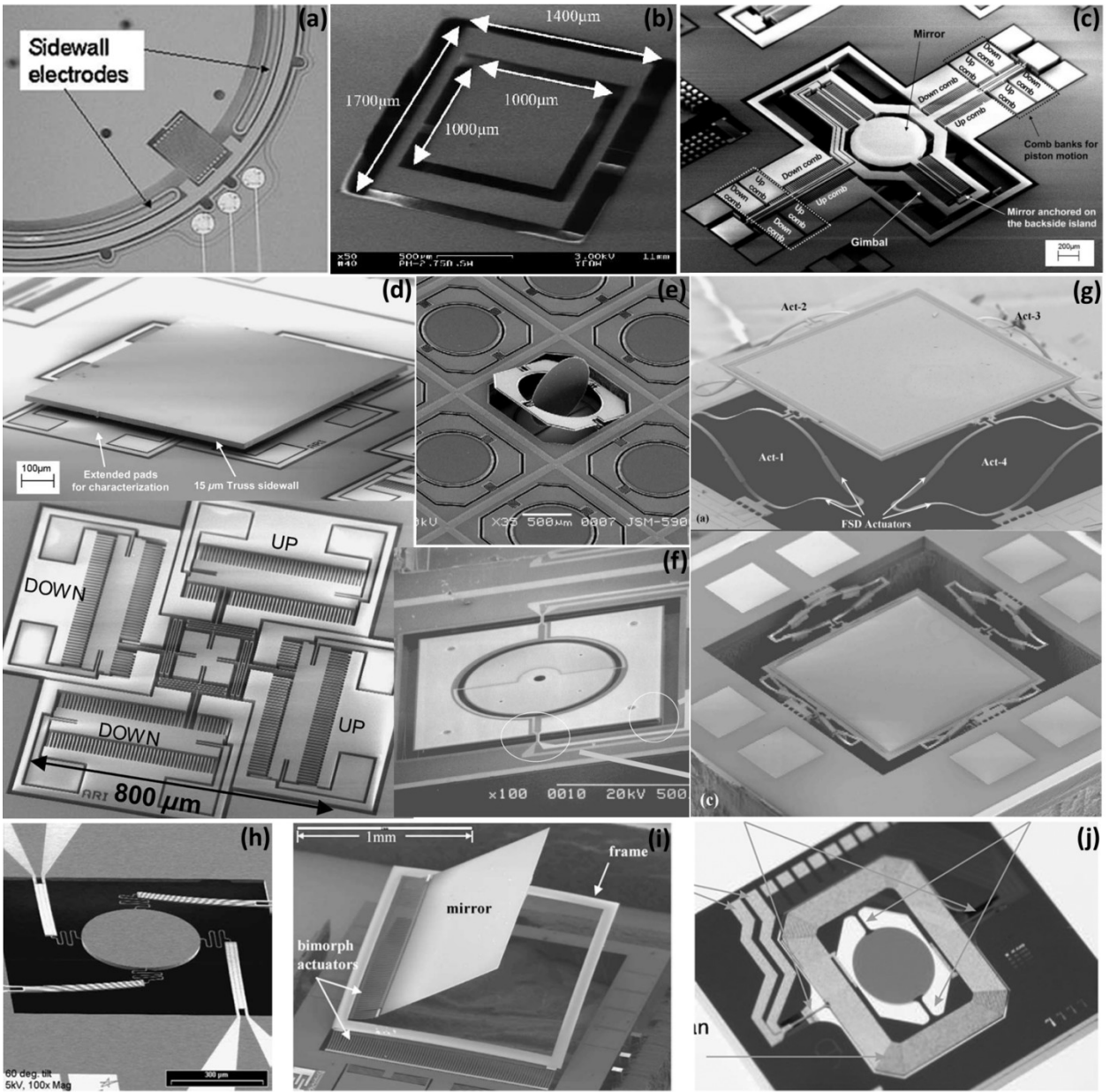


Figure 1.2: Various micromirrors based on hybrid bulk/surface micromachined technologies. (a)-(f) electrostatic actuators [20, 8, 21-24].; (g)-(i) electro thermal bimorph actuators [25-27]; (j) electromagnetic actuators [7].

mirror plate and a large cavity on the substrate, so various complex micromirrors employ hybrid bulk/surface micromachining techniques. From Figure 1.2 (a) to (f), electrostatic actuators actuate the mirror plate which has a large size and a low curvature to get 2-D scanning. Electro thermal bimorph actuators are used in some micromirrors, as shown in Figure 1.2 (g), (h), and (i). Electromagnetic actuators are adopted by the micromirror in Figure 1.2(j). The micromirrors in Figure 1.2(a), (c), (d), (f), (g), (h), and (i) require non-assembly process, while, those in Figure 1.2(b), (e), and (j) need an assembly process.

1.2.2 Materials in MEMS Mirrors

Various materials adopted by MEMS mirrors enrich fabrication processes and designs. Kurt Peterson states single crystal silicon as a perfect mechanical material in MEMS devices [28]. In micromachining, silicon, glass, ceramics, group III and V elements are important substrate materials. A variety of metals including titanium, platinum, tungsten, aluminum, gold, chrome, nickel, copper, and so on, are used widely as thin deposited films. Meanwhile, silicon dioxide, silicon nitrides, silicon carbides, carbon, and polymers (Polyimide, PMMA, SU-8, and parylene, and so on) are also deposited as thin films.

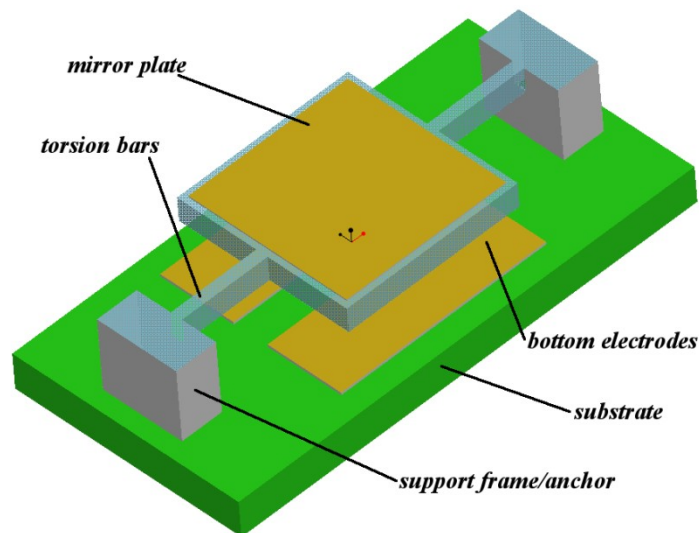


Figure 1.3: A simple 1-D micromirror with electrostatic actuators.

For example, a very simple 1-D micromirror with electrostatic actuators is composed of a movable mirror plate, torsion bars, support frames, and electrodes, as shown in Figure 1.3. Generally, materials of the mirror plate could be silicon, polysilicon, polymers, SU-8 or parylene [29], and the torsion bars may be based on silicon, polysilicon [23], silicon nitride [8], metals [30], polymer [5], or SU-8 [31]. The substrate could be silicon or glass. Metal thin films, aluminum or gold, are patterned on the substrate to form bottom electrodes. Depositing titanium/gold or chrome/aluminum on the surface of the mirror plate improves the ratio of light reflecting. Subsequently, the support frame with the mirror plate mounts on the substrate by flip-chip or bonding process. If the micromirror adopts different actuators, its corresponding materials and fabrication process have to be selected in terms of the specialty of the actuator.

1.2.3 Actuation Mechanisms

The design, fabrication, and characteristics of MEMS mirrors are highly dependent on actuation mechanisms. Actuation mechanisms include electrostatic, electro thermal bimorph, electromagnetic, PZT, electrowetting, and hybrid types. Table 1.1 illustrates the outline of different MEMS actuators used in MEMS mirrors from literatures. It is very important to understand various actuation mechanisms for selecting micromirror structures and fabrication processes when a new micromirror is developed for a special application.

1.2.3.1 Electro Thermal Bimorph Actuator

The thermal bimorph actuator is formed by using two materials with the thermal coefficient of expansion (TCE) difference. The bimorph tip performs an angular rotation due to both the residual stress and the TCE difference of two materials. The bimorph actuator is composed of either double layers with the TCE difference, such as Al/SiO₂, Au/SiO₂, metal/silicon nitride, Ni/Ni-diamond [32], or Al and SiO₂ enclosing the polysilicon or Pt heater [7, 25, 33, 34]. The bimorph actuator drives MEMS mirrors to perform either one direction (upward or downward) deflection [6, 26, 27], or dual direction movements in terms of dual S-shape bimorph [25, 34]. Its fabrication process is compatible

with CMOS sequences. The micromirror with thermal bimorph actuators can be built on one piece of single-crystal-silicon (SCS) wafer or SOI wafer entirely, so that an assembly process is avoided. In order to create an out-of-plane curling structure, the amount of fabrication experiments are required, but it is difficult to control curling angles after the mirror plate is released.

The main disadvantages of thermal actuators are high power consumption, low actuation speed, and material degradation and fatigue due to thermal stress cycles for a long period of time. The hysteresis phenomenon can be observed due to the thermal relaxation time [7]. In addition, the design of heat sink is a basic requirement for bimorph actuators [33]. The thermal resistance of bimorph actuators depends on the heat-flow path from the actuator to the substrate. This requires a sophisticated design.

1.2.3.2 Electromagnetic Actuator

Electromagnetic actuators utilize the Lorenz force, $F=I \times B$, generated when the electric current, I , pass through the coils in the external electromagnetic field with the magnetic flux density, B . Those actuators are created by either fabricating incorporated actuation coils or depositing ferromagnetic materials such as nickel-iron on the movement portion of devices [6, 10, 35-45]. In order to obtain the external electromagnetic field, some magnetic actuators use external permanent magnets or electromagnets while others use deposition and patterning of hard magnetic materials during the fabrication [41, 43, 44]. Therefore, the electroplating process is very common to fabricate thick coils or ferromagnetic materials for those actuators. Usually there is an assembly process for the last step after fabricating all the components. Magnetic actuation technique can deliver sufficient torque to allow a mirror plate to scan a large angle, thus, the size of the mirror plate can be designed in several millimeters and the spring hinge could have high spring stiffness [6]. Although the drive voltage is small, the current is high (in the range of milli-amperes (mA)) comparing with other actuators. Such actuator generates a lot of heat during work duration. Its disadvantage is potentially poor hysteresis and fatigue performance, which could affect static pointing accuracy and reliability. Most of micromirrors can realize 1-D scan [10, 37, 38], while some of micromirrors perform 2-D scan [35, 40, 43, 44].

1.2.3.3 Piezoelectric Actuator

Piezoelectric actuators utilize the piezoelectric effect, that is, when electric field applies to the class of materials, a piezoelectric thin film causes a strain to transverse direction by its inverse piezoelectric effect. Usually, a piezoelectric actuator has a metal/piezoelectric material/metal sandwich structure stacked on an insulation layer [47-52]. $\text{Pb}(\text{Zr}_x\text{Ti}_{1-x})\text{O}_3$ (PZT) is present general preferred piezoelectric material. The fabrication process is pretty simple, but requires depositing ferroelectric layers by sol-gel process and high Curie temperature [46]. When the exciting displacement frequency, that is applied electric field frequency, agrees with the resonant frequency of bending or torsional mode of a MEMS mirror, the mirror plate is actuated at the resonant vibration on each mode [47, 49]. Piezoelectric hysteresis and polarization are the main consideration during the design and fabrication [50]. In addition, since the piezoelectric actuator forms a capacitor, the leakage current is another characteristic during the design and fabrication. Zara *et al.* [48] adopted the piezoelectric bimorph as an actuator to drive the micromirror rotate about pivot axis by polyimide hinge for an endoscope.

1.2.3.4 Electrowetting Actuator

Electrowetting (EW) and Electrowetting-on-dielectric (EWOD) actuation are principles that control the shape of electrolyte drops on an electrode plate using electric potential [53, 54]. When a mirror plate is assembled on liquid droplets, the movement of the plate is generated by the shape change of droplets. The liquid metal drop (LMD) has several advantages over an electrolyte drop as a pivot of a micromirror: lower vapor pressure, less electrolysis, and better electrical/thermal contact with the substrate and the mirror. Mercury drop and gallium drop have been tested by Zeng *et al.* [53]. The insulation layer thickness between the LMD and the electrode plate affects the behavior of liquid metal drops. The micromirror plate and the electrodes are assembled with the LMD at their “confine spot”—a wetting metal spot surrounded by nonwetting parylene insulating surface treated by argon sputter. With the confine spot, the LMD drop can adhere strongly to the mirror plate and the substrate. Although the micromirror with electrowetting actuator can realize piston movement, it is essential to

realize the 2D rotation as well. The drive voltage is high. There is no any report about this kind of actuators for endoscopes in literatures.

1.2.3.5 Hybrid Microactuator

Hybrid microactuators combine two types of actuators or more to compensate disadvantages of individual actuators. Several hybrid actuators are developed: i) electromagnetic and electrostatic; ii) electromagnetic and electrothermal; iii) electrothermal and electrostatic. Il-Joo Cho *et al.* [55] used electromagnetic and electrostatic actuators into a RF-MEMS switch in order to obtain low power and low voltage operation. Youngkee Eun *et al.* [56] fabricated a micromirror with an electrothermal and electromagnetic actuator that generates a buckling deformation by the electrothermal actuator and control the buckling direction by the electromagnetic actuator in static mode. A RF-MEMS switch using electrostatic and electrothermal microactuators was fabricated by Ph. Robert *et al.* [57]. Moreover, Aravind Alwan *et al.* [58] gave an analytical modeling and figured out advantages of electrostatic and electrothermal actuation theoretically.

1.2.3.6 Electrostatic Actuators for MEMS Mirrors

Electrostatic actuators exploit the difference in electrostatic forces between two electrodes. Generally, there are two common electrostatic actuators: (i) parallel-plate; and (ii) comb-drive. Most micromirrors adopt parallel-plate actuators. They are actuated by high voltages and have a small tilt angle range. Therefore, the reduction of driving voltages while increasing the tilt angle range is a core requirement for the next-generation of electrostatic scanners. Traditionally, a biaxial micromirror is actuated by either four separate bottom electrodes [15] or by two inner bottom electrodes on the micromirror and two outer bottom electrodes on the outer attraction plates of the micromirror [8]. Meanwhile, a number of micromirrors adopt comb-drive actuators [59-63], which are built on the multiple SOI wafers and wafer bonding technology. In order to fabricate two layers of comb fingers

Table 1.1: Characteristics of different typical actuators used in the micromirrors

Characteristics	Different actuators based on different physical basis					
	Electromagnetic ¹	Bimorph electrothermal	Piezoelectric (PZT)	Electrowetting	Comb drive	Electrostatic
Physical basis	The Lorentz force $F=I \times B$	Two metals with different thermal expansion coefficient	An electrical resistor may change its resistance when it experiences a strain and deformation $R=pl/A$	Liquid metal drop changing shape at electric field $\cos \theta_2 = \cos \theta_1 + \frac{\epsilon_0 \epsilon}{2d\gamma_{lv}} u^2$	Electrostatic force, fringe field effect	An electrostatic force between the two parallel plates $F = \frac{1}{2} \left \frac{\partial C}{\partial x} \right V^2$
Substrate	SCS, SOI	SCS, SOI	SCS		SCS, SOI	SCS, SOI
Voltage	low	low	high	high	low	high
Current	large	large	small		small	small
Power consumption	high	high		low	low	low
Response time	fast	slow	fast	fast	fast	fast
Scan angle ²	large	large	small	small	large	small
Scan mode	1D, 2D	1D, 2D	1D, 2D	1D, 2D	1D, 2D	1D, 2D
Assembly ³	yes	no	no	yes	yes	yes
Structure character ⁴	gimbal	gimbal	gimbal	gimballess	gimbal, gimballess	gimbal, gimballess
Fabrication process	complex	complex	complex	simple	complex,	simple

Notice:

1. Electromagnetic actuators have a shielding requirement and require the fabrication of ferromagnetic materials, and hence increase the overall size of the micromirror system;
2. Scan range comes from literatures, and the biggest scan angle bases on the real application;
3. Assembly is a process integrating the micromirror plate with the actuators;
4. Structure of the micromirror can be divided into gimbal and gimballess. Gimbal structure increases the overall size and has a low fill factor, and gimballess structure decreases the overall size and has a high fill factor.

with different height, a sophisticated fabrication process has to be employed. One group of comb fingers realize either upward or downward movement, thus, the design of micromirrors with comb drive actuators often require a large area to accommodate the actuators and thereby increase the overall device size. More details of electrostatic actuators are presented in subsequent chapters.

Various micromirrors with different actuators in EOCT and confocal microscope have been developed. When compared with these actuators, as listed in Table 1.1, electrostatic actuators are easy to be understood and simple to realize. Therefore, this thesis focuses on developing a micromirror with electrostatic actuators.

1.2.4 Single Micromirror & Mirror Array

From single micromirror to micromirror arrays, they apply to DMD, optical switches, adaptive optics (AO), and optical phased array, and so on. Moreover, a micromirror array requires more sophisticated fabrication process than that of single micromirror. In a digital device such as a DMD chip, thousands of micromirrors are integrated at a small area. The reliability, yield rate and fill factor are important parameters. On the other hand, a micromirror array divides a large aperture into small apertures in order to keep the frequency bandwidth. In this thesis, the fabrication process is developed from single micromirror fabrication to micromirror array fabrication. Another important work is to calibrate each micromirror on an entire mirror array chip.

1.3 MEMS Mirrors in Endoscopic OCT and Confocal Microscope

Endoscopic OCT (EOCT) and confocal microscope employ MEMS mirrors to build laser scanning imaging systems. Generally, there exists three ways to perform laser beam scanning: i) beam scanning before the objective lens (Pre-Objective Scanning); ii) beam scanning after the objective lens (Post-Objective Scanning); iii) objective lens scanning. Figure 1.4 shows these three scanning configurations. MEMS mirrors are often used for the first two scanning ways, while MEMS microlenses or optic fiber bundles are adopted for the third one [8, 10, 64]. In this thesis, a biaxial micromirror with SW electrodes that is based on electrostatic actuation mechanism is mainly used

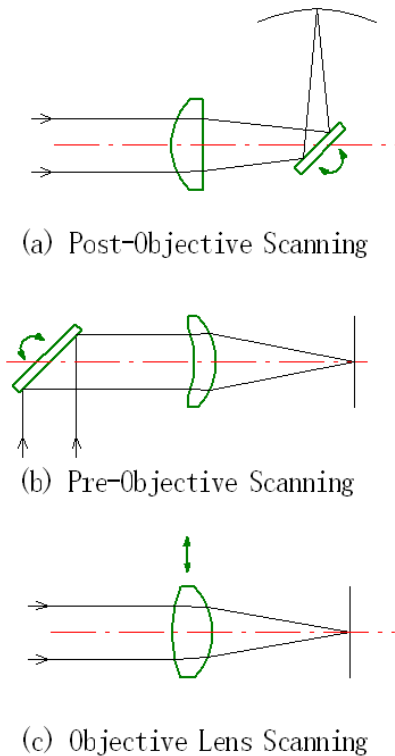


Figure 1.4: Three scanning ways for Endoscopic OCT and Confocal microscope.

into the first two ways. The goal of the thesis is to design and fabricate a biaxial micromirror for EOCT or Confocal MACROscope, which is a Confocal Laser Scanning Microscope (CLSM) with a large field of view (FOV) procured from Biomedical Photometrics Inc (BPI), Waterloo, ON. In order to integrate a micromirror with an endoscopic probe, there are several requirements the micromirror should process:

- Satisfies the endoscopic dimensional requirements: An endoscope has strict requirements on its diameter that is dependent on its application. In an endoscopic OCT system, the endoscopic probe is inserted into the human body; therefore the diameter of the endoscope will determine the diagnostic limitations. There are two scan modes: (i) side-imaging; and (ii) forward-imaging, for an endoscopic probe. The outer diameter of a side-imaging probes ranges from 0.4mm to 5mm, and that of forward-imaging probes range from 1.65mm to

7.5mm [65]. The dimensions of the micromirror have to be compatible with the diameter of the endoscopic probe.

- Provides a large scanning angle under a low driving voltage: The drive voltage actuating the micromirror is a safety concern when the endoscope is inserted into the human body. A larger angular scan will be able to create a larger field-of-view. Hence, physicians are able to image a larger piece of tissues within a shorter duration of time. This will greatly reduce the diagnostic time of the patient.
- Capable of 2 DoF scans: Combining a fast scan with a slow scan creates 2-D raster scan.
- Needs a large micromirror plate in order to obtain high resolution images.
- Requires simple fabrication processes that are compatible with MEMS fabricating technology.

1.3.1 Endoscopy, OCT and Confocal Microscopy

Endoscopic probes can be integrated with either OCT system or confocal microscope. Endoscope based on MEMS mirrors with a sophisticated optical system performs the laser beam scanning and collects reflected light that is excited or emits from the tissue or samples back to an optical fiber. Only a general discussion of selected fundamental concepts of endoscopy, OCT system and confocal microscopy is given here, for more detailed discussion see [66, 67].

1.3.1.1 Endoscopy

An endoscope is a probe for performing the laser scanning and also detecting scattered or reflected light. It is not only a diagnostic tool but it can also be used as a therapeutic equipment [65]. There are two typical endoscopes: (i) capsule endoscope; and (ii) catheter endoscope. The latter is our focus. A compact MEMS mirror is well-suited for endoscope applications because of its limited small dimension by MEMS technology. Scanning methods are of the utmost importance for endoscope probe. Generally, the scan modes can be divided into forward imaging and side imaging probe. Other important technical characteristics of an EOCT probe are the mirrors' scanning range, field-of-view (FOV), speed, and scanning flexibility.

Various endoscopes based on MEMS technology are being developed by many groups around the world [7-9, 26, 27, 68-75]. The typical structure of a MEMS-based endoscope is shown in Figure 1.5. The probe consists of a biaxial MEMS mirror and pigtailed gradient index (GRIN) lens mounted in tubular steel housing [74]. The optical fiber transmits light to the MEMS mirror and receives the scattered light from the tissues through the MEMS mirror again. The Optical fiber, GRIN lens, and the MEMS mirror are positioned so that the noise generated in the scanning head minimized. By monitoring the noise and minimizing it, high precision assembly within an error of few microns could be achieved [24].

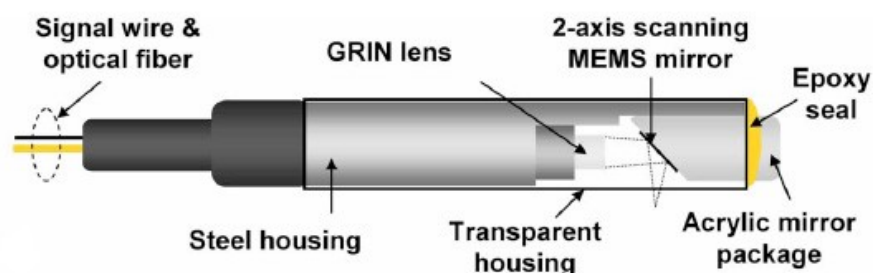


Figure 1.5: Schematic of the 3-D endoscopic OCT probe [74]. 2-D scanning MEMS mirror is putted in front of GRIN lens. Sideimaging process

1.3.1.2 OCT System

An OCT system is based on a fiber-optic Michelson interferometer to obtain high-resolution noninvasive cross-sectional imaging of tissue microstructure [66, 76-79]. OCT is an optical imaging technique that is analogous to ultrasound B-mode imaging and operates using continuous wave short coherent length light and can image the cellular structure of tissues at depths greater than conventional microscopes [66]. Light reflected from scattering sites within a sample is localized in depth by low-coherence interferometry. The low coherence interferometry measures the electromagnetic field of the optical beam rather than its intensity, since when two beams of light are combined, their fields rather than their intensities add and produce interference. Scanning a reference delay line while recording the interferometric detector response creates a map of reflectivity relative to optical depth. Here, the detector measures the intensity of the output optical beam, which is

proportional to the square of the electromagnetic field [66]. Two-dimensional images are made from sequential longitudinal image lines of backscatter versus distance into the sample. OCT produces tomographic images of subsurface microscopic structures with a resolution of $10\mu\text{m}$ or less [77, 79]. The performance of OCT systems varies widely according to their design and data acquisition speed requirements [66]. Figure 1.6 shows the schematic OCT system.

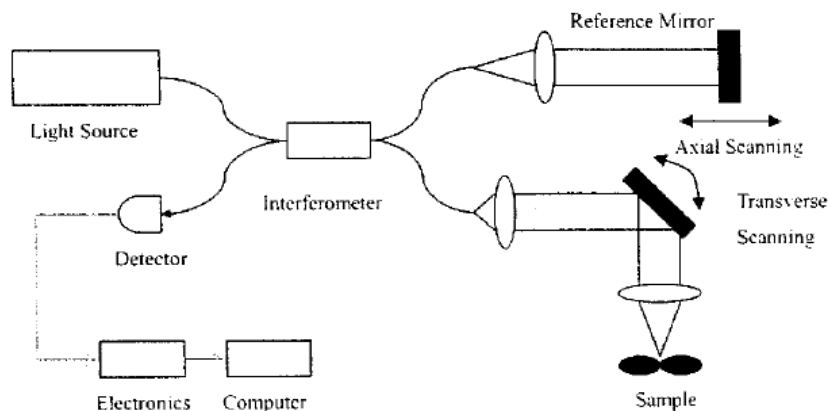


Figure 1.6: Schematic OCT system using a fiber-optic implementation of a Michelson interferometer with a laser low coherence light source [66].

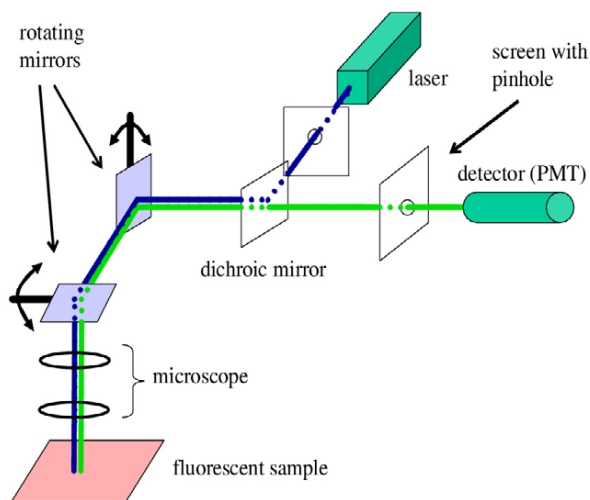


Figure 1.7: Schematic diagram of a conventional confocal microscope. The screen with the pinhole lies in the back focal plane of the sample with respect to the objective, thus rejecting most out-of-focus light. The rotating mirrors scan the sample pixel by pixel, and are the rate-limiting step for obtaining an image [80].

1.3.1.3 Confocal Microscopy

Confocal microscope is an optical imaging technique used to increase micrograph contrast and/or to reconstruct 3D images by using a spatial pinhole to eliminate out-of-focus light or flare in specimens that are thicker than the focal plane [67]. Figure 1.7 illustrates the schematic diagram of a conventional confocal microscope. In this system, a biaxial micromirror can replace the two scanning mirrors and realize the same function. More details of confocal microscope with MEMS mirrors will be discussed in Chapter 5.

1.4 Thesis Organization

The organization of this thesis is as follows. Chapter 1 contains the research background and micromirror overview. Developing a biaxial MEMS mirror applied into EOCT and confocal microscope is the motivation of this thesis. Chapter 2 presents a characteristic study of a micromirror with SW electrodes. An analytical modeling of SW electrodes for a biaxial micromirror is developed. Chapter 3 contains the design, fabrication and characterization of a 2-D micromirror with sidewall electrodes. Micromirrors with $3\mu\text{m}$ and $1.5\mu\text{m}$ serpentine torsion bars are successfully fabricated. Chapter 4 describes the fabrication process of 2×2 and 4×4 micromirror array with SW electrodes. Chapter 5 presents the micromirror with SW electrodes for the MACROscope imaging and a Micromirror-based Laser Scanning Microscope System. As the system developed is still at the proof of concept phase, a discussion on future directions is found in Chapter 6. Appendix A contains a list of integral factors.

1.5 Author's Contributions

The work in Chapter 2 was published in *International Journal of Optomechatronics*, Vol. 1, No. 3, pp231-258, July 2007 [81]. The author created an analytical modeling of SW electrodes so as to simulate the static and dynamic characteristics of a micromirror with SW electrodes. The linear voltage-to-angle property is still maintained under differential drive method and the drive voltage to

achieve the same angular displacement is greatly reduced. The pull-in voltage is not changed significantly. As a novel electrostatic actuator, using SW electrodes is the main consideration for design and fabrication of a micromirror.

The work in Chapter 3 was published in *IEEE Journal of Microelectromechanical Systems*, Vol. 19, No. 3, pp619-631, June 2010 [82]. The author designed and fabricated a 2 Degrees-of-Freedom (DoF) silicon-on-insulator (SOI) MEMS mirror with SW electrodes. The biaxial MEMS mirror with SW electrodes is actuated by electrostatic actuators. The dimension of mirror plate is $1000\mu\text{m}\times 1000\mu\text{m}$, thickness $35\mu\text{m}$. The extended analytical modeling, fabrication process, and performance characteristics are described. The chapter analyzes the effects of the 3-end single crystal serpentine torsion bar width and the bottom electrodes and SW electrodes on the performance of the mirror. A new fabrication process based on SOI wafer, hybrid bulk/surface micromachined technology, and a high aspect ratio shadow mask is presented. In comparison to previous fabrication processes and the Optical iMEMS[®] process, the process is novel, easily understood, and simple to realize. The measured maximum angular deflection achieved is $\pm 11^\circ$ (mechanical angle) at a static operating voltage and $\pm 21^\circ$ (mechanical angle) at a resonance frequency driving.

Chapter 4 devotes to extend the fabrication process of the single micromirror with SW electrodes to fabricate micromirror arrays. Four depths on the backside of the SOI wafer by DRIE process, two methods to fabricate the shadow mask, and sophisticated assembly process are the outstanding features. After optimization of the design and fabrication process, 2×2 and 4×4 micromirror arrays are obtained successfully. Although the fabrication of micromirror arrays is more difficult than that of the single micromirror, micromirror arrays achieved prove that the novel well-designed process possesses a flexibility and feasibility. The single micromirrors with SW electrodes, 2×2 and 4×4 micromirror arrays are fabricated at Cornell NanoScale Science & Technology Facility (CNF), Cornell University, USA.

The development of Micromirror-based MACROscope and a prototype of Micromirror-based Laser Scanning Microscope System are founded in Chapter 5. A biaxial MEMS mirror with SW electrodes at first time was tested in the MACROscope for the purpose of simplifying the MACROscope system.

This work cooperates with BPI. The study of optical requirements figures out optimizations on frequency and scanning range of the micromirror. In terms of experiment results from Micromirror-based MACROscope, the Micromirror-based Laser Scanning Microscope System is developed and 2-D images are obtained. This mirror is well-suited for applications where these characteristics are critical, such as in endoscopic scanning elements.

Some data in Chapter 3, Chapter 4, and Chapter 5 are from the paper “A 2-D micromachined SOI MEMS mirror with sidewall electrodes for biomedical imaging”, which has been published by *IEEE/ASME Transactions on Mechatronics*, Vol. 15, No. 4, pp501-510, 2010 [83].

Except as noted, all the experiments were performed in Professor John Yeow’s laboratory at the Advanced Micro-/Nano- Devices Lab/University of Waterloo.

Chapter 2

A Characteristic Study of Micromirror with Sidewall Electrodes

2.1 Introduction

The Optical Microelectromechanical System (MOEMS) scanner is one of the core components in many interesting fields as laser imaging, information handling, factory automation, printing, graphic arts, image digitizing, quality inspection, barcode reading, data storage, precision pattern generation, display, surveillance, and medical imaging [7, 13, 84-86]. It usually determines the device's limitation and performance. A biaxial micromirror used in an Optical Coherence Tomography (OCT) system to acquire 3-Dimensional images has already been demonstrated [8]. In addition, the micromirror actuating mechanisms such as electrostatic, thermal [26, 27, 87], piezoelectric [47, 88], electromagnetic [7], electrowetting of liquid metals [53] or hybrid actuators, are the subjects of intense research. During the actuator design process, performance such as static and dynamic characteristics of the scanner should be modeled, simulated, and understood [89, 90]. Several papers have reported the methodology on how to design a micromirror device [91-93].

Electrostatic actuator is widely used in many micromirror designs. The principles of electrostatic actuator are well-understood and their designs are simpler than other typical actuators. Electrostatic actuators are easy to fabricate by traditional integrated circuit (IC) process. There are two common electrostatic actuators: (i) parallel-plate; and (ii) comb-drive. Although parallel-plate actuators are

only capable of relatively small tilt angles under a high voltages in comparison to comb-drive actuators, their fabrication process are fairly straightforward, simple to be realized.

For parallel-plate actuators, the electrode configuration has a significant effect on the drive voltage threshold. Two typical electrode configurations have already been demonstrated: (i) planar electrode configuration [8, 9, 59-63]; (ii) inclined electrode configuration [94, 95]. The first configuration is very popular, and the second one is used by a handful of designers. Based on the electrostatic force, $F=1/2\varepsilon_0AV^2/d^2$, (ε_0 – dielectric constant of vaccum, A – effective area, d – the distance between electrode and mirror plate), if the same drive voltage is used, an increase in d will decrease the electrostatic force rapidly. Meanwhile, increasing the effect area of electrodes is effective to raise the electrostatic force. As a result, micromirrors with sidewall electrodes are proposed in Pu *et al.* [20]. Although the effect of bottom electrodes is well understood [8, 15, 96], there is no theoretical model to describe the effect of sidewall electrodes on a biaxial micromirror [97, 98]. The purpose of combining sidewall electrodes with bottom electrodes is to increase the electrostatic force on the micromirror plate. In this configuration, the static and dynamic behaviours of micromirrors deserve more investigation and detailed analyses.

In this chapter, a micromirror with a combination of sidewall and bottom electrodes will be modeled and investigated. Theoretical electrostatic model on a micromirror with sidewall and bottom electrodes are derived and simulated. Design parameters such as the controllable tilt angle, the pull-in angle and dynamic characteristics-modal analysis are studied to determine the desired scanner designs. All analytical design results are compared with Finite Element Modeling (*FEM*) simulations.

2.2 The Theoretical Modeling of Micromirror with Sidewall Electrodes

2.2.1 Building a Theoretical Modeling of Micromirror with Sidewall Electrodes

Generally, a biaxial micromirror consists of a rigid mirror plate, spring hinges, supporting frames and actuating electrodes. A micromirror structure is shown in Figure 2.1. The micromirror is suspended by the double-gimbal structure, which consists of two pairs of torsion bars (straight beam) for 2-

Degree-of-Freedom (DoF) scans: α -scan and β -scan, which rotates about the X-axis and Y-axis respectively. The micromirror plate is electrically grounded and the quadrant electrodes (sidewall and bottom electrodes) offer V_1 , V_2 , V_3 and V_4 voltages. The parameters of the micromirror are listed in Table 2.1.

In order to simplify the electrostatic force model between the micromirror and sidewall electrodes and bottom electrodes, we made several assumptions, namely:

- Ignore the electrostatic fringe field effect
- Electrostatic force caused by the bottom electrode will act on the entire micromirror plate
- Electrostatic force caused by the sidewall electrode is divided into upper sidewall electrostatic field and lower sidewall electrostatic field, as shown in Figure 2.2. The upper sidewall electrostatic field on the micromirror plate is ignored when tilt angle is small

2.2.1.1 Define the Coordinate System

Although the models for vertical electrode configuration are deduced in [97, 98], there is no existing models to describe 2 DoF configuration. The coordinate systems are defined: (i) global coordinate system (XYZ); and (ii) body-fixed coordinate system (xyz). Global coordinate system is fixed on the substrate and the origin of body-fixed coordinate system is set on the centre of the micromirror plate. These definitions are the same as Toshiyoshi *et al.* [15].

A small area (dS) on the mirror in the body-fixed coordinate system, $A(x, y, 0)$, and the normal vector of the mirror, $\mathbf{m}=(0, 0, 1)$, in Figure 2.3, are transferred to the global coordinate system, and corresponding coordinate A' and vector $\bar{\mathbf{m}}'$ are represented by:

$$A' = (x \cos \beta, x \sin \alpha \sin \beta + y \cos \alpha, -x \cos \alpha \sin \beta + y \sin \alpha) \quad (2.1)$$

and

$$\bar{\mathbf{m}}' = (\sin \beta, -\sin \alpha \cos \beta, \cos \alpha \cos \beta) \quad (2.2)$$

respectively (see, e.g., (Toshiyoshi *et al.* [15]).

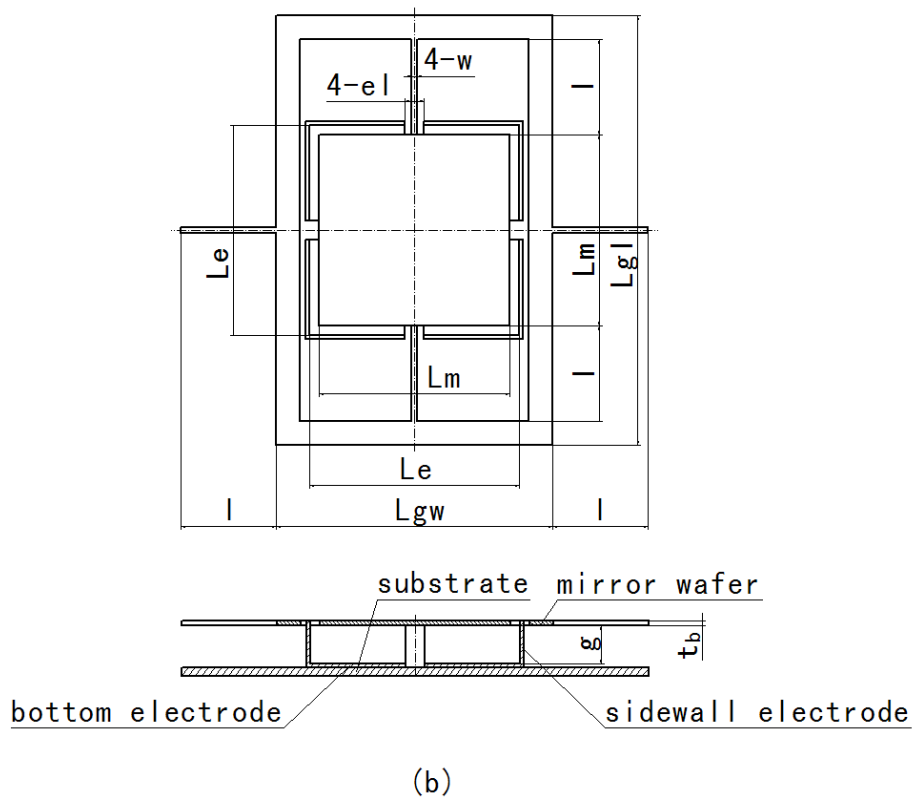
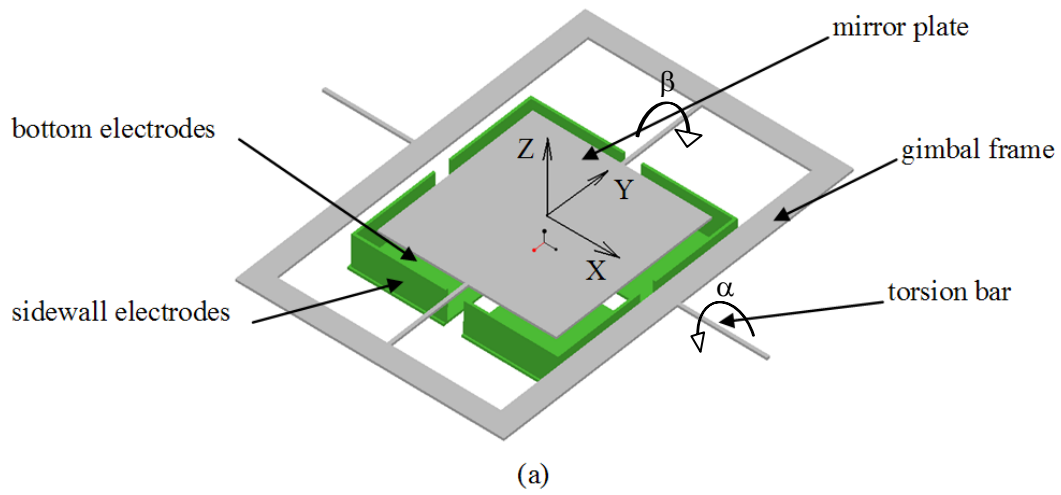


Figure 2.1: Schematic diagram of a biaxial micromirror (a) 3D diagram, mirror plate rotates about inner torsion bar, y-axis (β -scan); gimbal frame with mirror plate that rotates about outer torsion bar, x-axis (α -scan). (b) cross sectional view.

Table 2.1: Parameters of the biaxial micromirror

Parameters	Variable	Value
Micromirror properties		
Mirror width	L_m	$400\mu m$
Mirror length	L_m	$400\mu m$
Mirror plate thickness	t_m	$1.5\mu m$
Gimbal width	L_{gw}	$580\mu m$
Gimbal thickness	t_g	$1.5\mu m$
Gimbal length	L_{gl}	$900\mu m$
Torsion bar width	w	$2\mu m$
Torsion bar thickness	t_b	$1.5\mu m$
Torsion bar length	l	$200\mu m$
Electrode bottom edge width	L_e	$450\mu m$
Gap	g	$75\mu m$
Assumed material properties		
Young's modulus	E	169 Gpa [99]
Shear modulus,	G	73 Gpa
Silicon density,	ρ	2329 kg/m^3
Air permittivity,	ϵ_0	$8.854\text{e-}12\text{ F/m}$

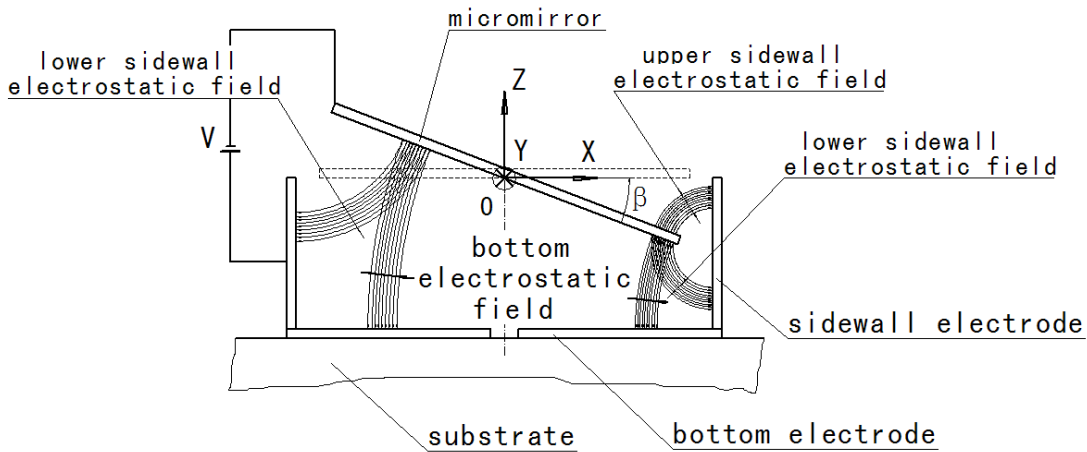


Figure 2.2: Schematic of electrostatic distribution when micromirror lies on an arbitrary tilt angle.

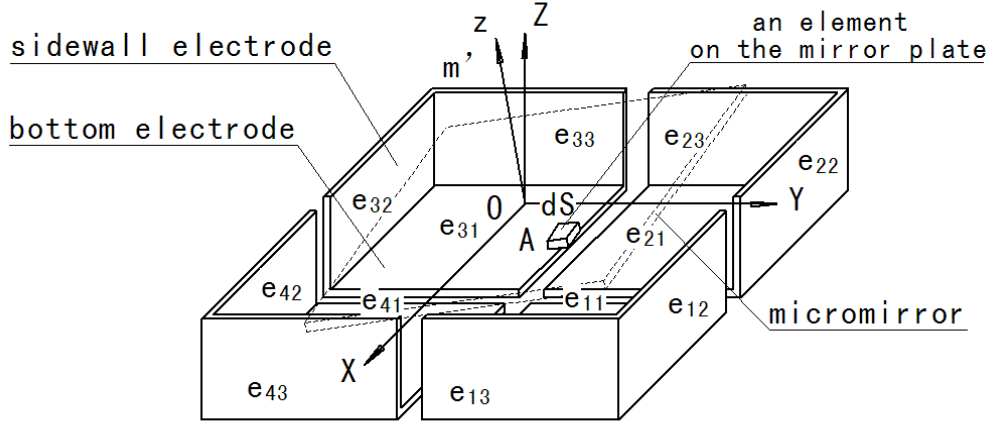


Figure 2.3: The layout of the four groups of electrodes.

Note that the four group electrodes, $e_{11} e_{12} e_{13}$, $e_{21} e_{22} e_{23}$, $e_{31} e_{32} e_{33}$, and $e_{41} e_{42} e_{43}$ are shown in Figure 2.3. When the micromirror plate is inclined, we can define the angles between the micromirror plate, and the bottom electrodes and the sidewall electrodes by θ , φ , and ψ respectively. The maximum slope angle of the mirror to the bottom electrode, θ , is equal to the angle between the normal vector of the mirror, \bar{m}' and the Z-axis ($Z=(0,0,1)$) (Toshiyoshi *et al.* [15]). In addition, as shown in Figure 2.4(a), the maximum slope angle of the mirror to the sidewall electrode (e_{12}), φ , is equal to the angle between the normal vector \bar{m}' and the Y-axis ($Y=(0,1,0)$); in Figure 2.4(b), the maximum slope angle of the mirror to the sidewall electrode (e_{13}), ψ , is equal to the angle between the normal vector \bar{m}' and the X-axis ($X=(1,0,0)$). Therefore, we take the inner product of them to find θ , φ , and ψ as follows:

$$\bar{m}' \cdot Z = \cos \theta = \cos \alpha \cos \beta, \text{ so } \theta(\alpha, \beta) = \cos^{-1}(\cos \alpha \cos \beta) \quad (2.3)$$

$$\bar{m}' \cdot Y = \cos \varphi = -\sin \alpha \cos \beta, \text{ so } \varphi(\alpha, \beta) = \cos^{-1}(-\sin \alpha \cos \beta) \quad (2.4)$$

$$\bar{m}' \cdot X = \cos \psi = \sin \beta, \text{ so } \psi(\alpha, \beta) = \cos^{-1}(\sin \beta) \quad (2.5)$$

2.2.1.2 Electrostatic Force on one Element of the Micromirror Plate

Since the flux of electrostatic field is perpendicular to the mirror surface, an element, dS , in Figure 2.3, on the mirror is attracted by electrostatic force from both the bottom electrode and the sidewall electrodes. Therefore, the net flux of electrostatic field \mathbf{E} is approximately

$$\mathbf{E} \approx \mathbf{E}_{e11} + \mathbf{E}_{e12} + \mathbf{E}_{e13} \quad (2.6)$$

for one quadrant of the mirror plate, where \mathbf{E}_{e11} , \mathbf{E}_{e12} and \mathbf{E}_{e13} are the flux of electrostatic field caused by the electrodes, e_{11} , e_{12} and e_{13} , respectively.

The electrostatic pressure is defined by:

$$F = \frac{1}{2} \varepsilon_0 E^2 = \frac{1}{2} \varepsilon_0 \left(\frac{V}{d} \right)^2 \quad (2.7)$$

$\varepsilon_0 = 8.854 \times 10^{-12}$ - dielectric constant of vacuum. The electrostatic force on the element, dS , is

$$dP = \frac{1}{2} \varepsilon_0 E^2 dS = \frac{1}{2} \varepsilon_0 \left(\frac{V}{d} \right)^2 dA \quad (2.8)$$

The moments of electrostatic force on the micromirror plate are

$$dT_\alpha = -y dP \quad (2.9)$$

and

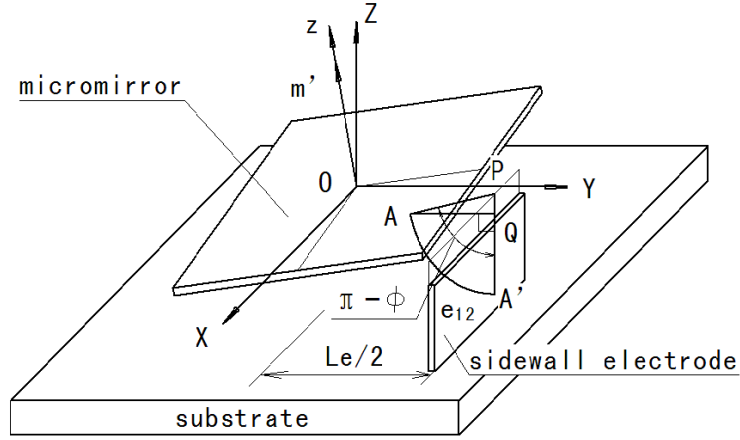
$$dT_\beta = x dP \quad (2.10)$$

– y represents the moment direction based on the global coordinate system.

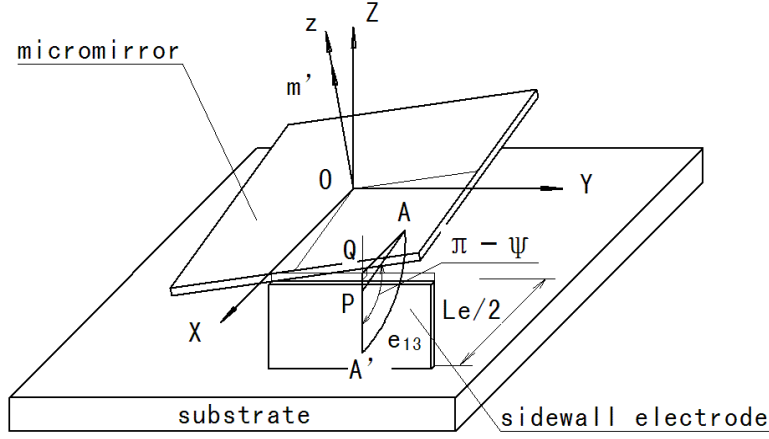
The electrostatic flux caused by sidewall electrodes on the element, dS , can be derived as

$$E_{e12} = \frac{V}{d_{12}} = \frac{V}{\widehat{AA'}} = \frac{V}{\frac{\overline{AQ}}{\sin(\pi - \varphi)} \cdot (\pi - \varphi)} = \frac{\sin(\pi - \varphi)}{\pi - \varphi} \cdot \frac{V}{Le/2 - x \sin \alpha \sin \beta - y \cos \alpha} \quad (2.11a)$$

$$E_{e13} = \frac{V}{d_{13}} = \frac{V}{\widehat{AA'}} = \frac{V}{\frac{\overline{AQ}}{\sin(\pi - \psi)} \cdot (\pi - \psi)} = \frac{\sin(\pi - \psi)}{\pi - \psi} \cdot \frac{V}{Le/2 - x \cos \beta} \quad (2.11b)$$



(a) Projected Angle $\pi - \phi$



(b) Projected Angle $\pi - \psi$

Figure 2.4: Projected angles in between the mirror plate and sidewall electrodes.

The moment of electrostatic force from sidewall electrodes on the micromirror rotating about X-axis (α -scan) are:

$$T^E_{\alpha 12}(V) = \frac{1}{2} \varepsilon_0 V^2 \iint_{Se12} -y \cdot \left(\frac{\sin(\pi - \phi)}{\pi - \phi} \cdot \frac{1}{Le/2 - x \sin \alpha \sin \beta - y \cos \alpha} \right)^2 dx dy = \frac{1}{2} \varepsilon_0 V^2 G_{fae12} \quad (2.12a)$$

$$T^E_{\alpha 13}(V) = \frac{1}{2} \varepsilon_0 V^2 \iint_{Se13} -y \cdot \left(\frac{\sin(\pi - \psi)}{\pi - \psi} \cdot \frac{1}{Le/2 - x \cos \beta} \right)^2 dx dy = \frac{1}{2} \varepsilon_0 V^2 G_{fae13} \quad (2.12b)$$

The moment of electrostatic force from sidewall electrodes on the micromirror rotating about Y-axis (β -scan) are:

$$T^E_{\beta 12}(V) = \frac{1}{2} \varepsilon_0 V^2 \iint_{S_{e12}} x \cdot \left(\frac{\sin(\pi - \varphi)}{\pi - \varphi} \cdot \frac{1}{Le/2 - x \sin \alpha \sin \beta - y \cos \alpha} \right)^2 dx dy = \frac{1}{2} \varepsilon_0 V^2 G_{f\beta e12} \quad (2.13a)$$

$$T^E_{\beta 13}(V) = \frac{1}{2} \varepsilon_0 V^2 \iint_{S_{e13}} x \cdot \left(\frac{\sin(\pi - \psi)}{\pi - \psi} \cdot \frac{1}{Le/2 - x \cos \beta} \right)^2 dx dy = \frac{1}{2} \varepsilon_0 V^2 G_{f\beta e13} \quad (2.13b)$$

Moreover, the micromirror plate is pulled down along Z direction, so the entire electrostatic forces caused by the e_{12} and e_{13} electrodes along Z-direction are the sum of components: $dP_{e12} \cos(\pi/2 - \varphi)$ and $dP_{e13} \cos(\pi/2 - \psi)$, respectively.

$$F^E_{Ze12}(V) = \frac{1}{2} \varepsilon_0 V^2 \iint_{S_{e12}} \cos(\pi/2 - \varphi) \cdot \left(\frac{\sin(\pi - \varphi)}{\pi - \varphi} \cdot \frac{1}{Le/2 - x \sin \alpha \sin \beta - y \cos \alpha} \right)^2 dx dy = \frac{1}{2} \varepsilon_0 V^2 G_{fze12} \quad (2.14a)$$

$$F^E_{Ze13}(V) = \frac{1}{2} \varepsilon_0 V^2 \iint_{S_{e13}} \cos(\pi/2 - \psi) \cdot \left(\frac{\sin(\pi - \psi)}{\pi - \psi} \cdot \frac{1}{Le/2 - x \cos \beta} \right)^2 dx dy = \frac{1}{2} \varepsilon_0 V^2 G_{fze13} \quad (2.14b)$$

where $G_{f\alpha eij}$, $G_{f\beta eij}$, and G_{fzeij} are integral factors and *Appendix A* gives all integral factor expressions which are caused by e_{11} , e_{12} , e_{13} , e_{21} , e_{22} , e_{23} , e_{31} , e_{32} , e_{33} , and e_{41} , e_{42} , e_{43} .

2.2.1.3 Equilibrium between Electrostatic Force and Mechanical Torsion

When the micromirror plate is actuated by the electrodes, the equations can be derived in terms of the equilibrium between the electrostatic and mechanical torques,

$$T_{\alpha M} = \sum_{i=1}^4 \sum_{j=1}^3 T_{\alpha eij}^E \quad (2.15a)$$

$$T_{\beta M} = \sum_{i=1}^4 \sum_{j=1}^3 T_{\beta eij}^E \quad (2.15b)$$

$$F_{ZM} = \sum_{i=1}^4 \sum_{j=1}^3 F^E_{Zejj} \quad (2.15c)$$

where the $T_{\alpha M}$, $T_{\beta M}$, mechanical torsion for X-axis and Y-axis, and F_{ZM} , mechanical force on the Z direction, which come from torsion bar [100], namely

$$T_{\alpha M} = 2 \frac{Gwt b^3}{3l} \alpha \left(1 - \frac{192}{\pi^5} \frac{t_b}{w} \tanh \frac{\pi w}{2t_b} \right) \quad (2.16a)$$

$$T_{\beta M} = 2 \frac{Gwt b^3}{3l} \beta \left(1 - \frac{192}{\pi^5} \frac{t_b}{w} \tanh \frac{\pi w}{2t_b} \right) \quad (2.16b)$$

$$F_{ZM} = \frac{1}{2} \cdot \frac{192 EI}{(2l)^3} Z \quad (2.16c)$$

The above parameters are from Table 2.1. For all bottom electrodes and sidewall electrodes, the integral factors are from *Appendix A*.

2.2.1.4 Integral Domain on the Micromirror Plate

When calculating the double integral, the integral domains are based on the effective area on which the electrostatic field is acting. The bottom electrostatic field caused by bottom electrodes e_{11} , e_{21} , e_{31} and e_{41} , we assume the integral domain is the entire micromirror plate. For the sidewall electrostatic field by e_{12} , e_{13} , e_{22} , e_{23} , e_{32} , e_{33} , e_{42} and e_{43} , we assume the effective integral domain is enclosed by the micromirror edges and the projected lines of lower sidewall electrostatic field, as shown in Figure 2.5. The projected lines, L_{AB} , L_{CD} , L_{EH} and L_{FG} are the projection of PQ , RS , PS and QR edges, respectively. In Figure 2.5, it is assumed that the scanning angle are $\alpha=5^\circ$, $\beta=5^\circ$.

2.3 The Characteristics of the Micromirror with Sidewall Electrodes

The static and the system dynamic properties of the scanner are derived and analyzed in this section. These two characteristics are important factors to be considered when designing the scanner.

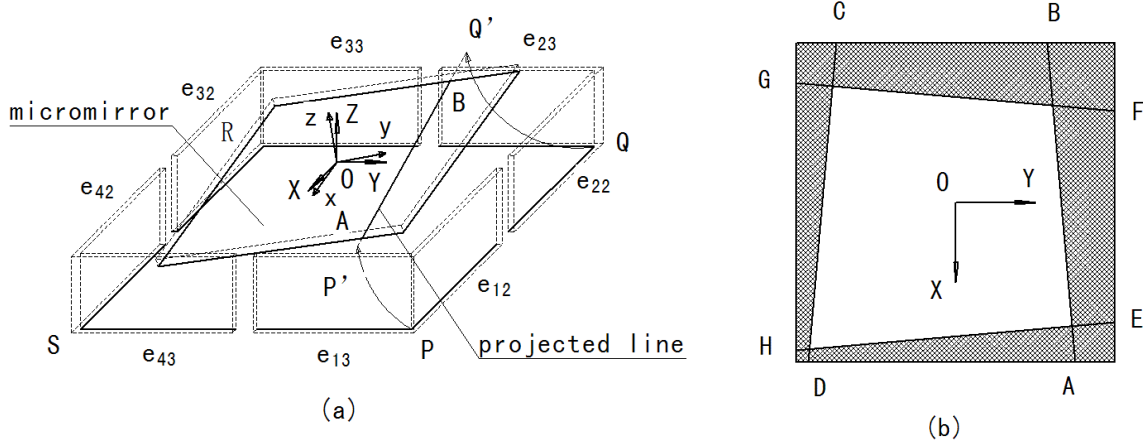


Figure 2.5: Four projected lines on the micromirror ($\alpha=5^\circ$, $\beta=5^\circ$) (a) line L_{AB} is the projection of PQ edge; (b) lines, L_{AB} , L_{CD} , L_{EH} and L_{FG} , and the shadows are composed mainly of the integral domains of lower sidewall electrostatic field.

2.3.1 The Open-loop Drive

Two drive methods are used for driving the micromirror (Toshiyoshi *et al.* [15]), one is nondifferential drive, another is differential drive. We define the differential drive

$$\begin{aligned}
 V_1 &= V_{bias} + \frac{V_x - V_y}{2} \\
 V_2 &= V_{bias} + \frac{-V_x - V_y}{2} \\
 V_3 &= V_{bias} + \frac{-V_x + V_y}{2} \\
 V_4 &= V_{bias} + \frac{V_x + V_y}{2}
 \end{aligned} \tag{2.17}$$

where V_1 is on the e_{11} , e_{12} , e_{13} electrodes, V_2 on the e_{21} , e_{22} , e_{23} electrodes, V_3 on the e_{31} , e_{32} , e_{33} electrodes, and V_4 on the e_{41} , e_{42} , e_{43} electrodes.

The micromirror plate is electrically grounded and the four group electrodes are driven by varying voltages. In the case of the differential drive method, the bias voltage on the electrodes causes the scanner to be operated under the unipolar voltage so that the micromirror will respond at the same

frequency as the drive voltage rather than twice that frequency [96]. However, the application of a DC bias voltage will alter the resonant frequency of micromirror. Section 2.3.3 will analyze this situation in detail.

2.3.2 The Static Behavior of Micromirror

2.3.2.1 Linearity and Nonlinearity

Linearity of the scan response is important for a scanner, especially for imaging applications. Particularly, the linearity property is one core technology requirement if the micromirror is used for imaging applications. It is well understood that a scanner based on differential electrostatic drive has a linear voltage-to-angle relationship (Toshiyoshi *et al.* [15]). Therefore, the voltage-to-angle characteristics of a scanner with both sidewall and bottom electrodes deserve more attention. This section will analyze the characteristics of a micromirror with sidewall electrodes.

Based on the above mathematical models, we can solve a system of nonlinear equations to determine the relationships between the drive voltages and tilt angles (α, β). The nonlinear equations are solved using MATLAB. There are two approaches to solving the nonlinear equations: (i) by using input drive voltages to solve for the tilt angles (α, β); and (ii) the other is the reciprocal of the first method.

When the differential drive method is adopted, the linear properties are shown in Figure 2.6, and Figure 2.7. Figure 2.6 is calculated from the model method by MATLAB calculation. Figure 2.7 is generated from *FEM* simulation. The linearity property of a micromirror with the addition of sidewall electrodes can be verified by our derived model and *FEM* simulation. *FEM* simulation adopt *ESSOLV* macro solver of *ANSYS* multiphysics field. Table 2.2 shows the different values for the micromirror with bottom electrodes and with sidewall electrodes at different drive voltage values. The bias voltage used is $V_{bias}=55V$.

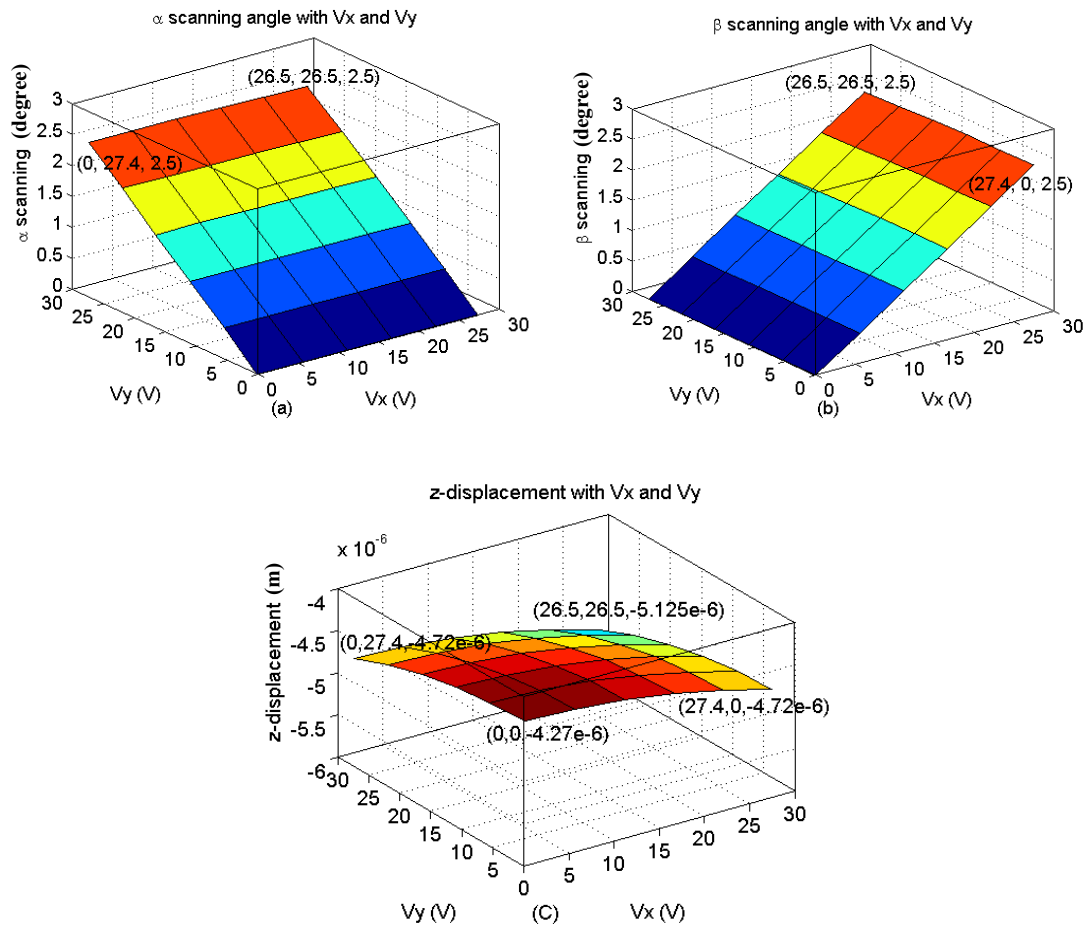


Figure 2.6: (a) (b) (c) shows the scanning angle and Z displacement under differential drive voltage, micromirror with bottom and sidewall electrodes. This result presents a linear relationship.

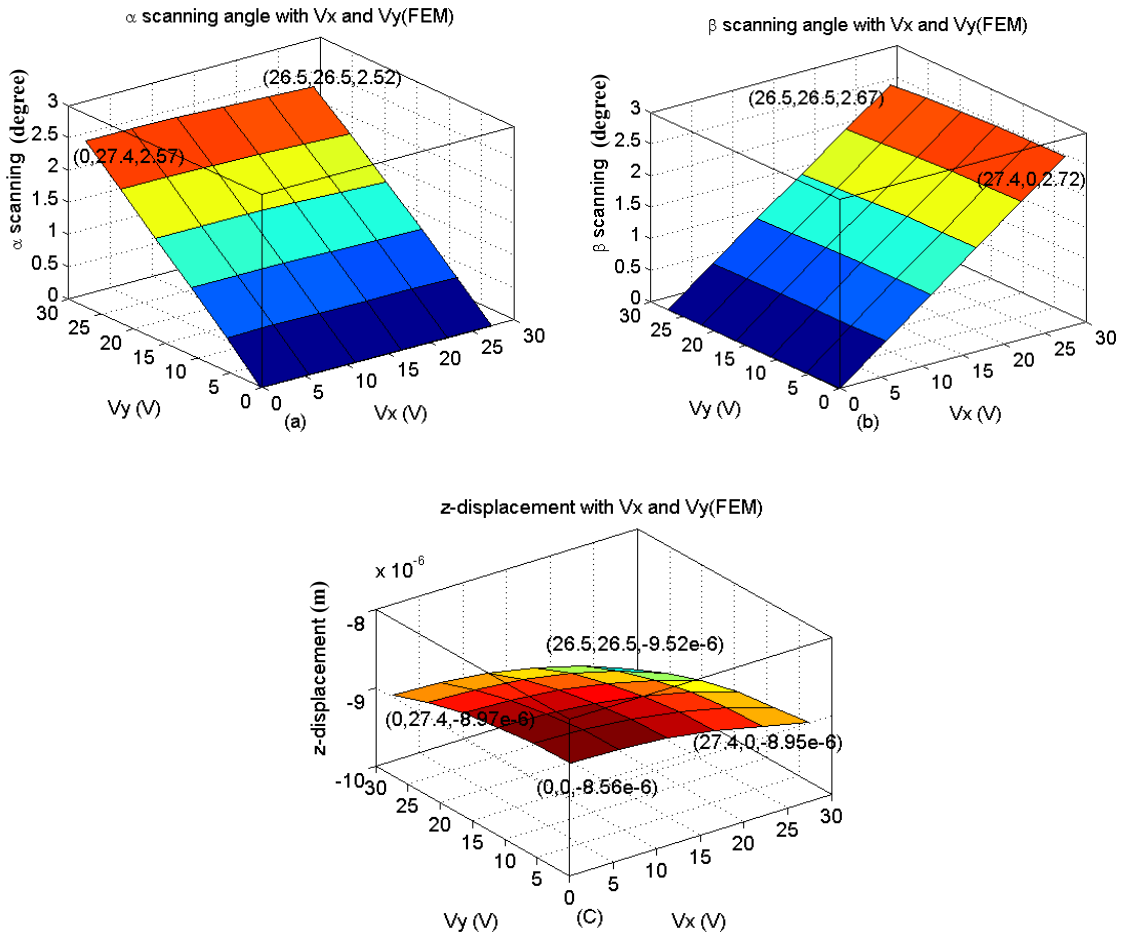


Figure 2.7: (a) (b) and (c) show the FEM simulation results: micromirror with bottom and sidewall electrodes under differential drive.

From Table 2.2, the α -scan angle, β -scan angle and Z displacement of micromirror with sidewall have been increased about 1.7 times than that with bottom electrodes based on model method. Although the results of FEM simulation and model method are different, the characteristics appear consistent.

From these figures, we observe that the design of a micromirror with the addition of sidewall electrodes can reduce the drive voltages to achieve the same scanning angles as that of only the bottom electrodes. Although the design with sidewall electrodes is beneficial for reducing the drive voltage, the Z -displacement is also larger than that with only bottom electrodes.

In addition, from Figure 2.6(c) and Figure 2.7(c), the Z -displacement of *FEM* simulation is shown to be larger than that of the model simulation. This is expected because the electrostatic field model for α - and β -scan has ignored the Z -displacement and the fringe field effect.

2.3.2.2 Pull-in Voltage

The pull-in voltage of a scanner is of interest because it shows the stable and unstable operating regions of the micromirror. There are reports on the determination of pull-in voltage of a 1-D micromirror under electrostatic force [101-103]. Xiao *et al.* [104] presented a method of calculating 2-D micromirror pull-in voltage. Based on the equilibrium Eqs. (15a) and (15b), we can directly solve these two nonlinear equations by numerical method and plot of the relative tilt angle as a function of drive voltage.

Figure 2.8 shows the relationship between the α -scan angle and drive voltage. There are four curves in the figure: (i) micromirror with sidewall under nondifferential drive voltage; (ii) micromirror with sidewall under differential drive voltage and bias voltage is 55V; (iii) micromirror with only bottom electrodes under nondifferential drive voltage; and (iv) micromirror with only bottom electrodes under differential drive voltage, bias voltage 55V. From the figure, it is observed that the α -scan pull-in voltage of micromirror with sidewall electrodes is about 100-101V, and that of micromirror with only bottom electrodes is about 104-105V.

Table 2.2: Results from mathematical model method and FEM simulation

Drive voltage value	Micromirror drive type	Model method			FEM simulation		
		α scan	β scan	Z_{disp} (μm)	α scan	β scan	Z_{disp} (μm)
$V_{bias}=55V, V_x=0V, V_y=0V$	micromirror with bottom electrodes	0°	0°	$Z_1=-2.67$	0°	0°	$Z_1=-5.37$
	micromirror with addition of sidewall electrodes	0°	0°	$Z_2=-4.29$	0°	0°	$Z_2=-8.56$
Relative change $((Z_2-Z_1)/Z_1)$				60.7%			59.4%
$V_{bias}=55V, V_y=26.5V$	micromirror with bottom electrodes	$\alpha_1=1.48^\circ$	$\beta_1=1.48^\circ$	$Z_1=-3.19$	$\alpha_1=1.87^\circ$	$\beta_1=1.88^\circ$	$Z_1=-6.44$
	micromirror with addition of sidewall electrodes	$\alpha_2=2.5^\circ$	$\beta_2=2.5^\circ$	$Z_2=-5.13$	$\alpha_2=2.52^\circ$	$\beta_2=2.67^\circ$	$Z_2=-9.52$
Relative change $((\alpha_2-\alpha_1)/\alpha_1, (\beta_2-\beta_1)/\beta_1), (Z_2-Z_1)/Z_1)$		68.9%	68.9%	60.8%	34.8%	42.02%	47.8%

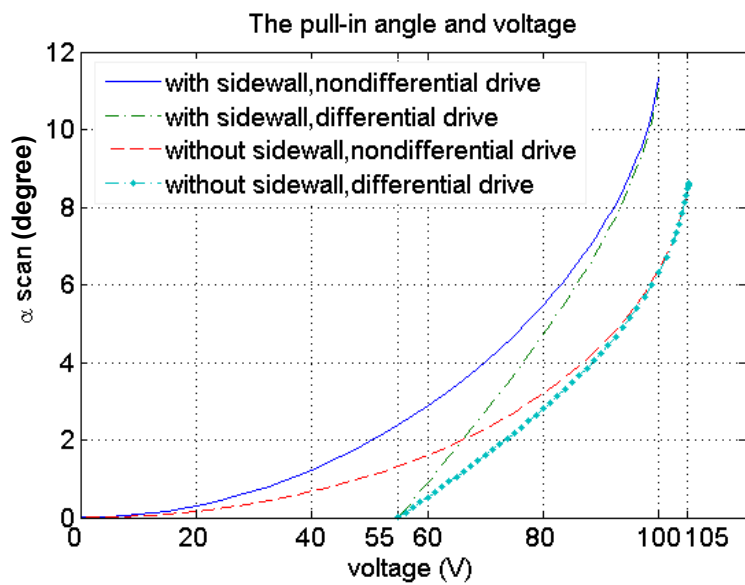


Figure 2.8: Pull-in voltage characteristics during α -scan.

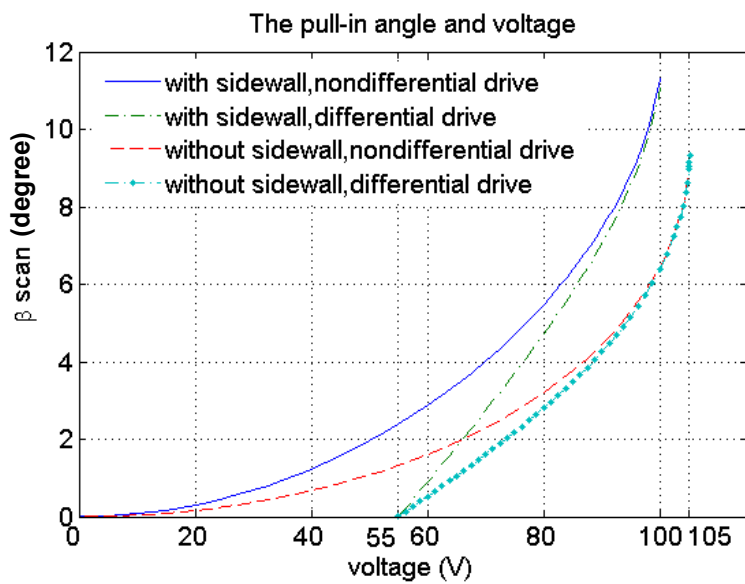


Figure 2.9: Pull-in voltage characteristics during β -scan.

Similar to Figure 2.8, Figure 2.9 illustrates the relationship in between β -scan angle and drive voltage. The β -scan pull-in voltage of micromirror with sidewall electrodes is about 100-101V, and that of micromirror with only bottom electrodes about 104-105V.

In addition, in order to verify the modeling results, additional FEM simulation is adopted. In ANSYS simulation, a capacitance versus the tilt angle function is developed by changing the value of the tilt angle and re-enabling the CMATRIX command (ANSYS R8.0 [105]). The micromirror plate, sidewall electrodes and bottom electrodes together comprise the net capacitance. Since the structure is symmetric, the capacitance curve reflects the relationship of a pair of micromirror plate and one group of electrodes (such as e_{11} , e_{12} , e_{13} , e_{21} , e_{22} , and e_{23}). Figure 2.10 displays the nonlinearity effects of capacitance related to the changeable tilt angle. These capacitance values are then placed in ANSYS model for pull-in voltage analysis.

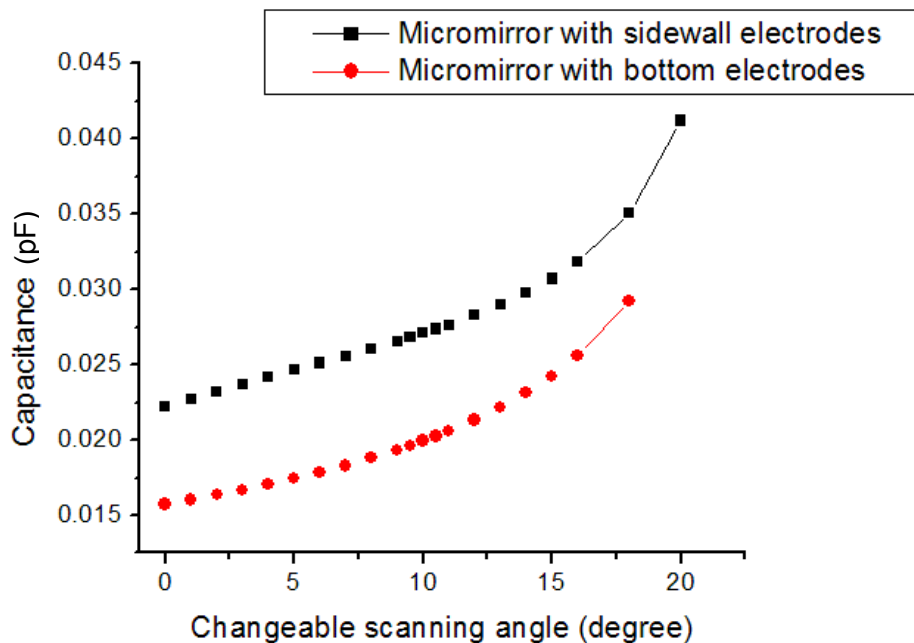


Figure 2.10: Capacitance versus changeable tilt angle.

Table 2.3: The pull-in voltage based on different methods

Pull-in direction	Micromirror drive method	Model method(V)	FEM simulation(V)	Formula (V)
α -scan	Micromirror with bottom electrodes	104-105	90-91	104.5323
	Micromirror with with addition of sidewall electrodes	100-101	97-98	
β -scan	Micromirror with bottom electrodes	104-105	86-87	104.5323
	Micromirror with with addition of sidewall electrodes	100-101	93-94	

Moreover, based on a paper by Degani *et al.* [102], we can calculate the pull-in voltage of micromirror with only bottom electrodes analytically. When calculating the α -scan pull-in voltage, the pull-in voltage is determined to be $V_{\alpha pull-in}=104.5323V$, and the β -scan pull-in voltage is $V_{\beta pull-in}=104.5323V$. All the pull-in analysis results are listed in Table 2.3.

Pull-in voltage gives the threshold of drive voltage in the stable situation. The different results of three methods used in calculating the pull-in voltage are shown in Table 2.3. The following explanations are provided:

- For micromirror with bottom electrodes, pull-in voltage is the same based on model and analytical methods. However, FEM simulation results are smaller than them. Both the model and analytical methods do not include the torsion bar bending effect, ignoring the Z-displacement. On the contrary, FEM simulation includes the fringe field effect and torsion bar bending effect. Therefore, it is expected that the pull-in voltage computed by FEM simulation is smaller.
- The formula method is not applicable to a micromirror with sidewall electrodes because it assumes parallel plate capacitance [102]. The model calculations show that the pull-in voltage of micromirror with sidewall electrodes is smaller than that with bottom electrodes. However, the results contradict that of FEM simulations. The model method ignores fringe field effect and upper sidewall electrostatic field (shown in Figure 2.2). If the scanning angle is greater

than 6° - 7° , the upper sidewall electrostatic field need cannot be ignored and is to be considered. On the other hand, FEM simulations include both of the effects.

- Although the micromirror structure uses the symmetrical quadrant electrodes, the configuration of the two pairs of torsion bar is not symmetric. When rotating about the x-axis (α -scan), the total deflection should include (i) bending of the inner and outer pairs of torsion bars; (ii) rotation of the outer pair torsion bars; and (iii) gimbal deformation. These deformations affect the α -scan more than β -scan, and thereby lead to different pull-in voltages for α -scan and β -scan. FEM simulation takes these non-idealities into account while the analytical model method ignores these parameters.

2.3.3 The Dynamic Behaviour of Micromirror

Another important property is the dynamic property of the micromirror. Dynamical analyses provide more insight into a moving system than static analyses. MEMS devices, such as RF MEMS switch, and optical MEMS switches operate at the resonant frequency, and the frequency can range from several MHz to several Hz. Dynamic analysis will show the spectral performance of such devices.

2.3.3.1 System Dynamical Function Based on Lagrange Equations

The biaxial micromirror consists of a rigid mirror plate, spring hinges and gimbals. The micromirror plate rotates about X-axis and Y-axis, and spring hinges bend along Z-axis. As a mechanical system, the biaxial mirror dynamics can be derived by using the Lagrange formulation [106]:

$$\frac{d}{dt} \left(\frac{\partial L}{\partial \dot{q}_i} \right) - \frac{\partial L}{\partial q_i} = F_i, \quad i = 1, 2 \quad (2.18)$$

where q is the generalized coordinates, and $\dot{q} = \frac{\partial q}{\partial t}$ is the generalized velocity, $L = T - U$ with T as the kinetic energy and U the potential energy. F_i is the generalized force at the corresponding axis. T can be calculated as:

$$T = \frac{1}{2} \sum_{i=1}^2 (m_i v_i^2 + J_i \omega_i^2) \quad (2.19)$$

where m_i is the micromirror mass, J_i is the moment of micromirror inertia, v_i is the velocity of the center of mass at link i with respect to the base substrate (global coordinate origin), w_i is the angular velocity about the center of mass at link i with respect to the base substrate.

And U can be calculated as:

$$U = \frac{1}{2} \sum_{i=1}^2 k_i q_i^2 \quad (2.20)$$

where k_i the hinge spring coefficients (the equivalent torsion stiffness with respect to torsion spring), it can be calculated as:

$$k_i = 4GI_{pi} / l \quad (2.21)$$

where I_{pi} the polar moment of inertia of hinge pair i , l the total length of hinge pair i , G the shear modulus of silicon. I_{pi} can be expressed as

$$I_{pi} = w \cdot t_b^3 \left[\frac{1}{3} - 0.21 \cdot \frac{t_b}{w} \left(1 - \frac{t_b^4}{12 \cdot w^4} \right) \right] \quad (2.22)$$

for ($t_b \leq w$, t_b is torsion bar thickness) [100].

Meanwhile, the moment of micromirror inertia J_i , J_l is the moment of micromirror plate inertia, J_2 is the moment of gimbal inertia, they can be expressed as

$$J_1 = \rho \cdot t_m \cdot L_m^4 / 12 \quad (2.23)$$

$$J_2 = \rho \cdot t_g \cdot \left[L_{gw} \cdot L_{gl}^3 - (L_{gw} - L_{gxx}) \cdot (L_{gl} - 2L_{ggy})^3 \right] / 12 \quad (2.24)$$

Now assuming air-damping to be zero, applying Lagrange formulation to micromirror plate leads to

$$\begin{aligned}
(J_1 + J_2)\ddot{\alpha} + k_1\alpha &= \Gamma_\alpha \\
J_1\ddot{\beta} + k_2\beta &= \Gamma_\beta
\end{aligned} \tag{2.25}$$

where

$$\begin{aligned}
\Gamma_\alpha &= \sum_{i=1}^4 \sum_{j=1}^3 T_{\alpha}^E{}_{eij} \\
\Gamma_\beta &= \sum_{i=1}^4 \sum_{j=1}^3 T_{\beta}^E{}_{eij}
\end{aligned} \tag{2.26}$$

By introducing the normalized parameters, $\tau = \omega_0 t$, $\omega_0 = \sqrt{k_2/J_1}$, $\omega_1 = \sqrt{k_1/(J_1 + J_2)}$, $\lambda_{\alpha\beta} = \omega_1^2/\omega_0^2 = \frac{k_1}{J_1 + J_2} \frac{k_2}{J_1}$, then substituting Eqs. (2.26) into (2.25), the dynamic equations become

$$\begin{aligned}
\frac{d^2\alpha}{d\tau^2} + \lambda_{\alpha\beta}\alpha &= \frac{\sum_{i=1}^4 \sum_{j=1}^3 T_{\alpha}^E{}_{eij}}{(J_1 + J_2)\omega_0^2} \\
\frac{d^2\beta}{d\tau^2} + \beta &= \frac{\sum_{i=1}^4 \sum_{j=1}^3 T_{\beta}^E{}_{eij}}{J_1\omega_0^2}
\end{aligned} \tag{2.27}$$

Eqs. (2.27) represents a set of nonlinear coupled dynamic equations for α -scan and the β -scan. Although this 2-D micromirror can perform both α -scan and the β -scan, decoupling of these two scans should lead to negligible deviation from its practical performance since the torsion beams supporting the micromirror plate and the gimbal are mechanically separated. The solution of Eqs. (2.27) can be obtained by the numerical method, i.e. Runge-Kutta method. By using the parameters in Table 2.1, the α -scan resonant frequency is determined to be $f_1 = \frac{\omega_1}{2\pi} = 617$ Hz, and the β -scan

resonant frequency is $f_2 = \frac{\omega_0}{2\pi} = 1736$ Hz.

Letting $x_1 = \alpha$, $x_2 = d\alpha/d\tau$, $x_3 = \beta$, $x_4 = d\beta/d\tau$, Eqs. (2.27) becomes a first-order differential equation set

$$\begin{aligned}
 x_1' &= x_2 \\
 x_2' &= -\lambda_{\alpha\beta} x_1 + \frac{\sum \sum T_{\alpha}^E}{(J_1 + J_2)\omega_0^2} \\
 x_3' &= x_4 \\
 x_4' &= -x_3 + \frac{\sum \sum T_{\beta}^E}{J_1\omega_0^2}
 \end{aligned} \tag{2.28}$$

By using ANSYS modal analysis, we can get results for different modes as shown in Table 2.4.

Table 2.4: Modal analysis result: model method and ANSYS modal analysis

	Model method (Hz)	ANSYS modal analysis (Hz)	
First mode (α -scan direction)	617	634.07	Torsion motion about coordinate axis X
Second mode (β -scan direction)	1736	1749.7	Torsion motion about coordinate axis Y
Third mode (Z-displacement direction)		1775.1	Vertical bending along axis Z

2.3.3.2 Resonant Frequency and Frequency Shifting Phenomena

The dynamic response of the micromirror can be solved by Eqs. (2.28). To simulate the response of the micromirror, the following arbitrary initial values are assumed: $[x_1^0, x_2^0, x_3^0, x_4^0] = [0, 0.005, 0, 0.002]$. The bias voltages are used are: 0V, 10V, 20V, 30V, 35V, 40V, 45V, 50V, 55V and 60V. Different bias voltages are substituted into Eqs. (2.28) to solve the ODE function. Finally, the time period T of the response is obtained from the solution. Figure 2.11, Figure 2.12 and Figure 2.13 demonstrate the dynamic performance of the torsion micromirror without considerations of the damping effect.

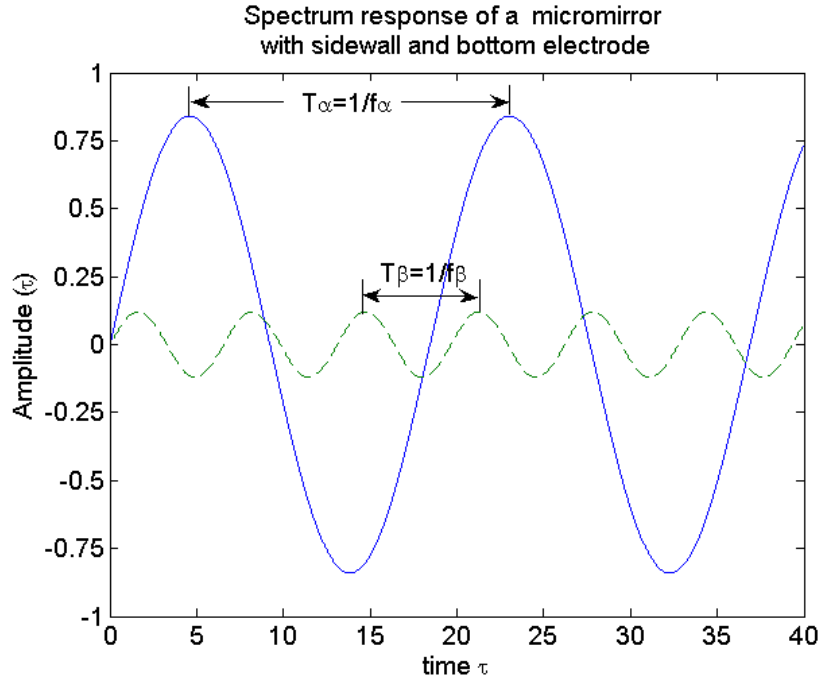


Figure 2.11: The dynamic response of α -scan (solid line) and β -scan (dotted line) at a bias voltage $V_{bias} = 55V$.

Figure 2.11 shows the solution of ODE function under a bias voltage $V_{bias} = 55V$. The solid line is the response of α -scan, while the dotted line is that of β -scan. The time periods, T_α and T_β , are observed in Figure 2.11, thereby the resonant frequency under different bias voltages, f_α and f_β can be computed [95]. The effect of bias voltages on α -scan and β -scan are shown in Figure 2.12 and Figure 2.13 respectively.

From Figure 2.12 and Figure 2.13, it is observed that the resonant frequency of the micromirror with the addition of sidewall electrodes is higher than that of micromirror without sidewall electrodes. Our derived mathematical model and ANSYS simulations show the same tendency of resonant frequency shifting, namely, undesired spring-softening effect commonly found in electrostatic actuation [96]. Both our model and ANSYS simulations show that the decrease in resonance frequency is significantly reduced by the effect of sidewall electrodes. That is the effect of sidewall electrodes is efficient for decreasing the spring-softening effect. This is advantageous when the micromirror is required to function over a wide range of operating voltages.

2.3.3.3 Transient Response at a Step Voltage Excitation

From practical performance, the damping item needs to be added into Eqs. (2.25),

$$\begin{aligned}(J_1 + J_2)\ddot{\alpha} + D_1\dot{\alpha} + k_1\alpha &= \Gamma_\alpha \\ J_1\ddot{\beta} + D_2\dot{\beta} + k_2\beta &= \Gamma_\beta\end{aligned}\quad (2.29)$$

where D_1 and D_2 are the damping coefficient. Corresponding to Eqs. (2.27), we can introduce the normalized parameters, $R_1 = \frac{D_1}{(J_1 + J_2)\omega_0}$ and $R_2 = \frac{D_2}{J_1\omega_0}$. So the dynamic equations lead to

$$\begin{aligned}\frac{d^2\alpha}{d\tau^2} + R_1\dot{\alpha} + \lambda_{\alpha\beta}\alpha &= \frac{\Gamma_\alpha}{(J_1 + J_2)\omega_0^2} \\ \frac{d^2\beta}{d\tau^2} + R_2\dot{\beta} + \beta &= \frac{\Gamma_\beta}{J_1\omega_0^2}\end{aligned}\quad (2.30)$$

The set of Eqs. (2.28) become

$$\begin{aligned}x'_1 &= x_2 \\ x'_2 &= -R_1x_2 - \lambda_{\alpha\beta}x_1 + \frac{\sum \sum T_\alpha^E}{(J_1 + J_2)\omega_0^2} \\ x'_3 &= x_4 \\ x'_4 &= -R_2x_4 - x_3 + \frac{\sum \sum T_\beta^E}{J_1\omega_0^2}\end{aligned}\quad (2.31)$$

With Eqs. (2.31), it is possible to simulate the transient behavior of the micromirror with sidewall and bottom electrodes. As an example, we can examine the transient response of the micromirror caused by a step voltage. We only consider the squeeze film damping, and the damping coefficients are estimated $[R_1, R_2]=[0.2, 0.2]$ in terms of Hao *et al.* [91] and Pan *et al.* [107]. The arbitrary initial values are assumed $[x_1^0, x_2^0, x_3^0, x_4^0]=[0, 0.02, 0, 0.02]$. Figure 2.14 shows the transient response of a step voltage, $V_s=65V$. The corresponding transient characteristics are found, such as settling time and overshoot.

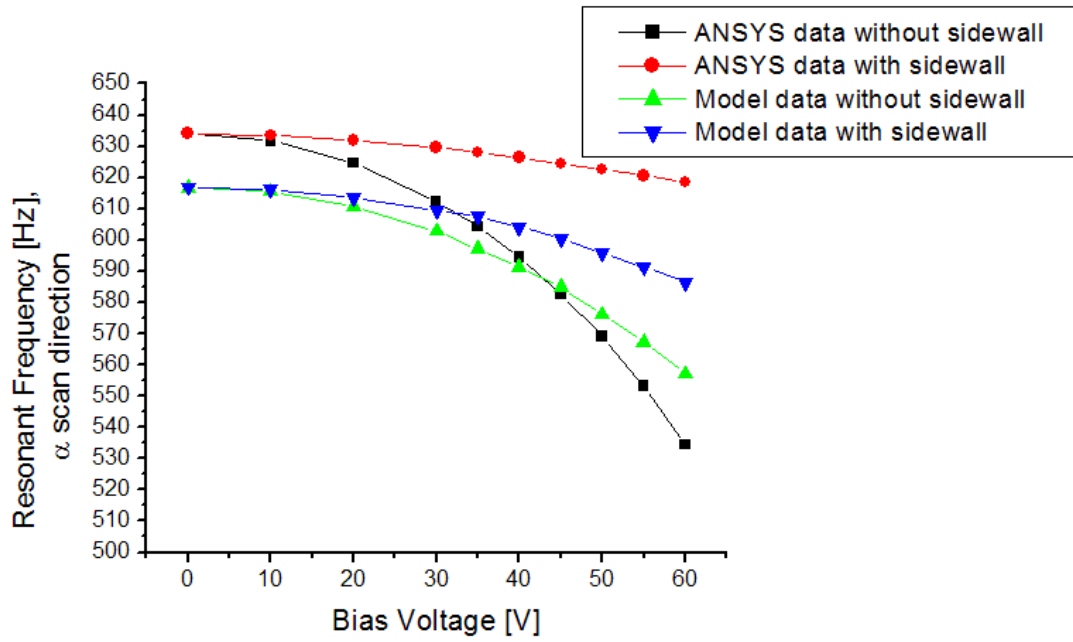


Figure 2.12: Resonant frequency of α -scan at the different bias voltage.

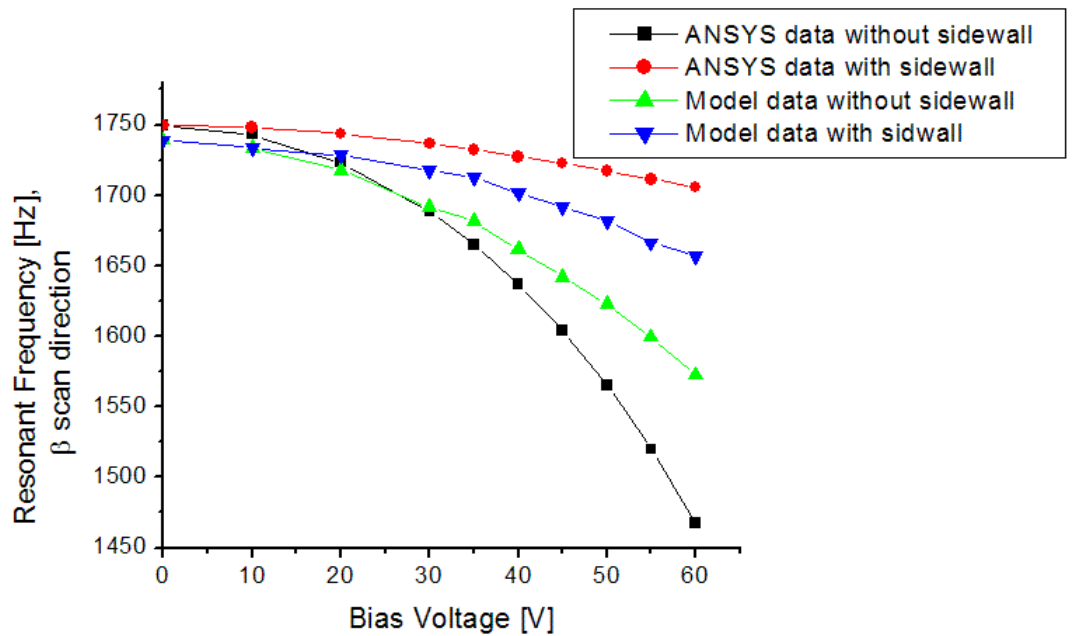


Figure 2.13: Resonant frequency of β -scan at the different bias voltage.

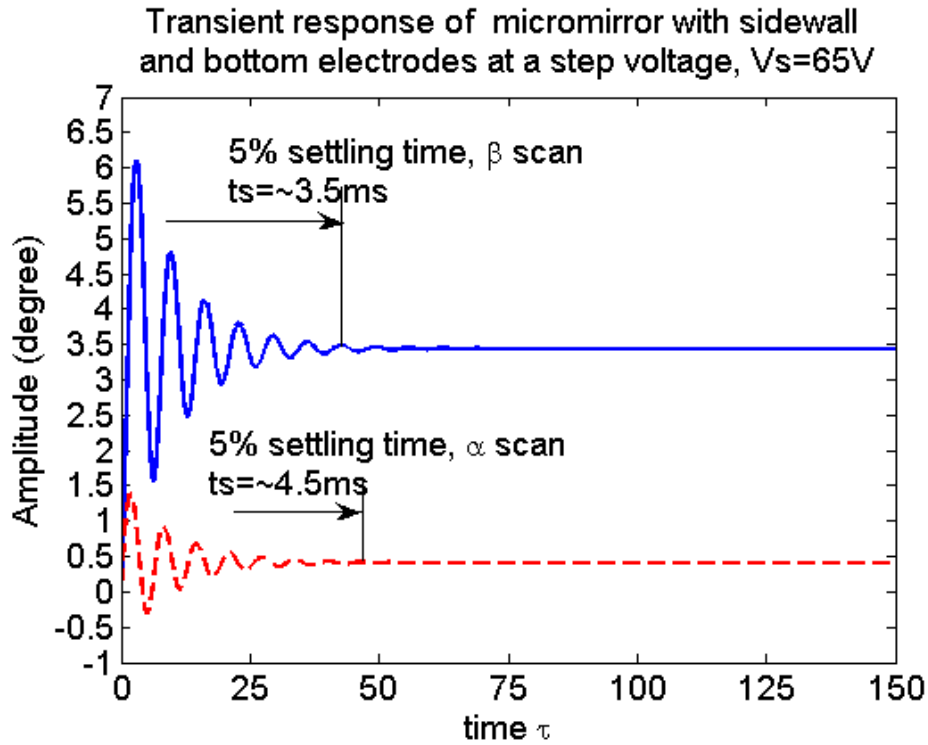


Figure 2.14: Transient response of micromirror with sidewall and bottom electrodes. One curve comes from α -scan, another from β -scan. The step voltage is $V_s=65V$.

2.4 Conclusion

Static and dynamic analyses are presented by analytical modeling of a micromirror with the addition of sidewall electrodes. Its characteristics are shown to have significant differences from micromirror with only bottom electrodes. Biaxial micromirror with the addition of sidewall electrodes appears to retain its linear angle-to-voltage property under differential drive, and the drive voltage is smaller than that of a micromirror with only bottom electrodes. Our model is also used for pull-in voltage analysis. The simplicity of our model is quite appealing. It is less consuming in term of time and processing power than FEM simulations. The system dynamic characteristic is also modeled to provide insights into the dynamic response of the micromirror with sidewall electrodes.

2.5 Summary

This chapter derived the analytical modeling of a micromirror with sidewall electrodes and studied static and dynamic characteristics of the micromirror. These results indicate that additional sidewall electrodes effectively increase a tilt angle more than only bottom electrodes under same drive voltages. The configuration of combined sidewall and bottom electrodes could benefit for a biaxial micromirror with electrostatic actuators. The developed analytical modeling of sidewall electrodes becomes a theoretical basis for a new electrostatic actuator, which is different with parallel-plate and comb-drive actuators.

Chapter 3

Design, Fabrication, and Characterization of MEMS Mirror with Sidewall Electrodes

3.1 Introduction

MEMS mirrors possess a number of attractive features, such as extremely compact structure size, potential low cost and high reliability. Thus, MEMS mirrors are considered the leading technology for endoscopic imaging systems [8, 68, 74, 96]. Designing and fabricating a novel MEMS mirror for endoscopic OCT and confocal microscope applications is the main motivation for the present work.

The micromirror is designed to satisfy the following requirements:

- large angular scan with a low driving voltage: the drive voltage actuating the micromirror is a safety concern when the endoscope is inserted into the body. Moreover, large angular scans allow a larger field-of-view, so that larger areas of tissue can be imaged within a given time.
- 2-DoF scans: combining a fast scan with a slow scan creates 2-D raster scan to build three-dimensional (3-D) images in OCT system.
- simple fabrication processes that are compatible with MEMS fabrication technology.

In previously reported micromirrors, different actuating mechanisms, such as electrostatic [8, 15, 68, 74, 91, 96], electromagnetic [6, 44], bimorph thermal [26, 71], electrowetting [53] and piezoelectric (PZT) actuators [47], have been commonly adopted. Table 1.1 lists the characteristics of

different typical actuators. Compared with other actuators, the electrostatic approach is relatively straightforward, easy to understand, and has a fairly simple fabrication process. The major disadvantage of electrostatic actuators is the requirement for large voltages, but only capable of relatively small scanning angles.

In terms of the theoretical modeling of sidewall electrodes built in Chapter 2, designing and fabricating a biaxial micromirror with SW electrodes is the focus. A micromirror with SW electrodes is proposed in Pu *et al.* [20]. The combination of sidewall and bottom electrodes increases the electrostatic force on the micromirror plate. One micromirror ($800\mu\text{m}\times 800\mu\text{m}$) with sidewall electrodes has been fabricated using the Optical iMEMS process. It uses a 3-layer silicon stack and SOI wafer bonding technique developed by Analog Devices Inc [108]. In order to obtain the $80\mu\text{m}\sim 90\mu\text{m}$ thick spacer layer, Grind, chemical-mechanical polishing (CMP) process, and multiple bonding technologies are necessary. The process is very complicated and expensive. Moreover, the process needs release holes on the device layer, and the thickness of the micromirror plate is limited by the device layer of the SOI wafer. Although the thick bulk micromirror plate has a lower curvature than devices built on surface micromachined technology to minimize distortions of the light wavefronts, it is impossible to obtain a thicker mirror plate beyond the SOI device layer based on the Optical iMEMS.

In the present work, to avoid these limitations, we have developed a novel fabrication process for the MEMS micromirror with SW electrodes. This is an inherently simple fabrication process based on SOI wafer, hybrid bulk/surface micromachined technology, and a high aspect ratio shadow mask.

In addition, we have extended theoretical model of sidewall electrodes for a biaxial micromirror. When compared with traditional electrostatic actuators, SW electrodes increase the effective area and, thereby, decrease the drive voltage needed to achieve large scanning angles. Moreover, sidewall electrodes are demonstrated to change pull-in threshold and suppress the resonance frequency shifting.

3.2 Analytical Modeling of MEMS Mirror with Sidewall Electrodes

As shown in Figure 3.2, a biaxial micromirror with SW consists of a rigid mirror plate, spring hinges, supporting frames and actuating electrodes. The micromirror is suspended by a double-gimbal structure, which consists of two pairs of torsion bars (serpentine beams) to achieve the 2-DoF scans: α - and β -scan, rotating about the X-axis and Y-axis respectively. Table 3.1 lists the parameters of the biaxial mirror. Figure 3.1 shows the cross-section view of the micromirror with SW electrodes. The term definition is the same as used in Bai *et al.* [81]. In Figure 3.2(a), the gimbal frame edges that are parallel to the X-axis are wider than along the Y-axis. This configuration is used to generate a different electrostatic field distribution on α - and β -scans. When the micromirror rotates about the X-axis (α -scan), the effective area “ A ” in the expression $F=1/2\epsilon_0AV^2/d^2$ involves the mirror plate and the gimbal frame. While rotating about Y-axis (β -scan), only the mirror plate is involved and the effective area is the mirror plate itself. As a result, slow and fast scans can be achieved in the α and β directions, respectively.

Table 3.1: Parameters of the biaxial micromirror

Parameters	Variable	Value
Micromirror properties		
Mirror width	L_m	1000 μm
Mirror length	L_m	1000 μm
Mirror plate thickness	t_m	35 μm
Gimbal outer width	L_{gw}	1400 μm
Gimbal inner width	L_{gwi}	1200 μm
Gimbal outer length	L_{gl}	1700 μm
Gimbal inner length	L_{gli}	1200 μm
Gimbal thickness	t_g	35 μm
Torsion bar width	w	3 $\mu m, 1.5 \mu m$
Torsion bar thickness	t_b	12 μm
Electrode bottom edge width	L_e	1060 μm
Gap	g	290 μm
Sidewall height	h	250 μm
Assumed material properties		

Young's modulus	E	169 Gpa
Shear modulus	G	73 Gpa
Silicon density	ρ	2329 kg/m ³
Air permittivity	ϵ_0	8.854e-12 F/m

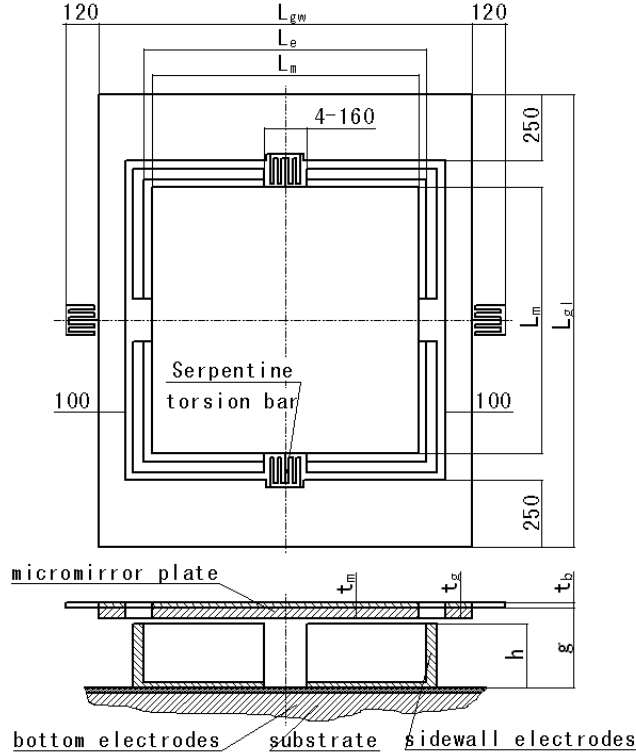


Figure 3.1: Cross-section view of the micromirror with SW.

3.2.1 Modified Electrostatic Force

3.2.1.1 Electrostatic Field Distribution

We follow the same assumptions as reported previously [81], but, the additional gimbal frame leads to an added effective area. Figure 3.5 (b) shows the sidewall electrodes after lift-off process. The maximum area of bottom electrodes is $1060\mu\text{m} \times 1060\mu\text{m}$. The size of the gimbal frame is $1700\mu\text{m} \times 1400\mu\text{m}$ of outer frame, $1200\mu\text{m} \times 1200\mu\text{m}$ of inner frame. Thus, the bottom electrostatic field is far from the gimbal frame, so it is ignored, as shown in Figure 3.12 (a). When the micromirror

plate rotates to a large scanning angle, as shown in Figure 3.12 (c), the bottom electrostatic field on the gimbal frame is still weak and can be ignored as well. Therefore, only the electrostatic force caused by the sidewall electrodes on the gimbal frame is considered. When calculating the double integral, the integral domains on the gimbal frame are the entire gimbal frame with edges along the X-axis.

3.2.1.2 Electrostatic Force on Gimbal Frame

The gimbal frame only can rotate about the α -scan axis. The additional moment of electrostatic force that is contributed from the sidewall electrodes (e_{12} , e_{22} , e_{32} and e_{42}) on gimbal frame is:

$$T^{Eg}_{\alpha 12_{-}22}(V) = \frac{1}{2} \varepsilon_0 V^2 \iint_{Se_{12_{-}22}} -y \cdot \left(\frac{\sin(\pi - \varphi)}{\varphi} \cdot \frac{1}{-Le/2 + y \cos \alpha} \right)^2 dx dy = \frac{1}{2} \varepsilon_0 V^2 G_{fg\alpha e_{12_{-}22}} \quad (3.1a)$$

$$T^{Eg}_{\alpha 32_{-}42}(V) = \frac{1}{2} \varepsilon_0 V^2 \iint_{Se_{32_{-}42}} -y \cdot \left(\frac{\sin(\pi - \varphi)}{\pi - \varphi} \cdot \frac{1}{-Le/2 - y \cos \alpha} \right)^2 dx dy = \frac{1}{2} \varepsilon_0 V^2 G_{fg\alpha e_{32_{-}42}} \quad (3.1b)$$

Simultaneously, the micromirror plate is pulled down along Z direction, so that the electrostatic forces caused by the e_{12} , e_{22} , e_{32} and e_{42} electrodes on gimbal frame along Z-direction are the sum of the components: $dP_{e_{12}} \cos(\pi/2 - \varphi)$, $dP_{e_{22}} \cos(\pi/2 - \varphi)$, $dP_{e_{32}} \cos(\pi/2 - \varphi)$, and $dP_{e_{42}} \cos(\pi/2 - \varphi)$.

$$F^{Eg}_{Ze_{12_{-}22}}(V) = \frac{1}{2} \varepsilon_0 V^2 \iint_{Se_{12_{-}22}} \cos(\pi/2 - \varphi) \cdot \left(\frac{\sin(\pi - \varphi)}{\varphi} \cdot \frac{1}{-Le/2 + y \cos \alpha} \right)^2 dx dy = \frac{1}{2} \varepsilon_0 V^2 G_{fgZe_{12_{-}22}} \quad (3.2a)$$

$$F^{Eg}_{Ze_{32_{-}42}}(V) = \frac{1}{2} \varepsilon_0 V^2 \iint_{Se_{32_{-}42}} \cos(\pi/2 - \varphi) \cdot \left(\frac{\sin(\pi - \varphi)}{\pi - \varphi} \cdot \frac{1}{-Le/2 - y \cos \alpha} \right)^2 dx dy = \frac{1}{2} \varepsilon_0 V^2 G_{fgZe_{32_{-}42}} \quad (3.2b)$$

, where $G_{fg\alpha e_{ij}}$, and $G_{fgZe_{ij}}$ are integral factors, and φ is the maximum slope angle of the mirror to the sidewall electrode.

3.2.1.3 Equilibrium between Electrostatic Force and Mechanical Torsion

When the micromirror plate is actuated by the electrodes, the equations can be derived in terms of the equilibrium between the electrostatic and mechanical torques,

$$K_{\Psi\alpha} \cdot \alpha = \sum_{i=1}^4 \sum_{j=1}^3 T_{\alpha}^E_{eij} + \sum_{i=1}^4 T_{\alpha}^{Eg}_{ei2} \quad (3.3a)$$

$$K_{\Psi\beta} \cdot \beta = \sum_{i=1}^4 \sum_{j=1}^3 T_{\beta}^E_{eij} \quad (3.3b)$$

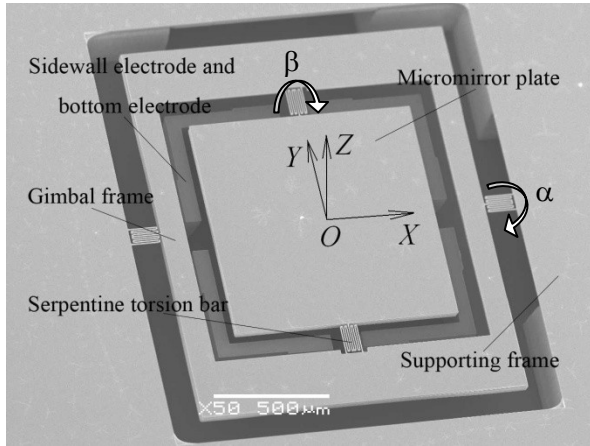
$$K_{\delta b} \cdot Z = \sum_{i=1}^4 \sum_{j=1}^3 F^E_{Zzij} + \sum_{i=1}^4 F^{Eg}_{Zei2} \quad (3.3c)$$

, where $K_{\Psi\alpha}$ and $K_{\Psi\beta}$, are the torsional stiffness of the 3-end serpentine bar at the α - and β -scans, respectively. $K_{\delta b}$ is the bending stiffness along Z-direction. We will derive these parameters in the subsequent section.

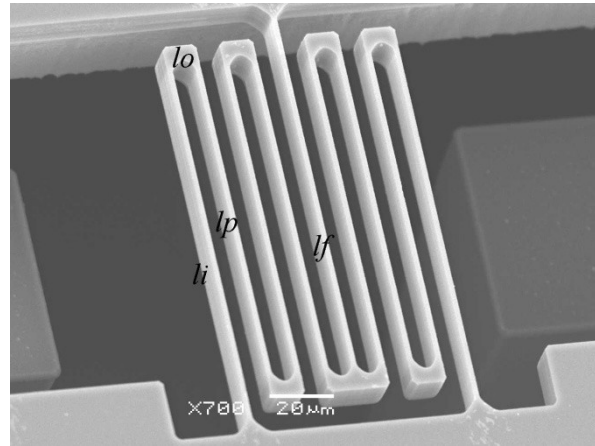
3.2.1.4 Dynamic Modeling

The dynamic response of the biaxial micromirror was derived by using the Lagrange Formulation [81, 106, 109]. The air-damping effects can be neglected since the gap between the micromirror plate and bottom electrodes is about 290 μ m and the micromirror works in the low frequency range (less than 500Hz). Thus, by introducing to the normalized parameters [81], and letting $x_1 = \alpha$, $x_2 = d\alpha/d\tau$, $x_3 = \beta$, $x_4 = d\beta/d\tau$, Eqs. (2.27) become a first-order differential equation set

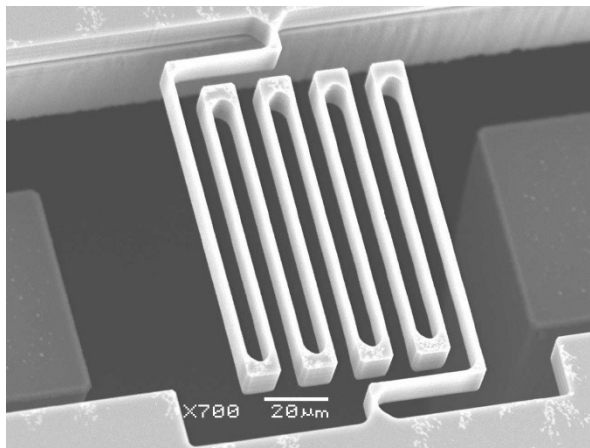
$$\begin{aligned} x'_1 &= x_2 \\ x'_2 &= -\lambda_{\alpha\beta} x_1 + \frac{\sum \sum T_{\alpha}^E + \sum T_{\alpha}^{Eg}}{(J_1 + J_2)\omega_0^2} \\ x'_3 &= x_4 \\ x'_4 &= -x_3 + \frac{\sum \sum T_{\beta}^E}{J_1\omega_0^2} \end{aligned} \quad (3.4)$$



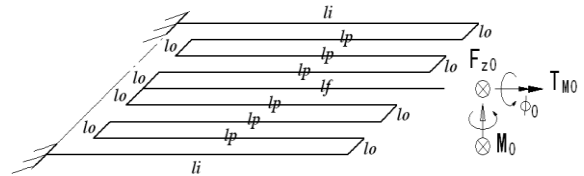
(a)



(b)



(c)



(d)

Figure 3.2: SEM of a single MEMS mirror with sidewall electrodes (micromirror with $1.5\mu\text{m}$ torsion bar). (a) as-fabricated micromirror with SW; (b) $1.5\mu\text{m}$ 3-end serpentine torsion bar; (c) $1.5\mu\text{m}$ 2-end serpentine torsion bar; (d) free body diagram of a 3-end serpentine torsion bar.

3.2.2 Stiffness of the Serpentine Torsion Bar

In comparison to a straight torsion bar, a serpentine torsion bar provides several advantages by: i) extending the effective length of beam; ii) minimizing the occupied space in order to deduce the overall size; and iii) being well-suited for simple bulk micromachining technology. There are three configurations: classic, 2-end rotated [110, 111], and 3-end serpentine springs. Figure 3.2 (b) illustrates a 3-end serpentine spring (a guided-end beam with two fixed ends and one end with the mirror plate). From the structural viewpoint, the 3-end serpentine spring is a more stable structure than the classic and rotated springs, and we have adopted it here. Although the 3-end serpentine spring is a statically indeterminate structure, the spring constant can be derived from Castigliano's 2nd theorem and the unit-load method directly [100, 112].

In order to build a stiffness model for the 3-end serpentine spring, we make several reasonable assumptions, such as small angle and vertical deflections, ignoring residual stress and extensional stress, adopting the neutral surface as an analysis basis, and considering the 3-end serpentine torsion bar as a guided-end beam. Meanwhile, we use F_{z0} , T_{M0} , and M_0 to present the forces and torques caused by the mirror plate, as shown in Figure 3.2 (d). Table 3.2 lists the transferred bending moments and torques imposed on all 17 segments of the spring, resulting from external electrostatic loads at the free end, in order to express the total strain energy. In Table 3.2 the variable, ξ , represents the individual local coordinate that is along the axial length direction. Castigliano's 2nd theorem states that the partial derivative of the strain energy of a linear structure, U , with respect a given load, F_i , M_i , and T_i , is equal to the displacement at the point of application of the load, δ_i , θ_i and ψ_i :

$$\delta_i = \frac{\partial U}{\partial F_i} \quad \theta_i = \frac{\partial U}{\partial M_i} \quad \Psi_i = \frac{\partial U}{\partial T_i} \quad (3.5)$$

In order to obtain individual spring constants from Eqs. (3.5), we can solve one the expressions and let the other two deflections equal zero simultaneously. Letting $\delta_i=0$ and $\theta_i=0$, M_0 and F_{z0} are zero, and for the torsional deflection, we obtain

Table 3.2: Force balance on each segment of the spring (from free end)

Segment No.	Length	Moment	Torque
1	l_f	$M_0 + F_{z0}\zeta$	T_{M0}
2	l_o	$1/2T_{M0} + 1/2F_{z0}\zeta$	$1/2M_0 + 1/2F_{z0}l_f$
3	l_p	$1/2M_0 + 1/2F_{z0}(l_f - \zeta)$	$1/2T_{M0} + 1/2F_{z0}l_o$
4	l_o	$1/2T_{M0} + 1/2F_{z0}(l_o + \zeta)$	$1/2M_0 + 1/2F_{z0}(l_f - l_p)$
5	l_p	$1/2M_0 + 1/2F_{z0}(l_f - l_p + \zeta)$	$1/2T_{M0} + F_{z0}l_o$
6	l_o	$1/2T_{M0} + 1/2F_{z0}(2l_o + \zeta)$	$1/2M_0 + 1/2F_{z0}l_f$
7	l_p	$1/2M_0 + 1/2F_{z0}(l_f - \zeta)$	$1/2T_{M0} + 3/2F_{z0}l_o$
8	l_o	$1/2T_{M0} + 1/2F_{z0}(4l_o + \zeta)$	$1/2M_0 + 1/2F_{z0}(l_f - l_p)$
9	l_i	$1/2M_0 + 1/2F_{z0}(l_f - l_p + \zeta)$	$1/2T_{M0} + 2F_{z0}l_o$
10	l_o	$1/2T_{M0} - 1/2F_{z0}\zeta$	$1/2M_0 + 1/2F_{z0}l_f$
11	l_p	$1/2M_0 + 1/2F_{z0}(l_f - \zeta)$	$1/2T_{M0} - 1/2F_{z0}l_o$
12	l_o	$1/2T_{M0} - 1/2F_{z0}(l_o + \zeta)$	$1/2M_0 + 1/2F_{z0}(l_f - l_p)$
13	l_p	$1/2M_0 + 1/2F_{z0}(l_f - l_p + \zeta)$	$1/2T_{M0} - F_{z0}l_o$
14	l_o	$1/2T_{M0} - 1/2F_{z0}(2l_o + \zeta)$	$1/2M_0 + 1/2F_{z0}l_f$
15	l_p	$1/2M_0 + 1/2F_{z0}(l_f - \zeta)$	$1/2T_{M0} - 3/2F_{z0}l_o$
16	l_o	$1/2T_{M0} - 1/2F_{z0}(3l_o + \zeta)$	$1/2M_0 + 1/2F_{z0}(l_f - l_p)$
17	l_i	$1/2M_0 + 1/2F_{z0}(l_f - l_p + \zeta)$	$1/2T_{M0} - 2F_{z0}l_o$

$$\Psi_t = T_{M_0} \left\{ \frac{l_f + \frac{1}{4}(6l_p) + \frac{1}{4}(2l_i)}{GJ_t} + \frac{1}{4} \frac{(8l_o)}{EI_b} \right\} \quad (3.6)$$

Letting $\psi_i=0$, T_{M_0} is zero, such that for the bending moment stiffness $K_{\theta M}$, and the bending force stiffness $K_{\delta F}$, we obtain

$$\theta_b = M_0 \left\{ \frac{1}{4EI_b} (4l_f + 6l_p + 2l_i) + \frac{1}{4GJ_t} (l_p + 7l_o) \right\} + F_{z0} \left\{ \frac{1}{4EI_b} (2l_f^2 + 6l_f l_p - 2l_p^2 + 2l_f l_i - 2l_p l_i + l_i^2) + \frac{1}{4GJ_t} (l_f l_p + 7l_f l_o - 4l_p l_o) \right\} \quad (3.7)$$

$$\begin{aligned}
\delta_b = M_0 & \left\{ \frac{1}{4EI_b} \left(\frac{1}{2} l_f^2 + 2 \left(3l_f l_p + l_f l_i - l_p l_i - \frac{3}{2} l_p^2 + \frac{1}{2} l_i^2 \right) \right) \right\} \\
& \left\{ + \frac{1}{4GJ_t} (8l_f l_o - 2l_p l_o) \right\} \\
+ F_0 & \left\{ \frac{1}{4EI_b} \left(\frac{1}{3} l_f^3 + 2 \left(\frac{64}{3} l_o^3 + 2l_f^2 l_p - 2l_f l_p^2 + l_p^3 \right) + (l_f - l_p)^2 (l_p + l_i) \right) \right\} \\
& \left\{ + (l_f - l_p) (l_p^2 + l_i^2) + \frac{1}{3} l_i^3 \right\} \\
& \left\{ + \frac{1}{4GJ_t} (4l_f^2 l_o + 28l_o^2 l_p + 4(l_f - l_p)^2 l_o + 32l_o^2 l_i) \right\}
\end{aligned} \tag{3.8}$$

Eqs.(3.7) and (3.8) can briefly be written as the following simplified forms:

$$\begin{cases} \theta_b = C_{11} M_0 + C_{12} F_{Z0} \\ \delta_b = C_{21} M_0 + C_{22} F_{Z0} \end{cases} \tag{3.9}$$

, where the coefficients C_{11} , C_{12} , C_{21} , and C_{22} are the terms of flexibility matrix of the spring. Thus, in terms of the definition of spring constant [112], the torsion stiffness $K_{\psi t}$ for a side spring is given by:

$$K_{\psi t} = \left(\frac{l_f + \frac{1}{4}(6l_p) + \frac{1}{4}(2l_i)}{GJ_t} + \frac{\frac{1}{4}(8l_o)}{EI_b} \right)^{-1} \tag{3.10}$$

Meanwhile, due to rigid body assumption of the micromirror with SW, no bending slope at free end of the serpentine spring is expected where there is a joint between the spring and the micromirror. This boundary condition is satisfied by letting the first equation in (3.9) equal zero at the joint. Substitution of the solved equivalent bending moment into the second equation in (3.9) gives the bending stiffness at the free end:

$$K_{\delta b} = \frac{C_{11}}{C_{11} C_{22} - C_{12} C_{21}} \tag{3.11}$$

The rotational stiffness at the free end can be

$$K_{ob} = \frac{C_{22}}{C_{11}C_{22} - C_{12}C_{21}} \quad (3.12)$$

Thus, we deduced the spring constant coefficient for one side of serpentine bar. For two sides of the serpentine bars, we only need to double the coefficients.

3.3 Fabrication Process

The fabrication process is divided into three steps: (i) micromirror plate fabrication, (ii) sidewall electrode fabrication, and (iii) assembly of the micromirror plate and sidewall electrodes. Single micromirror with SW, 2×2 micromirror array with SW and 4×4 micromirror array with SW are fabricated through this process.

3.3.1 Micromirror Plate Fabrication

The micromirror plate is fabricated on an SOI wafer. The SOI wafer is 100mm, device layer 12μm, buried oxide layer 0.5μm and handle layer 290μm. The fabrication process, shown in Figure 3.3, is based on reactive ion etching (RIE) and high aspect ratio deep reactive ion etching (DRIE).

Fabrication of the front side features: Layers of 0.5 μm and 2 μm silicon dioxide are deposited by using plasma enhanced chemical vapor deposition (PECVD) on top of the device layer and the handle wafer layer, respectively. Photoresist (PR) is patterned on the device layer to define the mirror plate features. RIE follows next to etch the 0.5 μm silicon dioxide layer. The patterned silicon dioxide layer is used as a mask for the subsequent DRIE process. Next, Bosch Etching DRIE is used to etch silicon and stopping on the buried oxide layer. This process forms the tiny serpentine torsion bars, the mirror plate and the gimbal frame on the device layer, as shown in Figures 3.3 (a)~(c).

Fabrication of the back side features: PR is patterned on the handle wafer layer to define the back features of the mirror. RIE is used to etch the 2μm silicon dioxide layer to expose the silicon, as shown in Figure 3.3 (d). PR is patterned on the exposed silicon to define the backside patterns of the micromirror plate and the gimbal frame, as shown in Figure 3.3 (e). DRIE is used to etch the exposed

silicon. The depth of DRIE trenches around the micromirror plate and the gimbal frame is $52\mu\text{m}\sim 57\mu\text{m}$, as shown in Figure 3.3 (f). The PR on the backside is stripped before using DRIE in order to etch the exposed silicon to a depth of $290\mu\text{m}$. DRIE etching stops at the buried oxide layer. A $35\mu\text{m}$ thick micromirror plate is created at this point, as shown in Figure 3.3 (g).

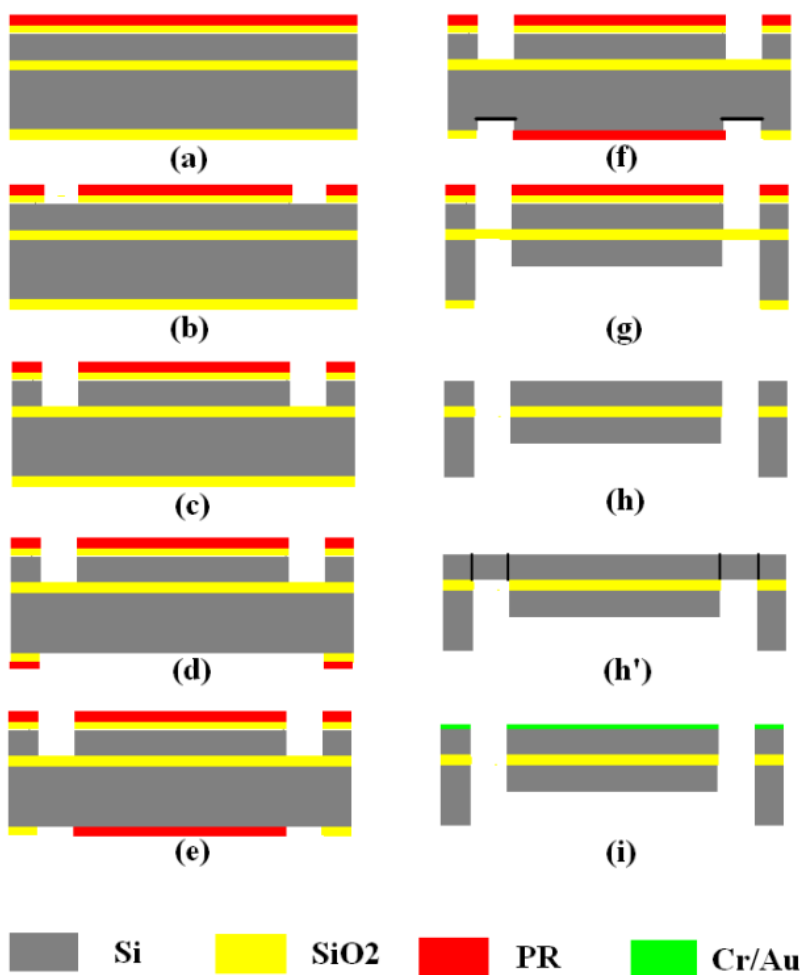


Figure 3.3: The micromirror plate fabrication process flow. (a)~(c) the micromirror front side fabrication; (d)~(g) the micromirror back side fabrication; (h)~(h') wet etching to release the micromirror; (i) evaporation of Cr/Au as a reflective coating.

Release of the micromirror plate from the SOI wafer: Releasing the micromirror plate is a challenge in the fabrication process. A wet etching method is adopted to release the micromirror plate by using 6:1 Buffered Oxide Etchant (BOE). After releasing the micromirror from the SOI wafer, DI water cleans the surface and pure alcohol dries it, as shown in Figure 3.3 (h). Figure 3.3 (h') shows the cross-sectional view of the device when rotated by 90°.

Evaporation of the reflective metals: Cr or Ti (16nm) is evaporated by using a CVC4500 evaporator as an adhesive layer before evaporating Au (150nm) as the reflective surface. Figure 3.3 (i) shows this process. The thickness of the reflective thin film affects the micromirror curvature, while the thin film quality influences the surface reflectivity.

3.3.2 Sidewall Electrodes Fabrication

The sidewall electrodes are fabricated on another SOI wafer, diameter 100mm, with device layer 250 μ m, buried oxide layer 2 μ m and handle layer 300 μ m. There are two challenges in this: (i) fabricating the 250 μ m tall sidewall electrodes on the SOI wafer; and (ii) patterning the connecting wire and pad on the bottom and sidewall electrodes. For the high aspect ratio structure, it is impossible to pattern through PR and evaporate metal layers on the vertical surface. Thus, a high aspect ratio shadow mask and bulk sidewall electrode fabrication are used to form the sidewall electrodes.

Fabrication of the shadow mask: The shadow mask is fabricated by a single crystal silicon (SCS) based on bulk micromachining technique. The SCS wafer has a diameter 100mm with thickness 250 μ m. RIE and DRIE are used to pattern the shadow mask features.

Fabrication of the bulk sidewall electrode: A 2.5 μ m silicon dioxide layer is deposited by using PECVD on top of the device layer. Subsequently, a thicker PR (S1845) is patterned on top of the silicon dioxide layer. Next, RIE is used to etch the 2.5 μ m silicon dioxide layer. Finally, the structure of bulk sidewall electrodes is obtained by DRIE. The process is shown in Figures 3.4 (a)~(c).

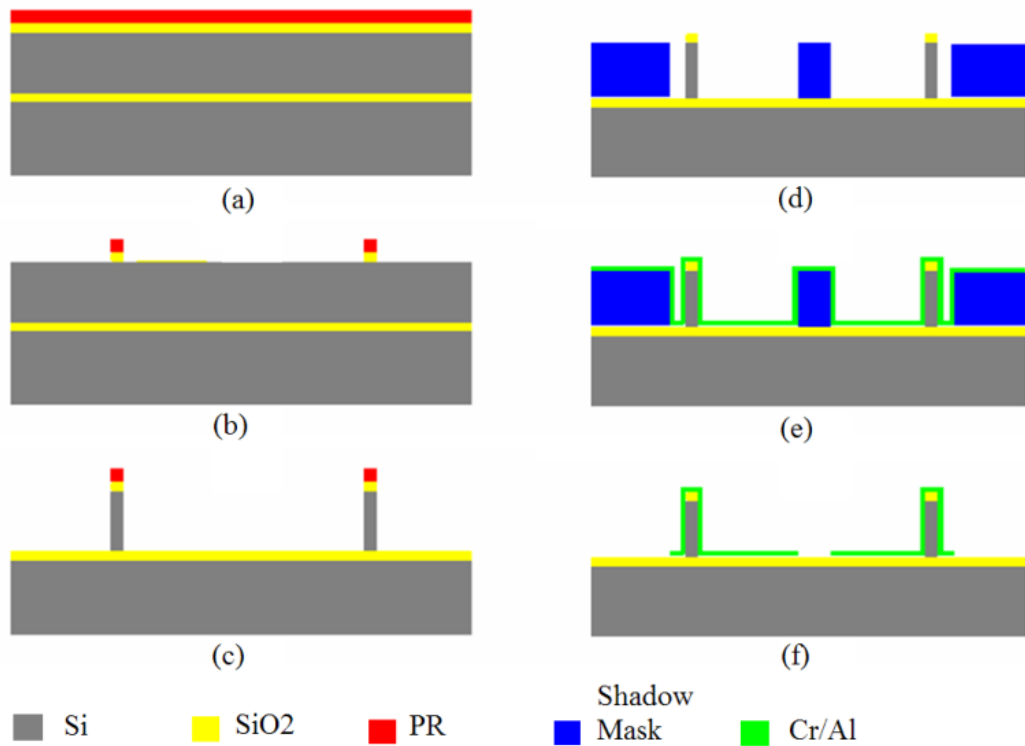
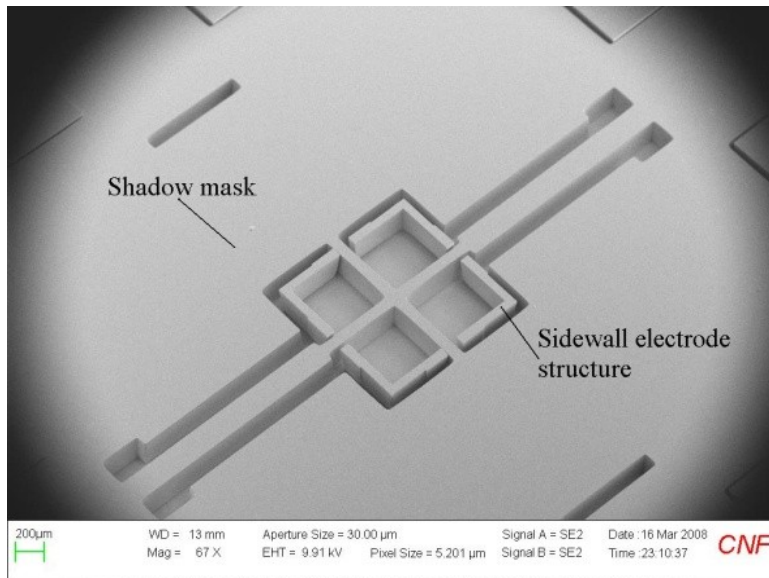


Figure 3.4: The sidewall electrodes fabrication process flow. (a)~(c) sidewall electrode fabrication by DRIE; (d)~(e) assembly of shadow mask and evaporation of metal Cr/Al as a conductive layer; (f) lift-off of the shadow mask to obtain the sidewall electrodes.

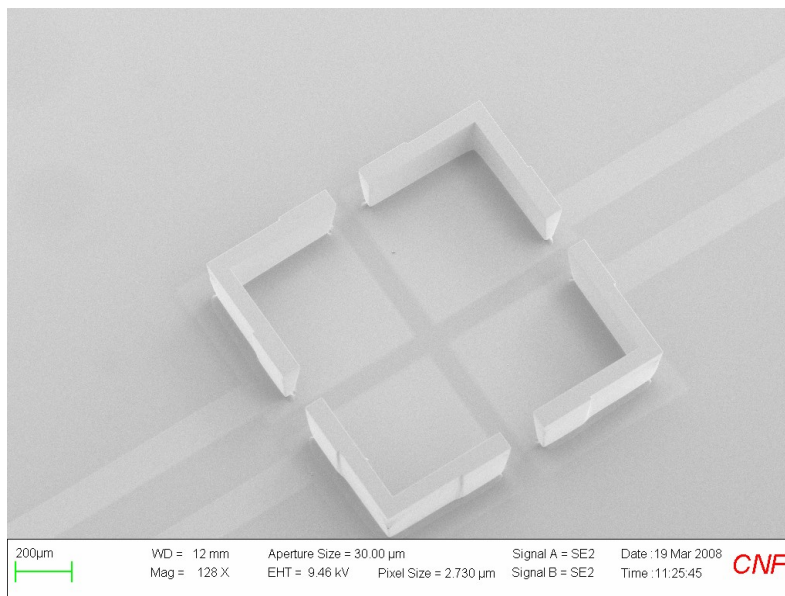
Assembly of a shadow mask on the sidewall electrodes: Figure 3.4 (d) and Figure 3.5 (a) present the assembling of a shadow mask on the sidewall electrode wafer. Cr or Ti (16nm) as an adhesive layer and Al layer (1~1.2 μm) are sputtered on the sidewall surface by using CVC Sputter Dep System. Figure 3.4 (e) shows the process. Finally, the shadow mask is removed by a lift-off process, shown in Figure 3.4 (f), and then the sidewall wafer is diced into single dies. Figure 3.5 (b) shows the pattern on the sidewall electrodes after lift-off the shadow mask.

3.3.3 Assembly of the Micromirror Plate and SW Electrodes

The last step is to assemble the micromirror plate and sidewall electrodes through using a transparent alignment tool built on a Pyrex glass wafer with four pins (height 50 μm) and the HTG System III-HR Contact Aligner (HTG). The assembly process resembles flip-chip method. The die of the sidewall



(a)



(b)

Figure 3.5: SEM of the sidewall electrodes. (a) assembly of the shadow mask and the sidewall electrode wafer; (b) the sidewall electrodes after shadow mask lift-off.

electrodes with a small quantity of epoxy glue, SU-8, is putted on top of HTG stage, and then the micromirror plate is stacked and aligned on the sidewall electrodes. Applied low pressure through the alignment tool, the micromirror plate is glued to the sidewall electrodes. Subsequently, the micromirror device is placed in a 90°C oven for 12 h. Figure 3.2 (a) shows the single micromirror with SW.

The yield rate is about 80% for the single micromirror with SW. The micromirrors are needed to store in a drying environment to keep Cr/Au reflective layer drying and clean.

3.4 Simulation and Experiment

Two types of micromirrors with SW having 3 μ m and 1.5 μ m torsion bars are fabricated at the Cornell Nanoscale & Sciences Facility (CNF). One micromirror without SW (only bottom electrodes), and having 3 μ m torsion bar and identical mirror parameters is also fabricated. Extensive experiments are performed to investigate the static and dynamic characteristics of the micromirror and verify the analytical modeling.

3.4.1 Experiment Configuration

The micromirror is driven by a differential drive method in order to obtain scan linearity [15]. The micromirror plate and the gimbal frame are electrically grounded. The drive voltages on the quadrant electrodes (sidewall and bottom electrodes) are denoted by V_1 , V_2 , V_3 and V_4 . The differential drive voltages are defined in Eq. (2.17).

In the experiment configuration, the MEMS mirror is controlled by signals generated by LabVIEW. A position sensitive detector (PSD) is used to measure the position of a laser spot reflected by the MEMS mirror. A data acquisition (DAQ) system is used to record the experimental data. Figure 3.6 shows the schematic experiment configuration.

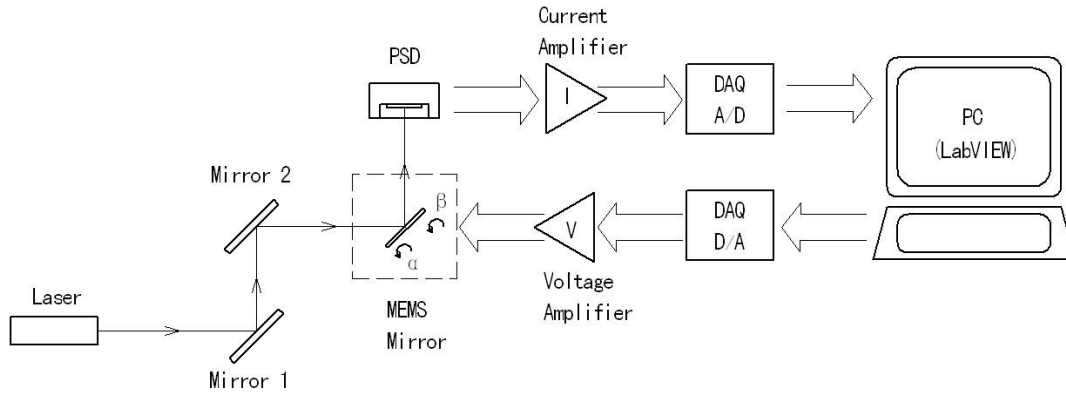


Figure 3.6: Schematic experimental configuration for characterizing the micromirror.

3.4.2 Static Characteristics

Only one quadrant of the micromirror is investigated because of the symmetry of the structure. Figure 3.7 illustrates the analytical modeling and experiment results for the static properties of the micromirror with $3\mu\text{m}$ torsion bar. Figure 3.8 shows the micromirror with $1.5\mu\text{m}$ torsion bar. For the case of the micromirror with $3\mu\text{m}$ torsion bar, as shown in Figure 3.7, the V_{bias} is 55V , and V_x and V_y range from 0 to 100V . When V_x and V_y are 100V , the α -scan angular deflection is about 0.80° and 0.87° , respectively, as shown in Figures 3.7 (a) and (c). The β -scan is 0.61° and 0.68° , respectively, as shown in Figures 3.7 (b) and (d). For the case of the micromirror with $1.5\mu\text{m}$ torsion bar, V_{bias} is 55V , and V_x and V_y range from 0 to 30V . When V_x and V_y are 25V , the α -scan angular deflection is about 1.71° and 2.68° , respectively, as shown in Figures 3.8 (a) and (c), while the β -scan is about 1.31° and 1.42° , as shown in Figures 3.8 (b) and (d).

From Figures 3.7-3.8, it is observed that: i) there is a good linearity under small scanning angles, with good-consistency between the analytical modeling and experimental results; ii) the mirror with $3\mu\text{m}$ torsion bar reaches a small angle under the differential voltage 100V , but the mirror with $1.5\mu\text{m}$ torsion bar achieves a large angle under 25V and the stiffness of spring constants affects the behavior of the mirror greatly.

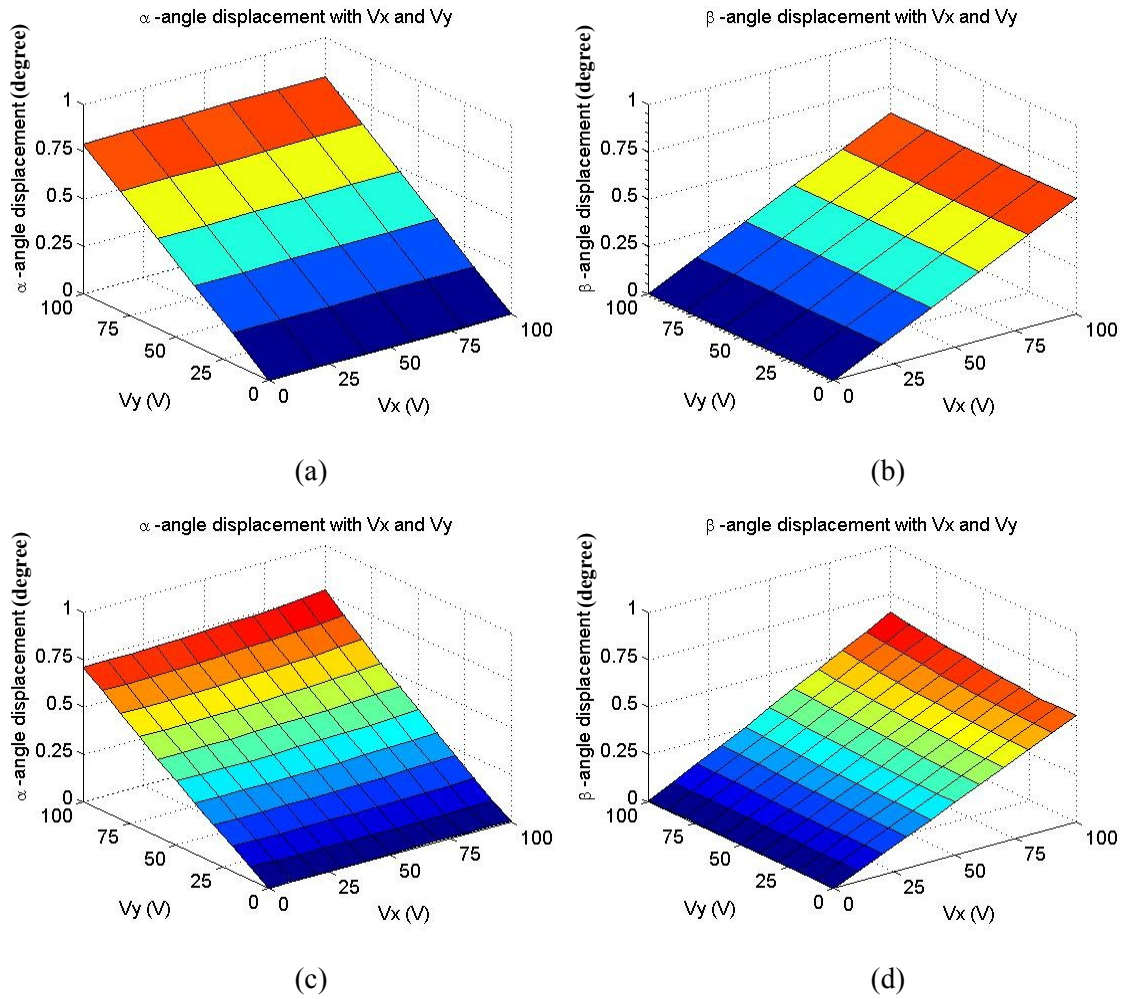


Figure 3.7: The linearity of the scanning angle and drive voltage for the micromirror with $3\mu\text{m}$ serpentine torsion bar. (a) α -scan angle displacement (from models); (b) β -scan angle displacement (from models); (c) α -scan angle displacement (from experiments); (d) β -scan angle displacement (from experiments).

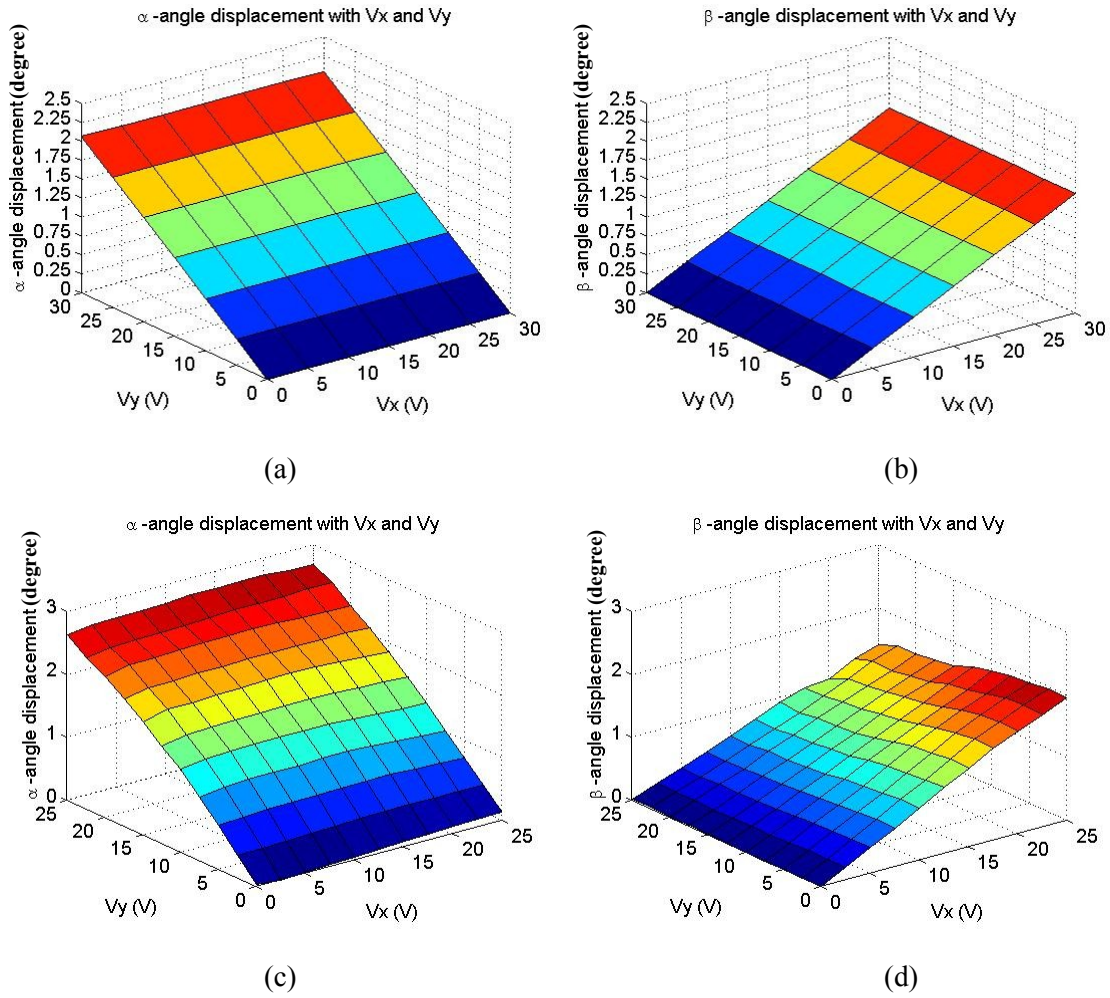


Figure 3.8: The linearity of the scanning angle and drive voltage for the micromirror with $1.5\mu\text{m}$ serpentine torsion bar. (a) α -scan angle displacement (from models); (b) β -scan angle displacement (from models); (c) α -scan angle displacement (from experiments); (d) β -scan angle displacement (from experiments).

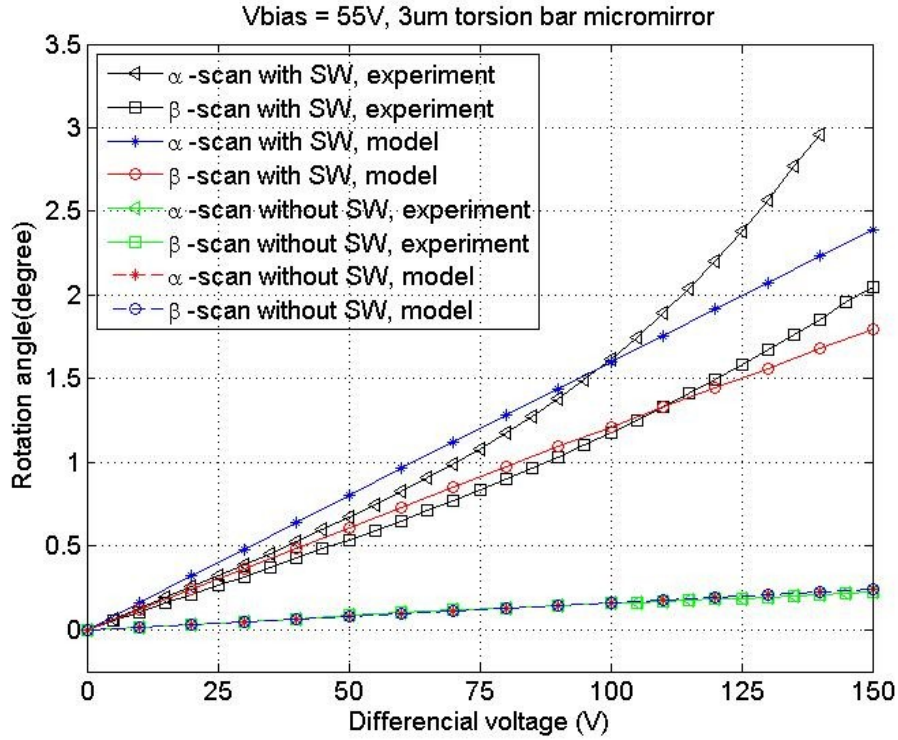
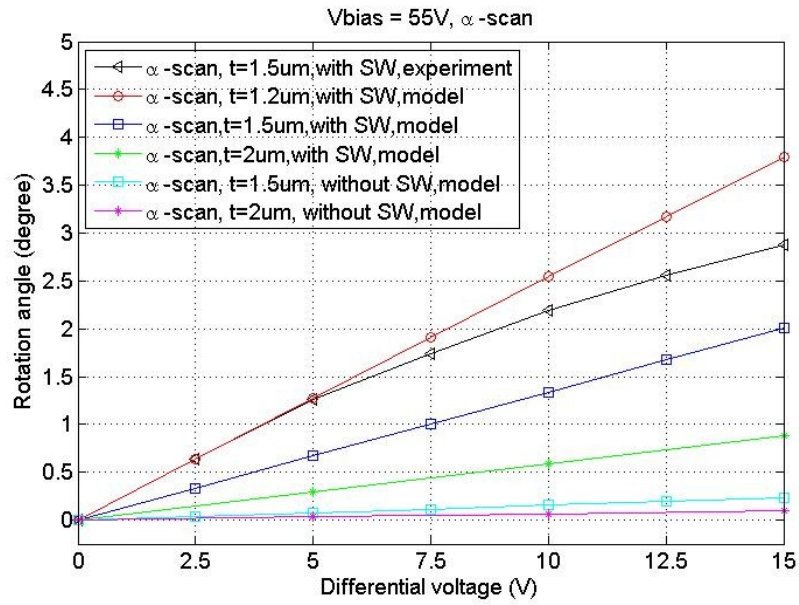
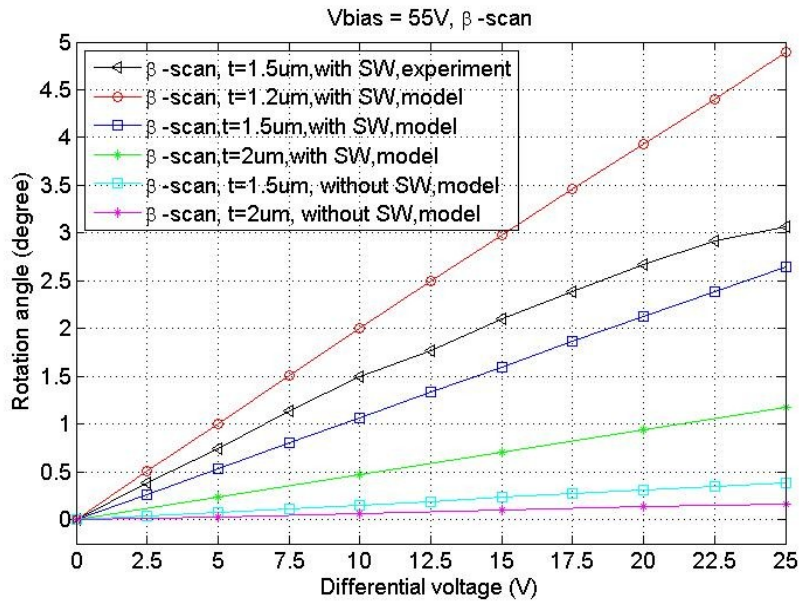


Figure 3.9: Scanning angle displacement under simple differential drive method for the micromirror with $3\mu\text{m}$ serpentine torsion bar. One group of curves are from micromirror with $3\mu\text{m}$ torsion bar with SW, the other from a $3\mu\text{m}$ torsion bar micromirror without SW (only bottom electrodes).

In addition, we adopted a simple differential drive method ($V_1 = V_{bias} + V_{diff}$, $V_2 = V_{bias} - V_{diff}$) for β - and α -scan, respectively [91]. The analytical modeling and experiment results are illustrated in Figure 3.9 and Figure 3.10. Figure 3.9 shows that the modeling agrees with the experiments but deviates at larger scanning angles. Figures 3.10 (a) and (b) show that the scan angle is large under small differential voltage. It is observed that the experiment results for the micromirror with $1.5\mu\text{m}$ torsion bars is between that of analytical modeling of the micromirror with $1.2\mu\text{m}$ and $1.5\mu\text{m}$ torsion bars. At small differential voltage, $0\text{V} \sim 7.5\text{V}$, the experiment result of α -scan is close to the simulation result of $1.2\mu\text{m}$ torsion bar, while the result between the experiment and analysis of β -scan is different. The discrepancy is due to i) the fabrication tolerance, namely, the actual width of each beam on a $1.5\mu\text{m}$ torsion bar ranges from $1.2\mu\text{m} \sim 1.5\mu\text{m}$, and ii) the α -scan electrostatic field with a large effective area involving the mirror plate and the gimbal frame, whereas, β -scan only the mirror plate. Moreover, the



(a)



(b)

Figure 3.10: Scanning angle displacement under simple differential drive method. The micromirror with SW is based on different widths of torsion bar, 1.2 μ m, 1.5 μ m, and 2 μ m. The micromirror without SW is based on 1.5 μ m and 2 μ m width torsion bars. (a) α -scan angle displacement; (b) β -scan angle displacement.

effects of the spring stiffness nonlinearity become larger along with increasing the scanning angle. However, although there are deviations at large scanning angle as shown in Figures 3.9-3.10, the analytical modeling is adequate for estimating the static characteristics of the micromirror with small angular deflection. Therefore, the analytical model can be used for determining the required micromirror parameters before an expensive fabrication run. Meanwhile, in comparison to the micromirror with only bottom electrodes, the micromirror with SW has demonstrated to achieve a larger scan angle for using the same drive voltage.

Pull-in properties: Figure 3.11 shows the large angular deflection for the micromirrors with $3\mu\text{m}$ 3-end torsion bars and $1.5\mu\text{m}$ 2-end serpentine bars. Figure 3.2 (c) shows the 2-end serpentine bar (a guided-end beam with one fixed end and one end with the mirror plate). In Figure 3.11 (a), the α -scan angular deflection of the micromirror with $3\mu\text{m}$ 3-end torsion bar has three phases: $0^\circ\sim 4.5^\circ$, $4.5^\circ\sim 6.5^\circ$, $6.5^\circ\sim 11^\circ$. In Figure 3.11 (b), for β -scan, the pull-in can be observed when the micromirror rotates about 5.5° . Such results are caused by the changes of electrostatic field distribution and the spring stiffness of different torsion bars. Figure 3.12 shows the changes of electrostatic field distribution under different α -scan deflection. The β -scan has a similar distribution, but without the gimbal frame. When the mirror plate rotates to α_1 (around 5.5°), the edge of the mirror plate is closest to the sidewall, as shown in Figure 3.12 (b). In this condition, the fringe field generates a maximum bending moment, M_o , to pull the mirror plate closer to the sidewall. Thus, the narrower the width of torsion bars, the smaller is the spring stiffness and thereby, the larger the lateral shift.

The experimental results in Figure 3.11 (b) have a convex shape because: i) the sidewall electrostatic field and fringe field can prevent the spring-softening effect [20]; and ii) the spring stiffness of the $1.5\mu\text{m}$ 2-end serpentine torsion bar has nonlinear property under large angular deflection. The width of a torsion bar affects both the ratio and linearity of the voltage-to-angle relationship. A smaller torsion bar width will decrease the required drive voltage to achieve a large angular rotation, however, it will also induce nonlinearity in the relationship.

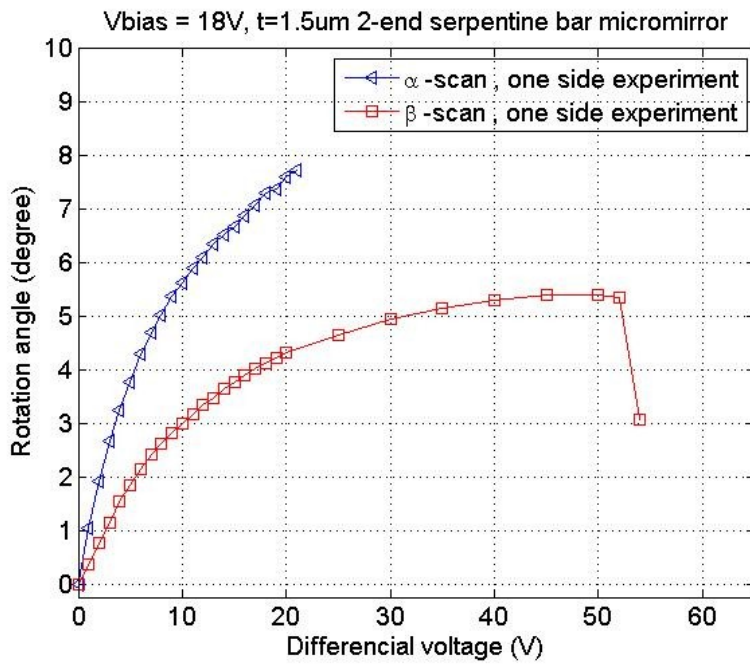
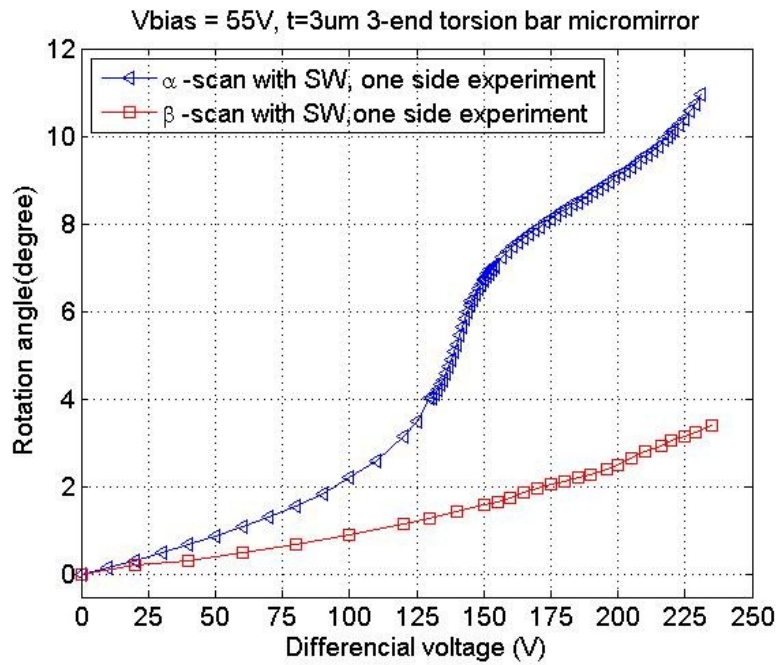


Figure 3.11: Large scan angle tests with simple differential drive method at α - and β - scan. (a) micromirror with $3\mu\text{m}$ 3-end torsion bar with SW, $V_{\text{bias}} = 55\text{V}$; (b) micromirror with $1.5\mu\text{m}$ 2-end serpentine bar with SW, $V_{\text{bias}}=18\text{V}$.

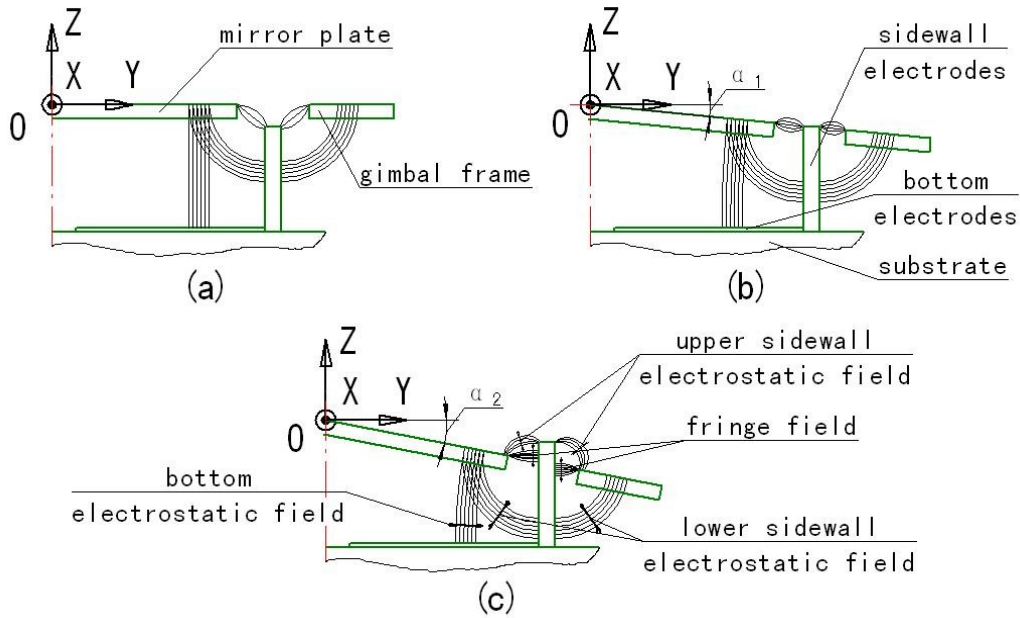


Figure 3.12: Electrostatic field distribution of one quadrant of the micromirror with SW under different angular deflection. (a) scanning angle 0° ; (b) scanning angle α_1 ; (c) scanning angle α_2 .

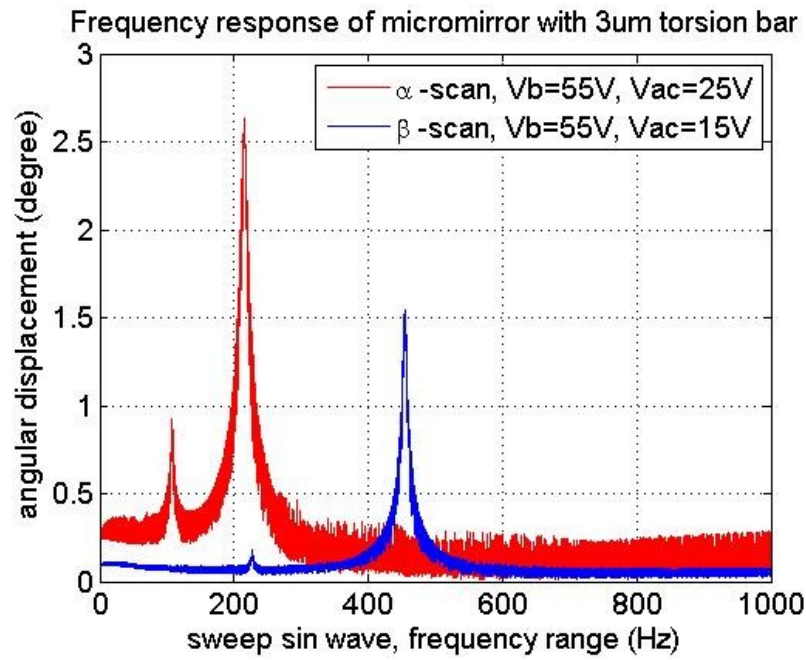
3.4.3 Dynamic Characteristics

There are two important characteristics of the dynamic properties of the micromirror: (i) the resonance frequency and (ii) resonance frequency shifting.

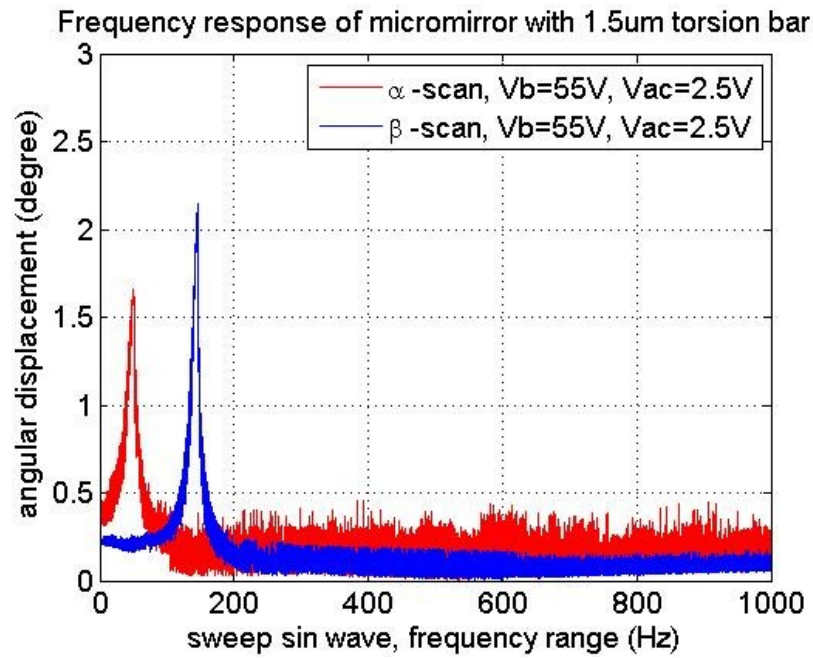
3.4.3.1 Resonance Frequency of the Micromirror

The dynamic response of the micromirror can be solved by through Eq. (3.6). To simulate the response of the micromirror, the following arbitrary initial values were assumed: $[x_1^0, x_2^0, x_3^0, x_4^0] = [0, 0.012, 0, 0.02]$. Eq. (3.4) can be solved by the Runge-Kutta method [81], to obtain the periods, T_α and T_β , and thereby the resonant frequency, under different bias voltages, f_α and f_β ($T_\alpha = 1/f_\alpha$, $T_\beta = 1/f_\beta$) [81].

In order to find the system resonance frequency experimentally, the micromirror is actuated by DC and AC voltages. The sinusoidal AC voltage has a frequency range of 1- 1000Hz. The peak voltages show the resonant frequency response of the α -scan and β -scan, as shown in Figure 3.13. Thus, the



(a)



(b)

Figure 3.13: The frequency response of micromirror with $3\mu\text{m}$ torsion bar and $1.5\mu\text{m}$ torsion bar under sinusoidal sweep experiments for a frequency range of 1Hz to 1000Hz. (a) Micromirror with $3\mu\text{m}$ torsion bar; (b) Micromirror with $1.5\mu\text{m}$ torsion bar.

resonance frequency under different DC bias voltage is tested. The micromirror with $3\mu\text{m}$ 3-end torsion bar has the resonance frequency 454.6Hz at β -scan, 215.4Hz at α -scan, the micromirror with $1.5\mu\text{m}$ 3-end torsion bar has the resonance frequency 146.5Hz at β -scan, 50.2Hz at β -scan, under DC bias voltage 55V. In addition, for one micromirror with $3\mu\text{m}$ torsion bars running at the resonance frequency, the scanning angle reaches $\pm 12^\circ$ (mechanical angle, $V_{\text{bias}}=55\text{V}$ $V_{\text{ac}}=35\text{V}$, $f_{r\alpha}=181\text{Hz}$) at α -scan, and $\pm 20^\circ$ (mechanical angle, $V_{\text{bias}}=80\text{V}$ $V_{\text{ac}}=80\text{V}$, $f_{r\beta}=383\text{Hz}$) at β -scan.

3.4.3.2 Resonance Frequency Shifting

The resonant frequency changes under different bias voltages [96]. This is an important property of MEMS mirrors actuated by electrostatic forces. The resonance frequency determines the scanning frequency bandwidth of the micromirror. The larger the resonance frequency shifting, the smaller is the bandwidth. It is known that micromirrors without SW have large range resonance frequency shifts. However, although the micromirror with SW still exhibits this phenomenon, it is much smaller, i.e. the sidewall electrodes suppress resonance frequency shifting, in that the fringe field effects from sidewall electrodes affect the stiffness of the tiny torsion bars. Figure 3.14 illustrates this under different bias voltages, showing good agreement between ANSYS simulation and experiments in terms of the values of Table 3.3. In addition, from the dynamic tests for the micromirror without SW, the resonance frequency shifting cannot be observed: the reason is the large gap between the mirror plate and bottom electrodes, around $300\mu\text{m}$. The generated electrostatic force is small and has very weak contribution for changing the resonance frequency through different bias voltages.

In fact, the resonance frequency under different bias voltages can be obtained by solving Eq. (3.4). It also indicates that the resonance frequency shift is negligible. Figure 3.15 shows the 3-D profile of the mirror with SW that was acquired from the Olympus *LEXT* OLS3100 confocal microscope. The height between the mirror plate and the edge top of the sidewall electrodes is about $55\mu\text{m}$. However, in the analytical models, we assume that the effective integral domain is enclosed by the micromirror edges and the projected lines of the lower sidewall electrostatic field [76], and ignore upper sidewall

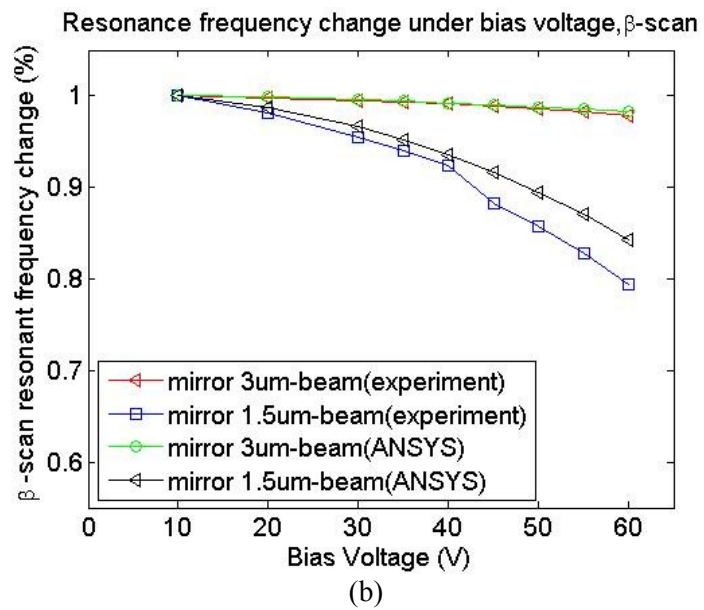
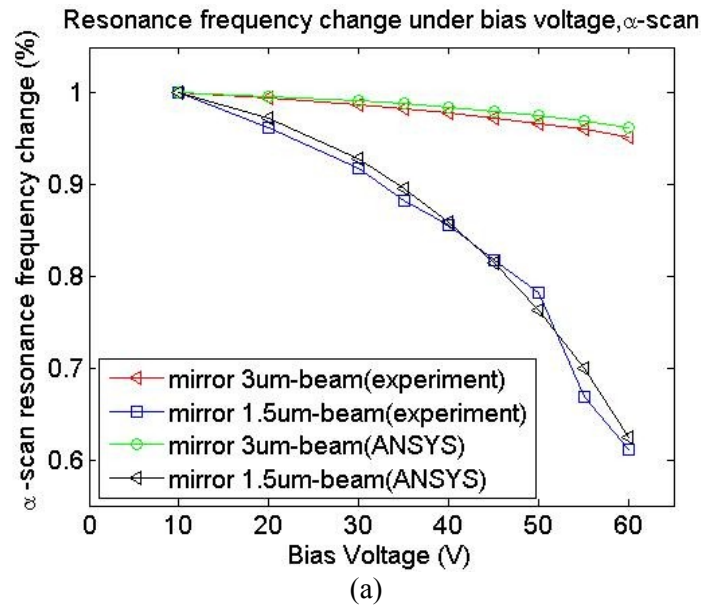


Figure 3.14: The resonance frequency shifting under different bias voltages (ANSYS and experiments). (a) Resonance frequency shifting of α -scan; (b) Resonance frequency shifting of β -scan.

Table 3.3: α -scan and β -scan resonance frequency values under different bias voltages

Bias voltage (V)	Micromirror with 3 μ m width torsion bars				Micromirror with 1.5 μ m width torsion bars			
	α -scan, resonance frequency(Hz) (mirror plate with gimbal frame)		β -scan, resonance frequency(Hz) (mirror plate)		α -scan, resonance frequency(Hz) (mirror plate with gimbal frame)		β -scan, resonance frequency(Hz) (mirror plate)	
	Experiment	<i>ANSYS</i>	Experiment	<i>ANSYS</i>	Experiment	<i>ANSYS</i>	Experiment	<i>ANSYS</i>
10	224.2	247.4	462.8	584.9	75	82.7	176.8	203.5
20	222.9	246.6	461.9	584.0	72.2	80.5	173.5	201.0
30	221.5	245.3	460.5	582.6	68.8	76.7	168.8	196.7
35	220.5	244.5	459.6	581.6	66.2	74.2	166.2	193.8
40	219.4	243.5	458.7	580.5	64.2	71.1	163.3	190.4
45	218.1	242.4	457.7	579.2	61.3	67.4	156	186.6
50	216.6	241.5	456.5	577.8	58.7	63.1	151.5	182.1
55	215.4	239.7	454.6	576.2	50.2	57.9	146.5	177.1
60	213.5	238.2	453	574.5	45.8	51.7	140.4	171.4

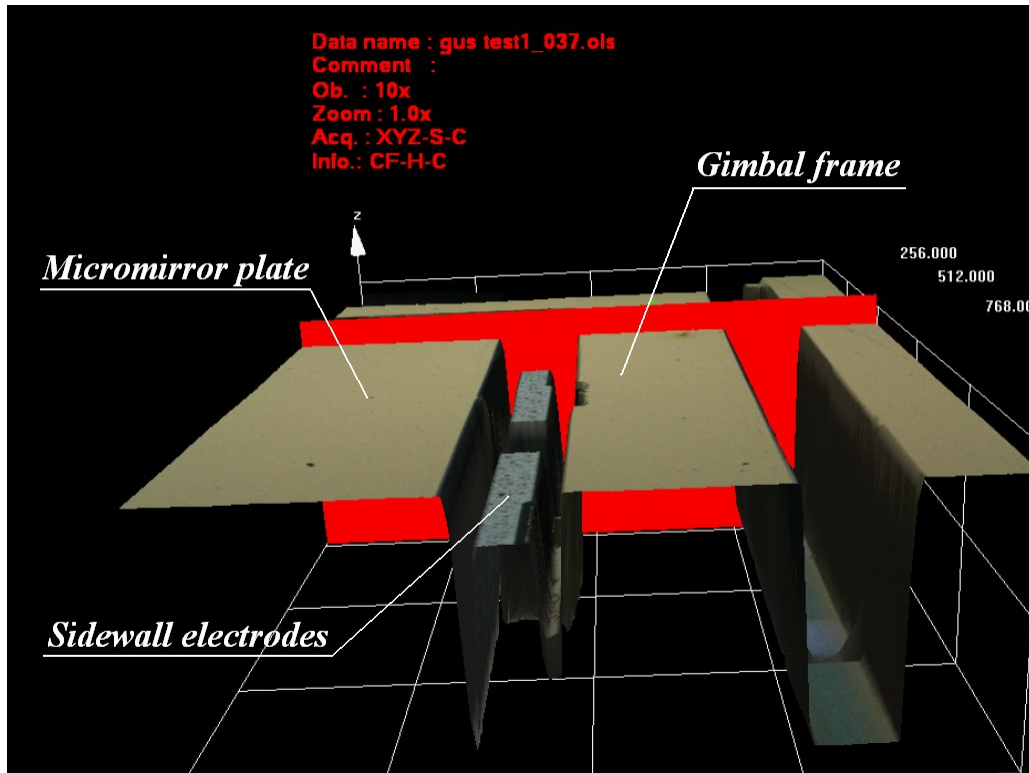


Figure 3.15: 3D profile of the mirror with SW acquired from an Olympus LEXT OLS3100 confocal microscope, and the distance between the mirror plate and the top of sidewall electrodes.

electrostatic field and fringe field effects. This assumption is a major contributor to the differences among the analytical modeling, experiments, and ANSYS simulation.

In addition, the ANSYS simulation results are larger than the measurements. These differences are attributed to discrepancies in the estimation of material parameters and fabrication tolerance.

3.5 Conclusions

In terms of both the analytical modeling and the experiments, the characteristics of the MEMS micromirror with SW are determined by several factors: the cross section (width and thickness) and length of the serpentine torsion bars, the distance between the mirror plate and bottom electrodes, and the height of sidewall electrodes. The higher the sidewall electrodes, the smaller are the electrostatic

field effects of the bottom electrodes and the smaller the resonance frequency shifting. Within a small scanning angle range, the mirror scan is linear under differential voltage drive, but, as the scanning angle is increased, nonlinearity is observed. Although there are differences between the analytical models and the experiments, they are very consistent at small scanning angles. In this domain, the analytical modeling describes the system very well and can be used as a very good reference during the design phases before a commitment to a fabrication runs. It is also shown that the height of the sidewall electrode affects the pull-in threshold during the large angular deflection.

3.6 Summary

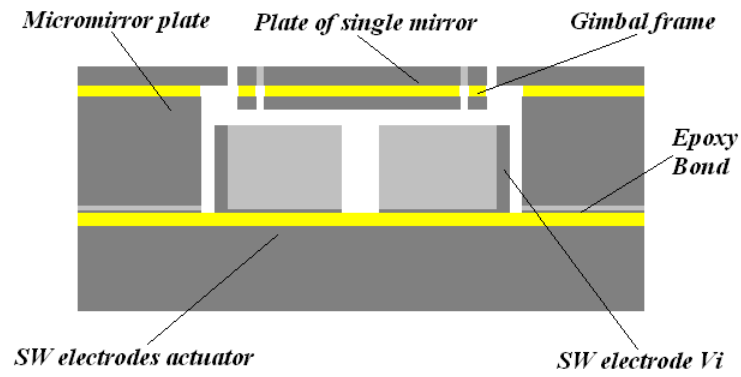
A novel biaxial MEMS mirror with SW electrodes has been fabricated successfully in terms of a new fabrication process. The static and dynamic characteristics of the micromirror with SW electrodes are obtained. In the following chapters, the extended fabrication process succeeds in achieving micromirror arrays, and also a biaxial MEMS mirror with SW electrodes is used into a laser scanning microscope system – the MACROscope system.

Chapter 4

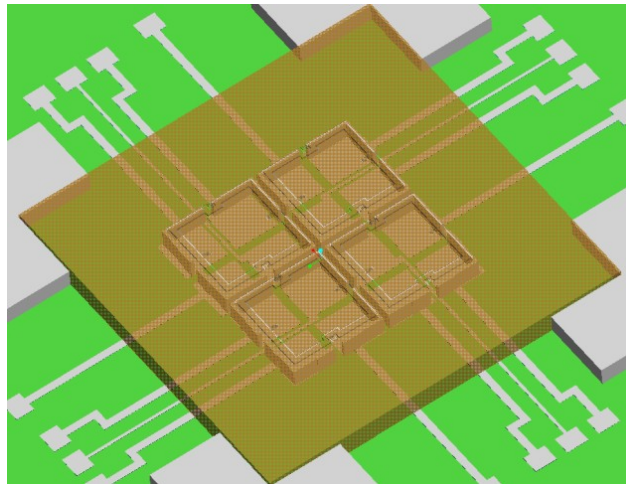
Design and Fabrication of 2×2 and 4×4 Micromirror Array

4.1 Introduction

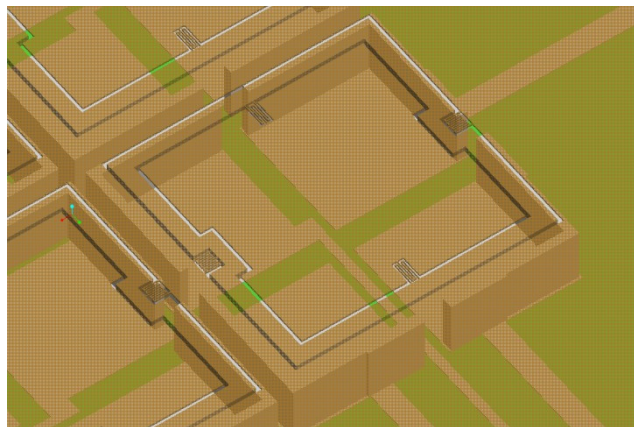
2×2 and 4×4 micromirror arrays based on the extended fabrication process are fabricated in order to get a large optical aperture that is the requirement of the EOCT and confocal microscope for obtaining high resolution images [67]. The optical aperture is determined by a micromirror plate. However, the larger the micromirror plate, the lower resonance frequency the micromirror has. To simulate a large aperture tilt micromirror, micromirror arrays divide a large aperture into small micromirrors with significantly reduced inertia and increase rotation speed. Different types of micromirror arrays apply to optical switches, DMD, adoptive optics (AO) [3], telescope [114, 115], and optical phased arrays [116, 117]. DMD developed by Texas Instrument Inc is widely adopted into digital light projector (DLP) and confocal microscopy [118]. Each mirror in DMD is only 10μm or a little bit large with “on” or “off” state. Optical phased array technology was developed by Paul F. McManamon *et al.* [119]. Micromirror arrays can be used as optical phased arrays for laser beam steering. Several types of micromirror arrays are fabricated in terms of surface micromachining or hybrid bulk/surface micromachining techniques [12, 22, 114-117, 120]. Micromirror arrays process several advantages: low inertia, high frequency, and large field of view (FOV). Therefore, applying a micromirror array to Endoscopic OCT and confocal microscope becomes the motivation of design



(a)



(b)



(c)

Figure 4.1: The structure of 2×2 micromirror array. (a) schematic of one micromirror element; (b) overview of 2×2 micromirror array; (c) close-up view of one micromirror on the right corner.

and fabrication of 2×2 and 4×4 micromirror arrays.

This chapter presents the design and fabrication of 2×2 and 4×4 micromirror array. Although the process flow of micromirror arrays is based on that of the single micromirror with SW electrodes [82], relevant modification and plenty of optimization on the mirror array design and fabrication parameters are required.

4.2 Design of Micromirror Arrays

The schematic design of 2×2 micromirror array is shown in Figure 4.1. The micromirror array is composed of a mirror plate array and sidewall electrodes. The size of one mirror plate in the array is 1mm×1mm, which is supported by two pairs of 3-end serpentine torsion bars, and the total optical aperture combined from four micromirrors is close to 2mm×2mm. The gap between the mirror plate array and bottom electrodes is about 300μm, which makes each micromirror have a large scan angle potentially. The width of the torsion bar is designed to 2μm. Figure 4.1 (a) illustrates a cross-view of one micromirror, and Figure 4.1 (c) shows a close-up view on the right corner micromirror. Figures 4.3 (b) and (c) show outer and inner 3-end serpentine torsion bars. In order to control each micromirror, the mirror plate array is an electrical ground and each cell of 2×2 SW electrode actuators is insulated. The driving voltages, V_1, V_2, V_3 and V_4 , are added onto each actuator, respectively. Figure 4.3 illustrates 2×2 micromirror array bonded in a chip carrier. In addition, the fill factor is an important parameter for micromirror array devices. Fill factor can be calculated through equation [117]:

$$f = \left(\frac{a}{a + b} \right)^2 \quad (4.1)$$

in which a is the size of each sub-aperture, and b is the spacing between adjacent pixels. Due to the electrostatic actuators, a can be in millimeter scale. The choice of b is subjected to several factors including the robustness of the silicon walls, manufacturability and process tolerances. In a 2×2

micromirror array, $a=1\text{mm}$ and $b=335\mu\text{m}$, rendering a fill factor of 56%. However, for a 4×4 micromirror array, $a=1\text{mm}$ and $b=1.4\text{mm}$, rendering a fill factor of 17%.

4.3 Fabrication of 2×2 Micromirror Array

The fabrication process of 2×2 micromirror array is based on that of the single micromirror with SW electrodes and is composed of micromirror array fabrication, SW electrode fabrication, and assembly of micromirror array and SW electrodes. This section emphasizes the fabrication process specialties and difference between single micromirrors and micromirror arrays.

4.3.1 Micromirror Array Fabrication

The micromirror array is built on a double side polished (DSP) SOI wafer, 100mm diameter, with $12\mu\text{m}$ device layer, $0.5\mu\text{m}$ buried oxide layer, and $290\mu\text{m}$ handle layer. The process, as shown in Figure 4.2, is based on reactive ion etching (RIE) and high aspect ratio deep reactive ion etching (DRIE).

Shallow trench etched on top of the handle layer: A layer of $0.5\mu\text{m}$ silicon dioxide (SiO_2) is deposited by GSI PECVD on top of the device layer. S1818 Photoresist (PR) is patterned on top of the handle layer to define a shallow trench area. Bosch Etching DRIE follows next to etch the shallow trench, depth $8\text{-}9\mu\text{m}$. The first depth is created, as shown in Figures 4.2 (a) and (b). Then, the remained PR is cleaned by Hot Tank. A layer of $2\mu\text{m}$ SiO_2 is deposited by GSI PECVD on top of the fabricated handle layer, as shown in Figure 4.2 (c).

2×2 micromirror array patterned on top of the device layer: S1813 PR is patterned on the device layer. RIE is used to etch SiO_2 as a mask for the next DRIE etching. DRIE etching silicon stops on the buried oxide layer. This process forms tiny serpentine torsion bars, the mirror array and the gimbal frame on the device layer, as shown in Figures 4.2 (d) and (e). The diagrams in Figure 4.3 show the pattern of 2×2 micromirror array.

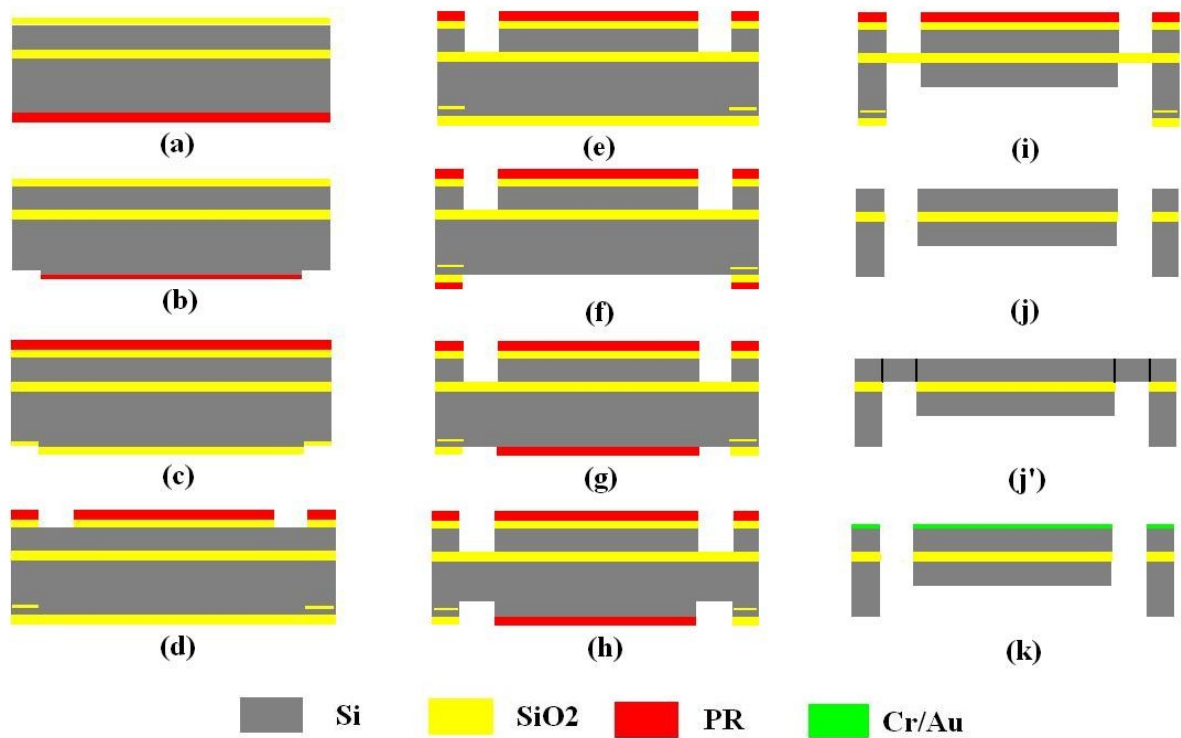
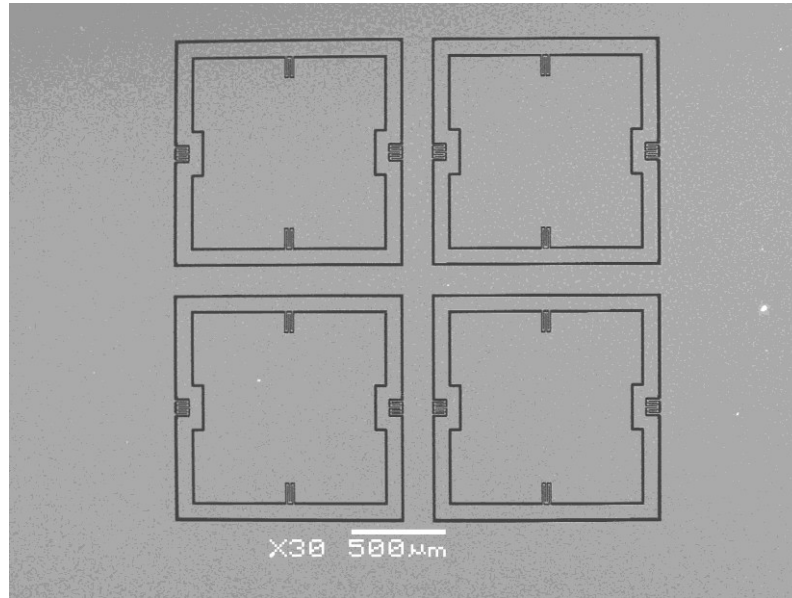


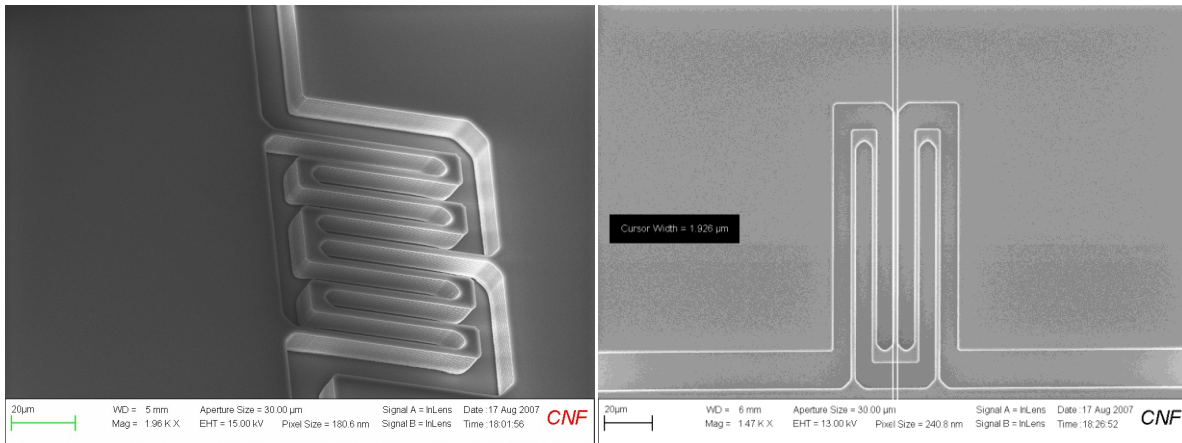
Figure 4.2: The fabrication process flow of 2×2 and 4×4 micromirror arrays

Backside features of 2×2 micromirror array etched on top of the handle layer: Subsequently, S1818 PR is patterned on the handle layer to define backside features of the micromirror array. RIE is used to etch the $2\mu\text{m}$ silicon dioxide layer to expose the silicon handle layer, as shown in Figure 4.2 (f). PR is patterned on the exposed silicon to define the backside patterns of the micromirror array and the gimbal frame, as shown in Figure 4.2 (g). DRIE is used to etch the silicon on the backside. The depth of the DRIE trenches around the mirror array and the gimbal frame is $60\text{-}65\mu\text{m}$, as shown in Figure 4.2(h). PR on the backside is stripped and then DRIE is used to etch the exposed silicon to a depth of $290\mu\text{m}$, as shown in Figure 4.2 (i). The backside features of 2×2 micromirror array after DRIE etching is illustrated in Figure 4.4. DRIE etching stops at the buried oxide layer. A $35\mu\text{m}$ thick micromirror plate is created at this point. As shown in Figure 4.4 (c), four layers on the backside are created from three masks. In terms of the literatures, the maximum layers are three, and it is the first

time to get four layers through DRIE for fabricating complex structures. After DRIE etching, the buried oxide layer is exposed and shown in Figure 4.5. The thermal SiO₂ layer is a compressive unstressed layer. After exposed, it becomes a buckled thin film, as shown in Figure 4.5(b). The tiny serpentine torsion bars will be damaged if the deformation of the thin film is too big. This effect has to be considered when designing 3-end serpentine torsion bars.



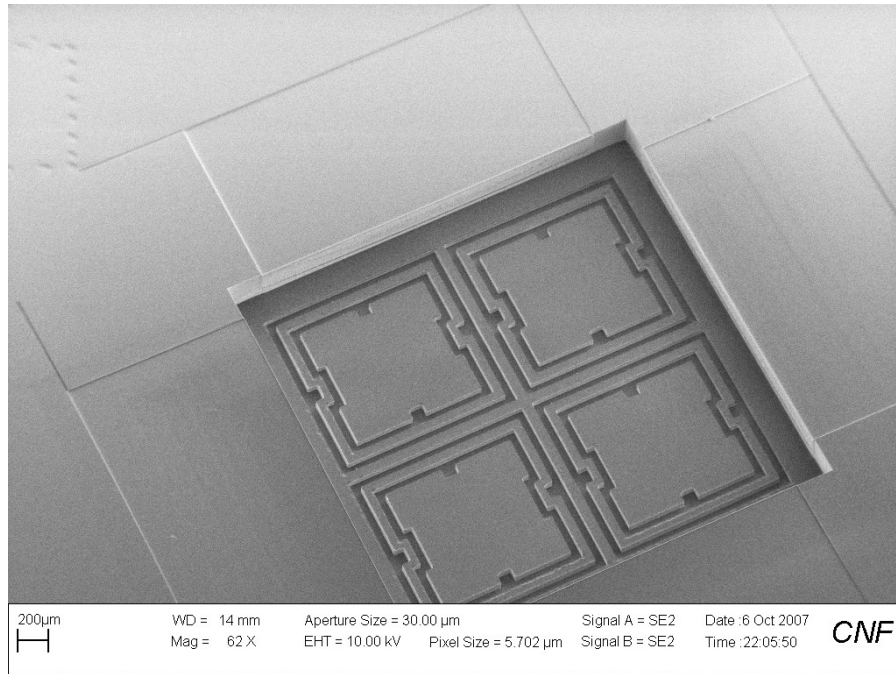
(a)



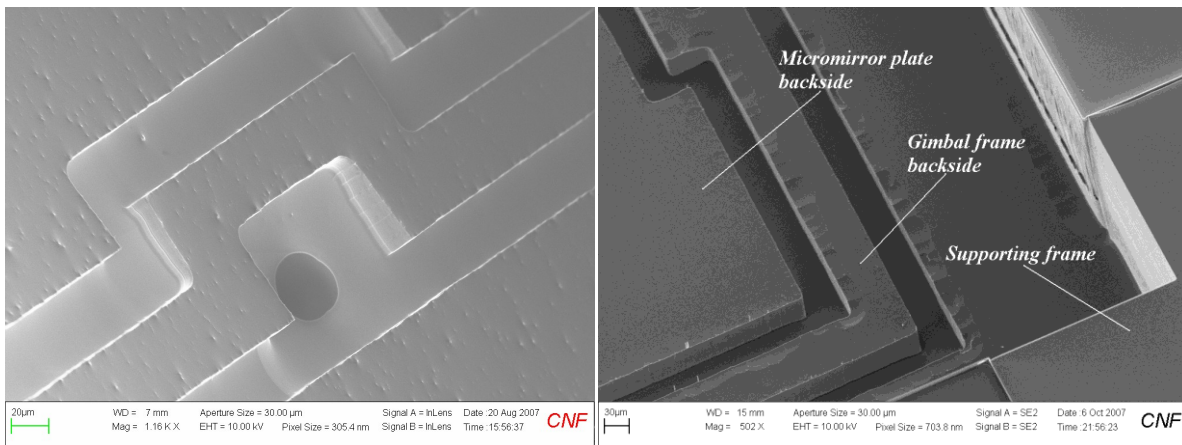
(b)

(c)

Figure 4.3: The front side features and critical 3-end serpentine torsion bars. (a) SEM of 2×2 micromirror array; (b) outer serpentine torsion bar; (c) inner serpentine torsion bar.



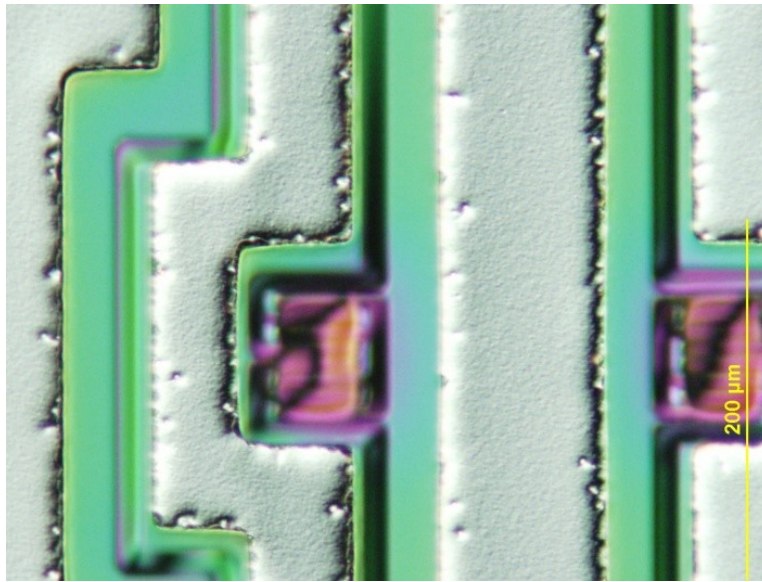
(a)



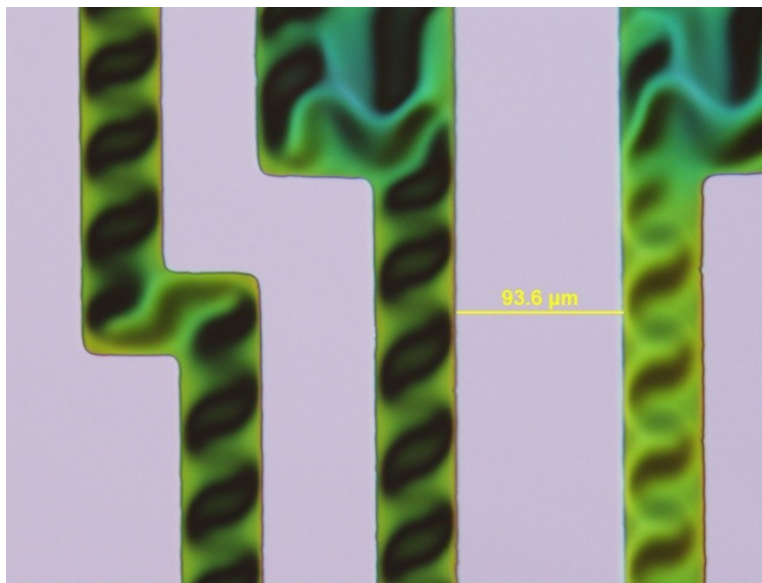
(b)

(c)

Figure 4.4: The backside features of the micromirror array plate after DRIE. (a) SEM of the backside feature of the micromirror array plate; (b) close-up view of the backside gimbal frame and mirror plate on the serpentine torsion bar area; (c) overview of the corner on the mirror plate backside.



(a)



(b)

Figure 4.5: The compressive unstressed SiO₂ thin film exposed after DRIE. (a) backside view on the serpentine torsion bar area; (b) frontside view close to serpentine torsion bars.

Release of the micromirror plate array: The micromirror array is released by a wet etching method. 6:1 Buffered Oxide Etchant (BOE) is adopted. After releasing the micromirror array from the SOI wafer, DI water and pure alcohol are used to dry the surface, as shown in Figure 4.2 (j). Figure 4.2 (j') shows the cross-sectional view of the device when rotated by 90°.

Evaporation of the reflective metal layer: The subsequent step is to evaporate the reflective metals, for which Cr or Ti (16nm) is evaporated by a CVC4500 evaporator as an adhesive layer, and then Au (150nm) as a reflective surface. Figure 4.2 (k) shows this process. The thickness of the reflective thin film affects the micromirror curvature, while the thin film quality influences the surface reflectivity.

4.3.2 Sidewall Electrode Fabrication

The sidewall electrodes are fabricated on another SOI wafer, diameter 100mm, with 250 μ m device layer, 2 μ m buried oxide layer and 300 μ m handle layer. RIE and DRIE are adopted to form the sidewall features. The layer of 2.5 μ m silicon dioxide is deposited by PECVD on top of the device layer, and then, a thicker PR (S1845) is patterned on top of the SiO₂ layer to pattern the sidewall features. Next, RIE is used to etch the 2.5 μ m SiO₂ layer. Finally, the bulk sidewall electrode with 250 μ m height is obtained by DRIE. The process is shown in Figures 3.4 (a)~(c). Figure 4.8 (a) shows the bulk sidewall electrodes after DRIE etching.

In order to get bulk sidewall electrodes, sacrificial walls are designed to enclose the sidewall. After a long time DRIE, the etch rate is faster at three-fourth position of the entire wafer than at the center and the edge. There exists a 10-20 μ m difference in the etched depth on the whole wafer. Moreover, the feature density on the wafer affects DRIE etch rate. The diagrams in Figures 4.8 (b) and (c) illustrate that the difference of etch rate affects final structure pattern. At the high density area does the undercut show up while vertical walls at the low density area.

A shadow mask is adopted to pattern wires, pads, and bottom electrode features on the high-aspect-ratio bulk sidewall electrodes. The shadow mask is fabricated on single crystal silicon (SCS), diameter 100mm, thickness 250 μ m and 285 μ m. Although a silicon shadow mask has been reported in [121], the characteristics of the shadow mask for the bulk sidewall electrodes are thicker and applied on top of the wafer with high-aspect-ratio bulk features. RIE and DRIE are used to pattern the shadow mask features. Two methods are adopted during the fabrication, as shown in Figure 4.6 and Figure 4.7. Figure 4.6 shows a dry etching process flow with RIE and DRIE. Figure 4.7 shows a hybrid wet etching and dry etching process flow. The big difference between two methods is to get different

thickness of shadow masks. Dry etching process, Method I, adopts a 250 μm or 285 μm DSP SCS wafer. If fabricating a thinner shadow mask, the thin silicon wafer is expensive and maybe required to grind to expected thickness. Method II shows a little bit complex process, based on 500 μm SSP SCS wafer, but the thickness can be fabricated thinner than 20 μm .

Subsequently, the shadow mask is assembled on the sidewall electrodes. The HTG System III-HR Contact Aligner (HTG) is used to align the shadow mask with the sidewall electrodes wafer, as shown in Figure 3.4 (d). Cr or Ti (16nm) as an adhesive layer and Al layer (1~1.2 μm) are sputtered on the sidewall surface by CVC Sputter Dep System. Figure 3.4 (e) shows the process. Finally, the shadow mask is removed by a lift-off process and the sidewall wafer is cut into single dies. The process is shown in Figure 3.4 (f).

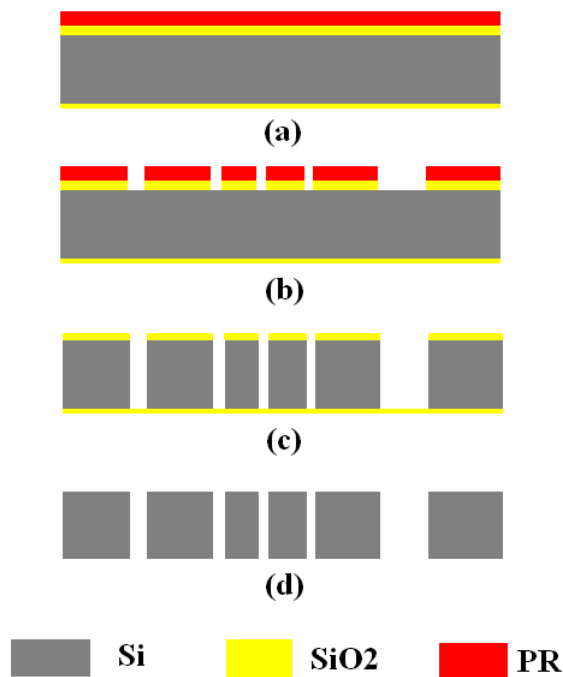


Figure 4.6: The fabrication process flow of shadow mask based on dry etching (method I)

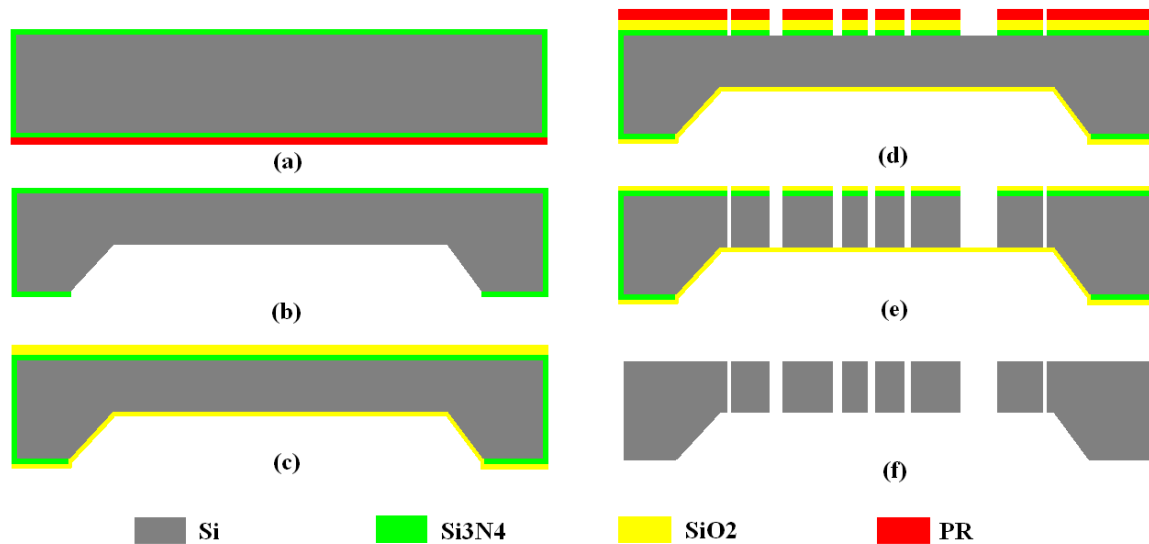
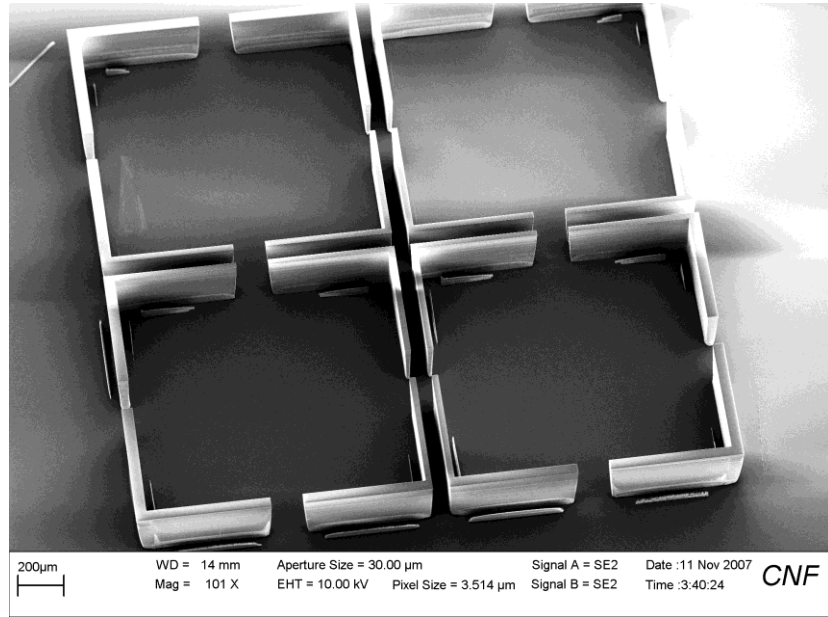


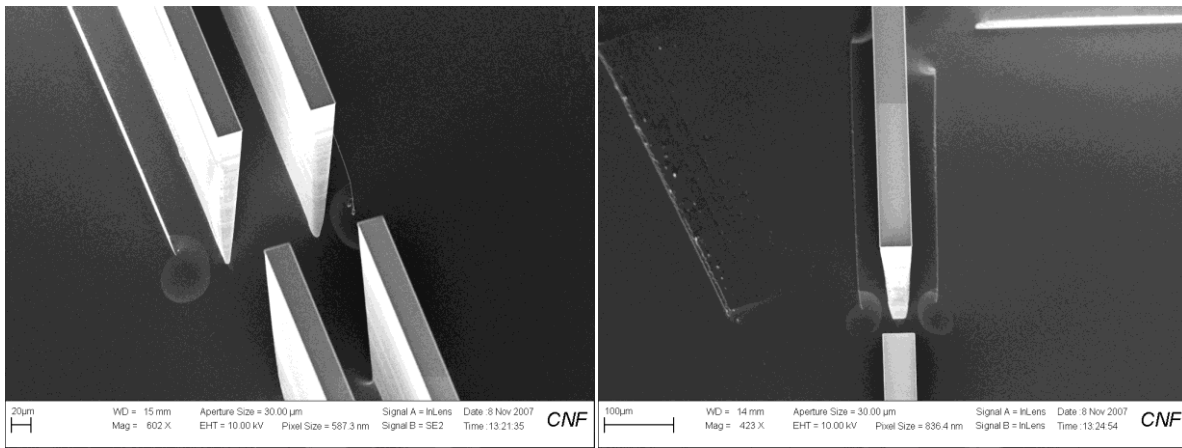
Figure 4.7: The fabrication process flow of shadow mask based on hybrid wet etching and dry etching (method II)

4.3.3 Assembly of Micromirror Array and SW Electrodes

The last step is to assemble the micromirror array and SW electrodes through a transparent alignment tool with four pins and HTG contact aligner. A few droplets of epoxy glue, SU-8, are deposited on the SW electrode die, and then the micromirror array is stacked on top. Subsequently, the micromirror array with SW electrodes is moved to HTG stage. The micromirror array could be aligned with the SW electrodes. Figure 4.9 shows an alignment mark on the SW electrodes. With low pressure applied through the alignment tool, the micromirror plate is glued to the sidewall electrodes. Finally, the micromirror device is placed in a 90°C oven for 12 h. The yield rate of 2×2 micromirror array is about 60% after all the process. The 2×2 micromirror array with SW is shown in Figure 4.10.



(a)



(b)

(c)

Figure 4.8: The bulk sidewall electrodes after fabrication process. (a) SEM of 2×2 sidewall electrode array; (b) SEM of the bulk sidewall electrodes at the center; (c) SEM of the bulk sidewall electrode at the corner.

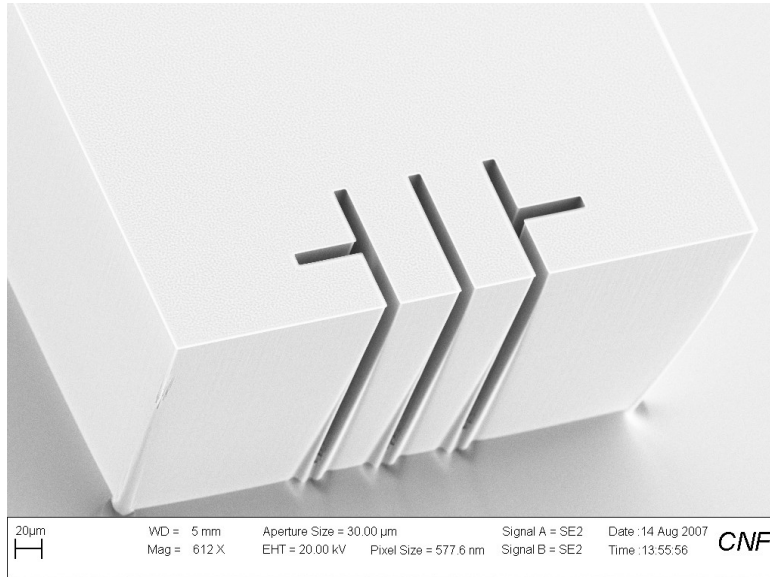


Figure 4.9: SEM of alignment mark on the SW electrodes

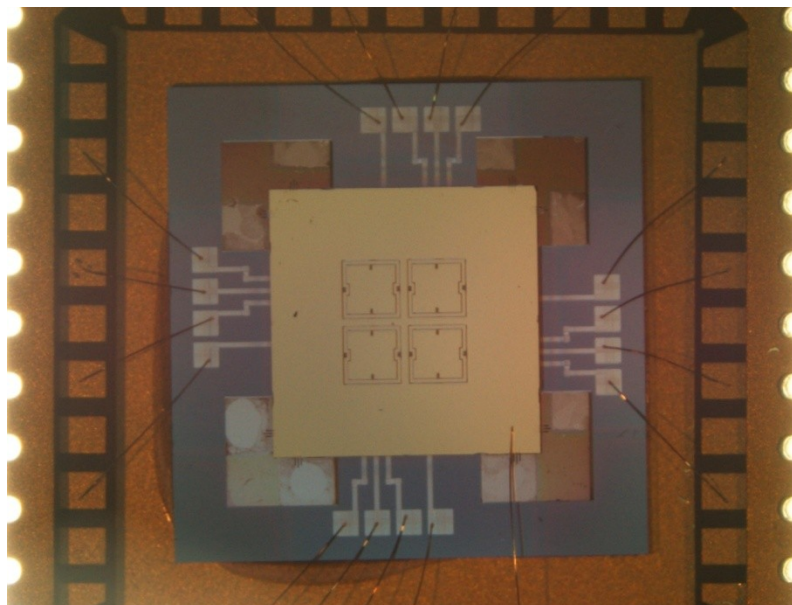
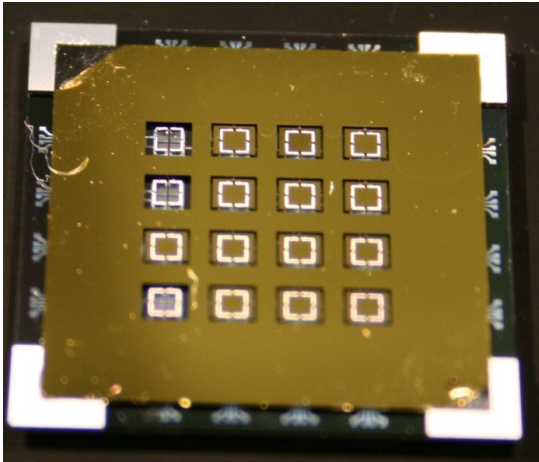


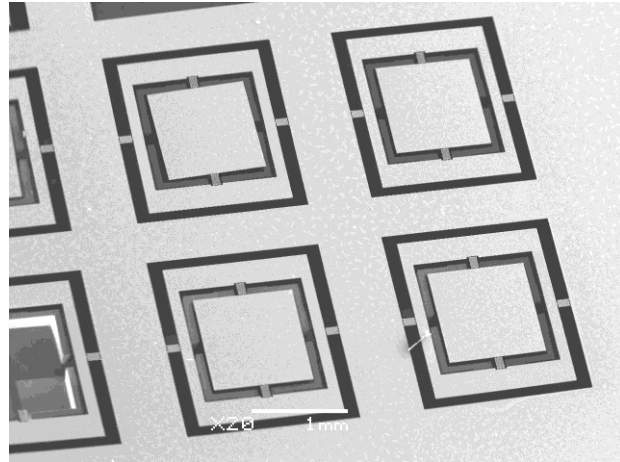
Figure 4.10: Photograph of 2x2 micromirror array after wire bonding in a chip carrier.

4.4 Fabrication of 4×4 Micromirror Array

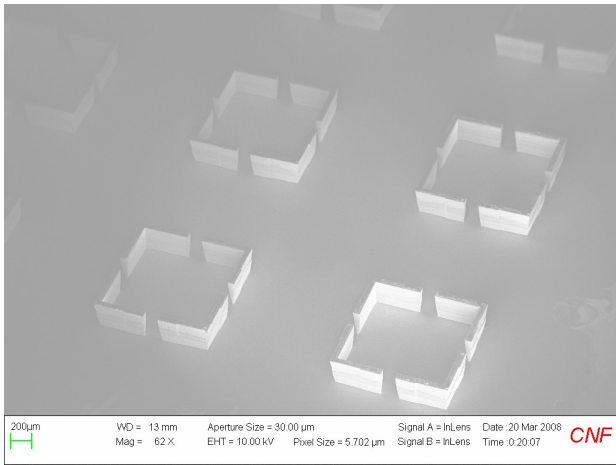
The design of 4×4 micromirror array has a gimbal structure to realize a biaxial rotation. Each of micromirrors has the same structure as the single micromirror with SW electrodes developed in Chapter 3. The micromirror plate is ground electrically, and V_1, V_2, V_3 and V_4 are applied on four sidewall electrodes, respectively. Each micromirror can be controlled separately. The process of 4×4 micromirror array is developed in terms of that of 2×2 micromirror array. The process includes: i) 4×4 micromirror array fabrication; ii) 4×4 sidewall electrode fabrication; iii) assembly of mirror plate and SW electrodes. The diagrams in Figure 4.11 show 4×4 micromirror array. Figure 4.11 (e) shows one single micromirror with a broken torsion bar. Although the backside features have been designed, they are etched out after a long time DRIE due to the large open cavity on the backside of the mirror plate array. The thickness of the micromirror is 12 μm without backside features after the entire fabrication process.



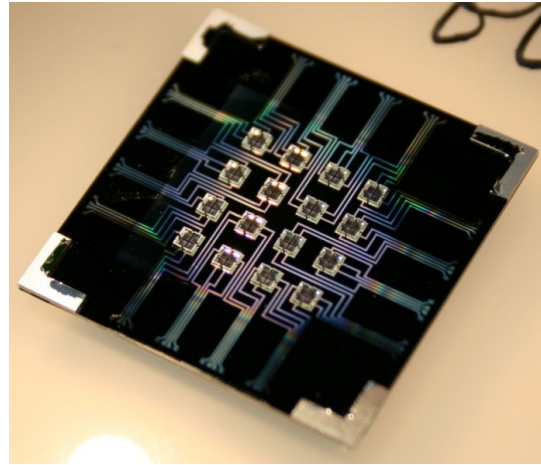
(a)



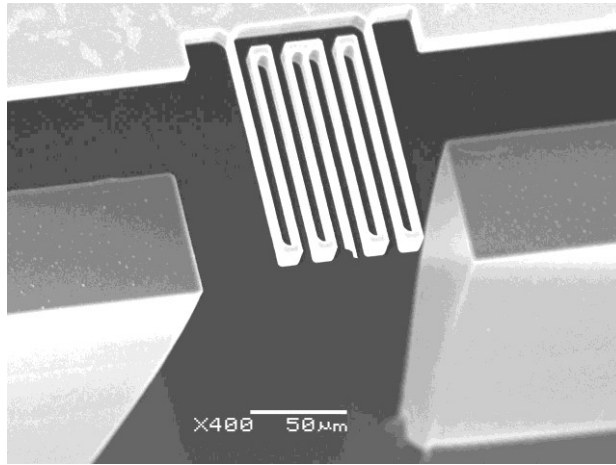
(b)



(c)



(d)



(e)

Figure 4.11: (a) Assembly of 4×4 micromirror array and SW electrodes; (b) SEM of 4×4 micromirror array; (c) SEM of SW electrode array; (d) 4×4 SW electrodes after shadow mask lift-off; (e) SEM of single micromirror with a broken serpentine torsion bar.

4.5 Optimization of Design and Fabrication

The fabrication process of micromirror arrays is more complicated than that of the single micromirror with SW electrodes. It is a continuous and repeated procedure to optimize the structure design and the process flow. Several aspects have to be considered. First of all, Bosch DRIE etch rate is effected by the following: i) aspect ratio of each feature; ii) density of features in one die; iii) open area in one die; iv) position of one die on the entire wafer. When adopting DRIE etching process, the distribution of

DRIE etch rate is faster at three-fourth circle than at the center and the edge of the entire wafer. Secondly, the structure design has to be optimized in terms of the distribution of DRIE etch rate on the entire wafer. The dimensions of torsion bars, gimbal frame, and trench not only satisfy mechanical requirements, but also coincide with the DRIE etch rate. Some sacrificial structures are required in order to fabricate sophisticated features. Thirdly, assembly of the mirror plate array and SW electrodes is a challenge. The special alignment mark and transparent alignment tools are important and can be optimized in the future.

The micromirror array with SW electrodes has a low fill factor. It is possible to improve if the micromirror plate with a pedestal is mounted on top of the micromirror array with SW electrode. The following provides a possible process flow: i) fabricating the micromirror plate array with pedestal on SOI wafer I; ii) fabricating the micromirror array with serpentine torsion bars on SOI wafer II, as shown in Figure 4.2 (a) to (e); iii) flip-chip bonding the wafer I that includes the micromirror plate array on top of the wafer II that have serpentine torsion bars and mirror features; iv) removing the handle layer from the wafer I; v) keeping on following the process in Figure 4.2 (f) to (j'); vi) evaporate Cr/Au on the top layer as a reflective surface. The SW electrode actuator utilizes the same process flow as in section 4.3.2. And then, the micromirror array plate and SW electrodes are assembled through alignment tools.

Chapter 5

MEMS Mirror with SW Electrodes applied for Confocal MACROscope Imaging

5.1 Introduction

The first confocal microscope was invented and built with a stage movement in 1961, when Dr. Markvin Minsky presented the principle of the confocal microscopy [122]. A confocal microscope has one major advantage over a traditional microscope. It allows the focus plane light to pass through a pinhole on the conjugate (or ‘confocal’) plane to the detector while blocking light emitted from out-of-focus planes. As a result, the image resolution and contrast are improved significantly. A confocal microscope images a sample by scanning a diffraction limited spot across the sample either by translating the sample under a fixed beam with an XYZ-stage [122, 123], or by using a system with mirrors scanning the beam on the stationary sample [67]. In comparison to stage scanning, the mirror scanning system is not limited by the scanning speed for acquiring images *in vivo*, therefore, it is well suited for a wide range of applications. The confocal microscope is broadly applied to biological and clinic imaging, as well as semiconductor inspection. The other two types of confocal microscopes are two-photon or multi-photon confocal microscopes and Nipkow disk confocal microscopes [67]. A two-photon confocal microscope images a sample, through an intense near-infrared (IR) laser, by exciting the fluorophore to emit a fluorescence photon with a half wavelength of the laser beam in the focused spot [124-126]. The fluorescence emission is collected by an efficient photodetector without

a use of a pinhole or aperture as the excitation spot is being scanned. Nipkow disk confocal microscopes obtain the scanning beam by spinning a Nipkow disk with regular patterned pinholes. Current scanning methods such as galvanometer, spinning polygon, and acousto-optic scanners are typically used into the confocal microscopes and can introduce vibrations into the system which degrades image quality. Recently, MEMS mirrors have been successfully integrated with traditional confocal microscopes and two-photon confocal microscopes [10, 124-126]. For example, Olympus LEXT OLS3100 confocal microscope is integrated with a 1-D MEMS mirror mounted on a 1-D galvo-scanner [10, 127, 128], and handheld confocal microscopes for skin cancer inspection utilizes MEMS mirrors or microlens [64, 129-137].

The Confocal Laser Scanning MACROscope (CLSM) system (by BPI, Waterloo, Ontario) is a confocal microscope with a large field of view (FOV) for biological analysis. It can obtain very large images with high resolution with a galvo-scanner and a XYZ stage movement. Figure 5.1 shows the schematic of the MACROscope system. The intention is to integrate the MEMS mirror with SW electrodes to a MACROscope system for biomedical imaging [138]. Point-scanning instruments like the MACROscope or confocal microscopes could benefit from the small size and unique features of the MEMS mirror. The galvo-scanner currently used in the MACROscope system consists of a scanning mirror that is actuated by a servo motor. This scanner is large (50 mm x 35 mm) and is capable of scanning at a maximum rate of 40 Hz over +/- 6 degrees (optical) using a closed-loop position feedback system. A very sturdy frame is required to minimize vibrations produced by the large amount of inertia when running at maximum frequency. Using a micromirror instead of the galvo-scanner, it would be possible to simplify the frame structure and decrease the size and weight of the system. An additional advantage is the potential to scan at frequencies much greater than 40 Hz, as well as being able to scan in two directions simultaneously. A MEMS mirror with SW electrodes is used to replace the galvo-scanner for obtaining biomedical imaging.

This chapter presents a MEMS mirror with SW electrodes applied into the MACROscope for biomedical imaging. In comparison to the galvo-scanner, the micromirror plate has a small optical aperture, thus the original optical system requires to be adjusted. This section focuses on developing

the critical optical requirements and optimizing micromirror frequency in a confocal laser scanning imaging system. Two laser scanning optical systems were prototyped and tested. The optimized frequency range based on the MACROscope was investigated. An open-loop control method was adopted to control the MEMS mirror in the system. Finally, a new Micromirror-based Laser Scanning Microscope system was developed with imaging acquisition/processing system based on Programmable Interface Controller (PIC) allowed 2D images to be acquired and displayed.

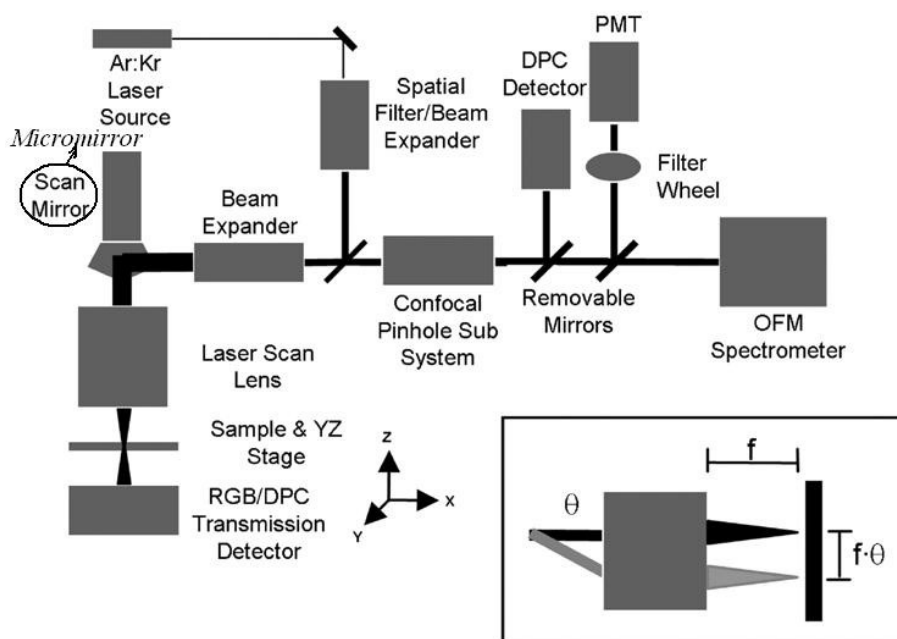


Figure 5.1: Schematic of MACROscope system with a galvo-scanner (the micromirror instead of the galvo-scanner) [138]. DPC Detector, OFM Spectrometer, and PMT were removed from the MACROscope system during experiments.

5.2 Confocal MACROscope Prototype with MEMS Mirrors

5.2.1 Two Optical Systems for Confocal MACROscope with MEMS Mirrors

In the CLSM system, the micromirror with SW electrodes replaces the original 1-D galvo-scanner. Initially, two prototypes of the CLSM are developed to study the critical optical requirements for a

MEMS mirror implementation into the CLSM. Figure 5.2 and 5.3 show block diagrams of the two optical layouts of the micromirror. The confocal detection path has been excluded from the optical arrangement. The CLSM uses a collimated beam of light that is incident onto a galvanometric scanning mirror that is located at the entrance pupil of the laser scan lens. In Optical System-I, a MEMS mirror, as shown in Figure 5.4, is fixed in front of a 4× Beam Expander (BE). The laser beam was expanded to fill the entrance pupil of the objective lens, namely, the conjugate image of the MEMS mirror through the 4-time BE simultaneously images onto the entrance pupil. The BE expands a small aperture (1mm×1mm) to a larger aperture (4mm×4mm), thus, the numerical aperture (NA) of the objective lens will be efficiently utilized by the optical system. Optical System-II takes advantage of a unitary telescope and the MEMS mirror is placed very close to the entrance pupil of the objective lens, as shown in Figure 5.3. The MEMS mirror scans the laser beam which is collimated by the unitary telescope onto the objective lens. Although Optical System-I expands 4-time aperture for the micromirror, the scanning range is reduced to one quarter in comparison to that of Optical System-II.

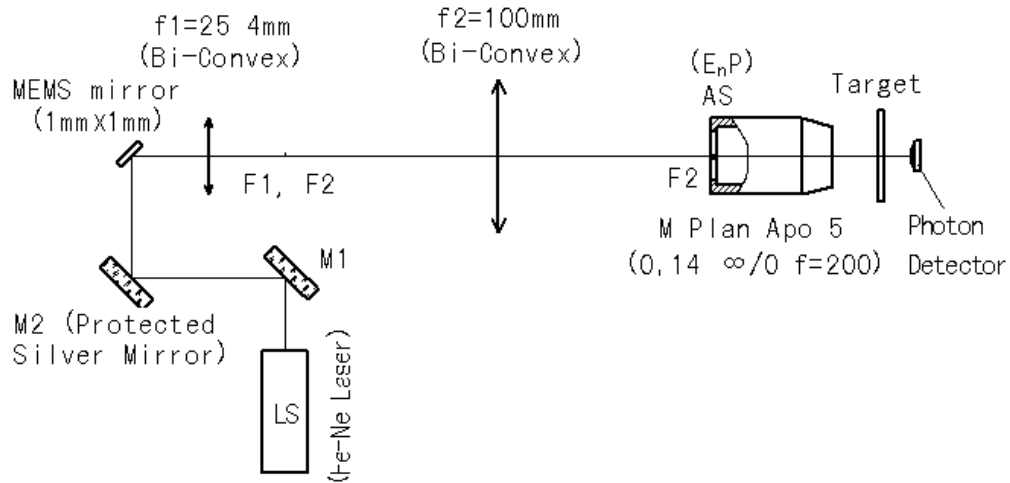
According to Rayleigh criterion for calculating resolution, the maximum number of resolvable spots, N is given by [137, 139],

$$N \cong \frac{\theta_{\max}}{\delta\theta} \cong \frac{\theta_{\max} D}{\lambda} \quad (5.1)$$

where θ_{\max} is the total optical scan range and $\delta\theta$ is the divergence angle, D is the objective lens diameter, and λ is wavelength. The maximum lateral resolution is calculated in terms of the equation,

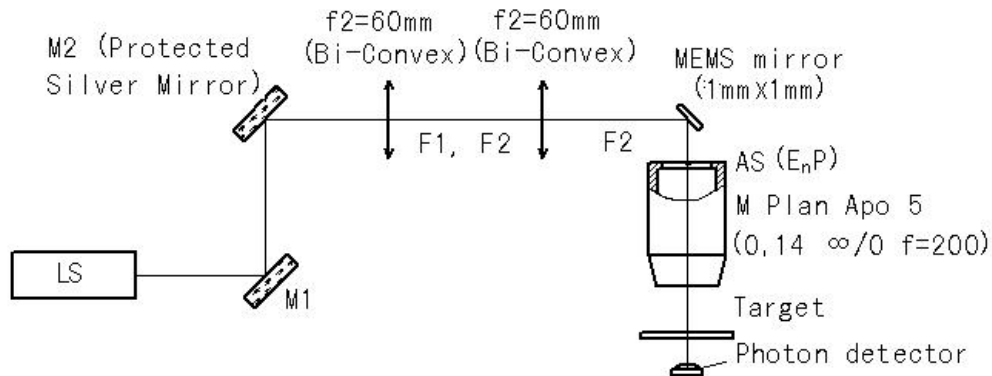
$$d = \frac{1.22 \lambda}{NA} \cong 0.61 \frac{\lambda D}{f} \quad (5.2)$$

where NA is the numerical aperture of the objective lens, and f is the focus length. If the light source is green laser, $\lambda=532\text{nm}$, and the NA of objective lens (M Plan Apo 5) is 0.14, Optical System-I possesses a higher lateral resolution than Optical System-II, as shown in Figure 5.9.



Optical System - I: with 4X Beam Expander

Figure 5.2: Optical System-I: the laser scanning microscope with a 4× beam expander. The micromirror is located at f_1 focus distance, and the entrance pupil of the objective lens at f_2 focus distance. The objective lens is M Plan Apo 5, NA=0.14, $f=200$.



Optical System - II: with unitary telescope

Figure 5.3: Optical System-II: the laser scanning microscope with a unitary telescope. The micromirror is located between Bi-Convex lens, f_2 , and the objective lens (M Plan Apo 5, NA=0.14, $f=200$). The micromirror requires as close as to the entrance pupil.

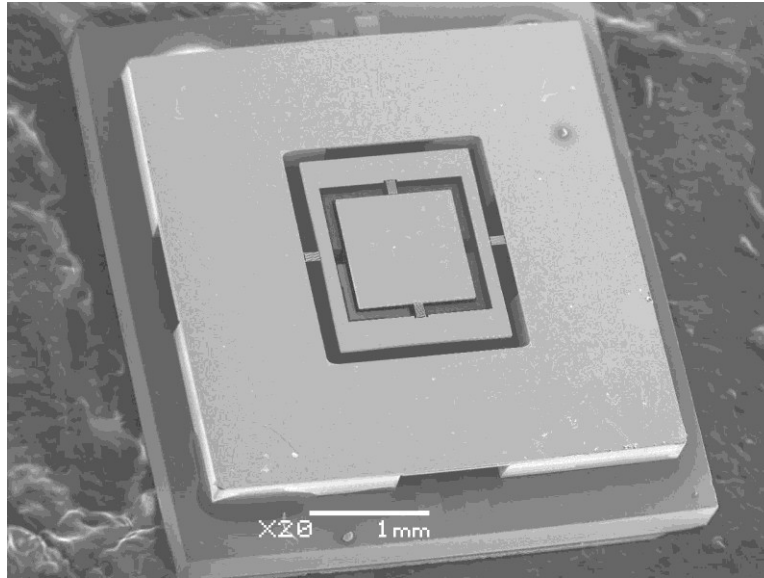
5.2.2 MEMS Mirrors in Confocal MACROscope System

A MEMS mirror with SW electrodes replaces the 1-D galvo-scanner in the MACROscope. The micromirror has been designed and fabricated and its characterization has been obtained in Chapter 3. Figure 5.4 shows two micromirrors with $2\mu\text{m}$ and $3\mu\text{m}$ torsion bars.

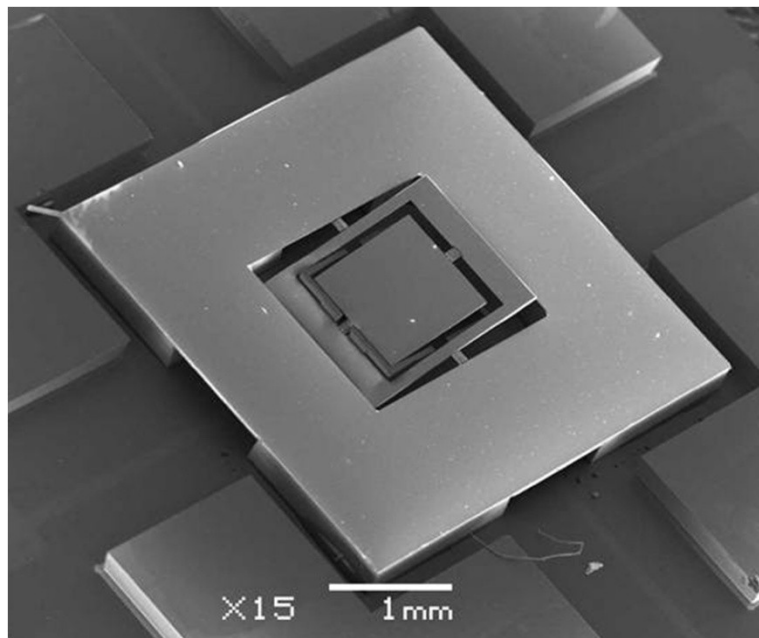
The biaxial MEMS mirror with SW electrodes obtains a flexible scanning pattern by running each axis at different frequency and amplitudes, as shown in Figure 5.8. For the raster scan under DC bias voltage of 40V, AC voltage of 35V, the micromirror with $2\mu\text{m}$ torsion bars can reach $\pm 3^\circ$ (mechanical scan angle) and its resonance frequency is 64Hz on α - scan and 165Hz on β - scan. If the micromirror works under the combination of two frequencies, Lissajous patterns can be achieved.

In terms of the MACROscope system, a modulated triangle waveform with a sinusoidal wave on the corner acts as a control signal to drive the 1-D galvo-scanner. The triangle waveform can extend the linear range for the scanner and maximize the data acquisition time for imaging. Under the closed-loop control, the galvo-scanner performs a one dimensional scan, meanwhile, the XYZ-stage matches the scanning rate with a slow lateral movement to achieve a raster scan. The Z-movement of the XYZ-stage is used to adjust the focus and the depth of field. Through synchronizing the control signal and data acquisition, the rising part of the waveform is utilized for building the image. Using the 2-D micromirror instead of 1-D galvo-scanner and the XYZ-stage simplifies the structure design and it is possible to develop a portable confocal MACROscope system. Moreover, the open-loop control replaces the closed-loop feedback control when the biaxial micromirror with SW electrodes is actuated by the differential drive method [81, 82].

At present, the biaxial micromirror with SW electrodes realizes 1-D scanning in the MACROscope system, because the control box of the MACROscope only generates one channel signal to control the scanner. In the MACROscope, critical optical requirements based on the dynamic response of the micromirror are obtained. In terms of the experimental results, a Micromirror-based Laser Scanning Microscope System is developed. 2-D images are achieved by a raster scan of the micromirror.



(a)



(b)

Figure 5.4: SEM of the micromirror with SW electrodes. (a) the micromirror with $2\mu\text{m}$ torsion bars; (b) the micromirror with $3\mu\text{m}$ torsion bars.

5.3 Experiments and Imaging

5.3.1 Transient Response of the Micromirror

The transient response of the micromirror reflects the dynamic characteristics and induces the damping ratio. Figure 5.5 illustrates the step response of the micromirror with $2\mu\text{m}$ torsion bars on two directions, respectively. The mirror transient response shows an oscillating behavior. If the micromirror is driven by a triangle waveform, which is additive synthesis by odd harmonics, there are ripples on the response waveform that affect the synchronization between the control signal and data acquisition: therefore, the frequency transient response of the micromirror with SW electrodes is tested in order to find the optimized frequency range.

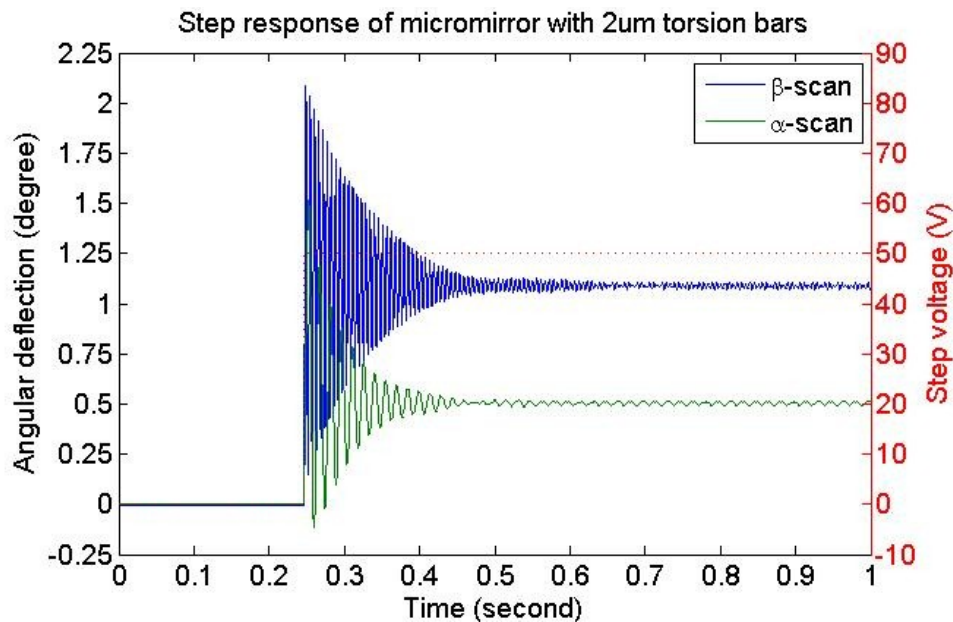


Figure 5.5: The transient response of the micromirror with $2\mu\text{m}$ torsion bars.

5.3.2 Frequency Transient Response of Micromirror under Triangle Waveform

The dynamic response of the micromirror determines the properties of the MACROscope system. In the MACROscope, the control signal is the modulated triangle waveform, and the linear part on the

waveform is the interval of data acquisition. If the sinusoidal waveform drives the micromirror, there is only the phase delay on its dynamic response. However, in order to maximize the linear scanning range, the triangle waveform with rounded corners is adopted as a driving signal, as a result, the dynamic response of the micromirror not only shows a phase delay, but also appears a shape change of the waveform. Figure 5.6 and 5.7 show the frequency transient response of two types of the micromirror with $2\mu\text{m}$ and $3\mu\text{m}$ torsion bars under pure triangle waveform without rounded corners. This waveform only actuates the micromirror on 1D scanning, either α -scan or β -scan. In terms of Figure 5.6 and 5.7, several properties are achieved as the following: i) at the lower frequency, less than resonance frequency, the shape of the waveform is the superposition of driving waveform and harmonic components, and the micromirror experiences extreme overshoots; ii) at the higher frequency, larger than resonance frequency, the scanning waveform is close to the uniform, but has a longer settling time for a good oscillation and also the scanning angle is small; iii) close to the resonance frequency, the scanning waveform has a short settling time and there is a good shape of the waveform, close to the driving triangle waveform. At the frequency response, the beat frequency that is the difference between the driving frequency and the resonance frequency controls the settling time and the waveform. Thus, for the open-loop control, the micromirror actuated by a frequency close to the resonance value has a good behavior and perfect scanning waveform, which is fit for the data acquisition control box and circuits, software in the MACROscope.

Moreover, as shown in Figure 5.6 (b), when the micromirror is driven along β -scan, the oscillation response on α -scan direction is pretty large and the settling time is longer. The reason is that the micromirror with $2\mu\text{m}$ torsion bars on α -scan has a low resonance frequency and easy disturbed by the cross-talk.

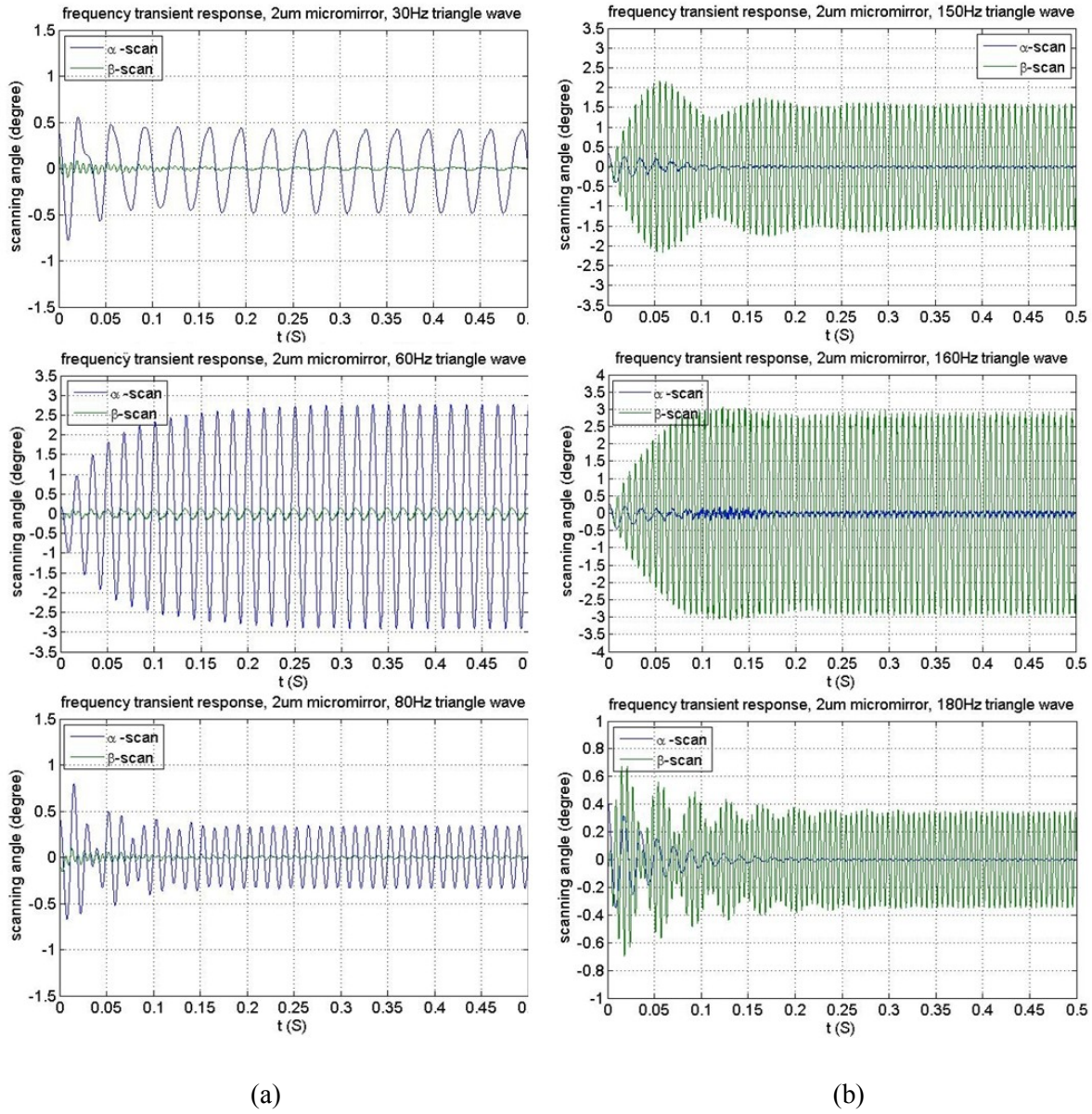
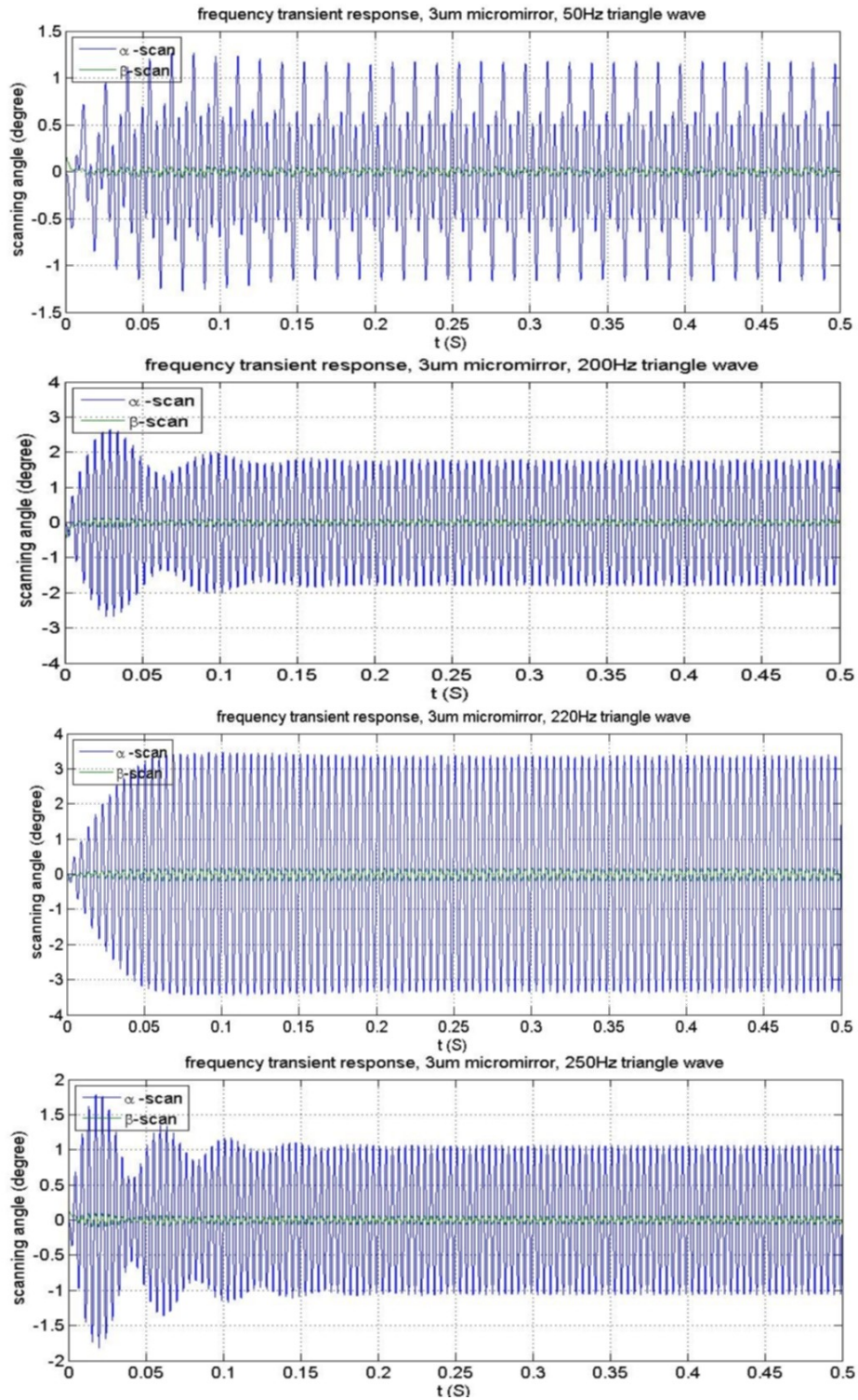
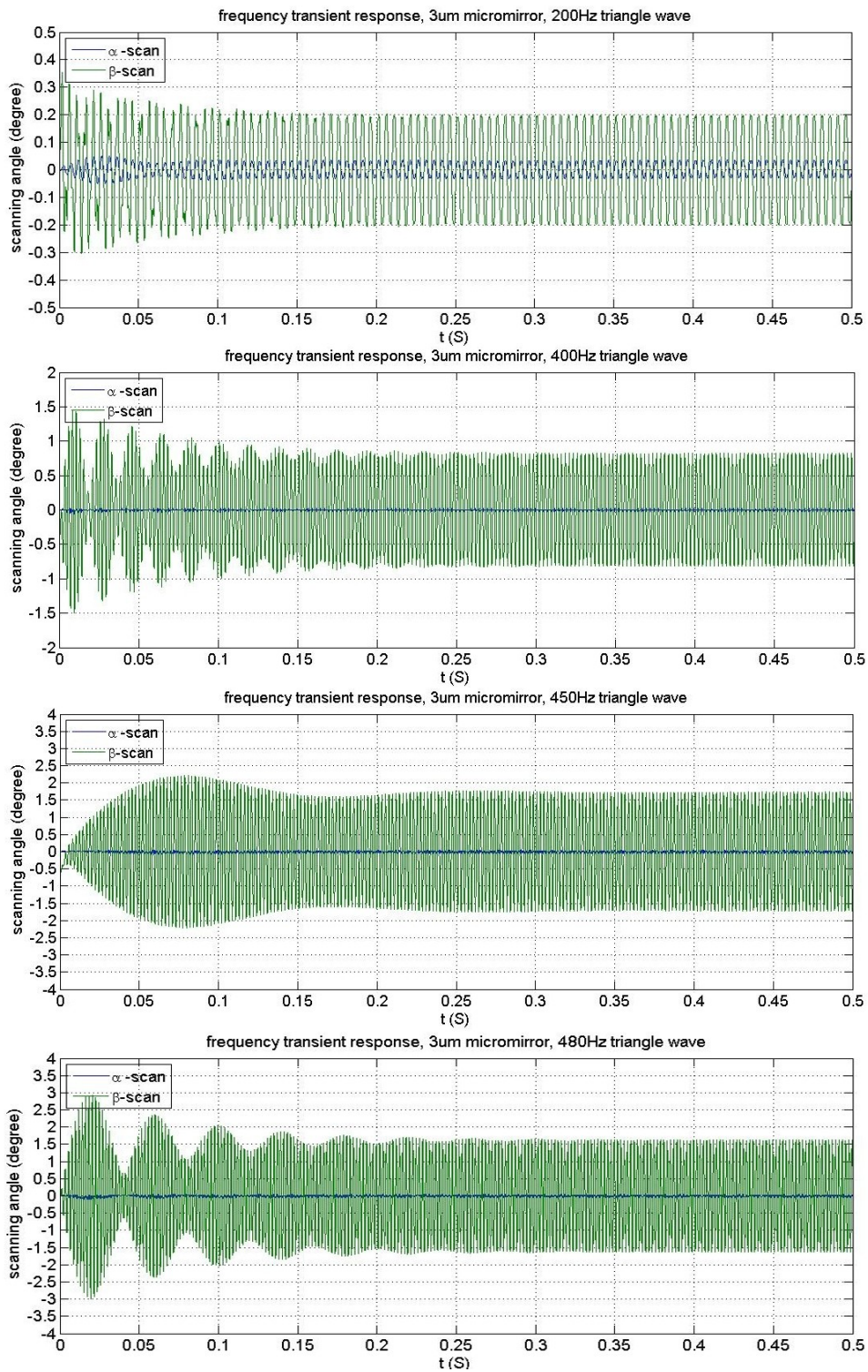


Figure 5.6: The frequency transient response of the micromirror with 2 μ m torsion bars driven by the triangle waveform under $V_{bias}=50V$ and $V_{ac}=2.5V$. The driving signal actuated the micromirror on α - and β -scan, respectively. (a) The frequency response of the micromirror actuated by 30Hz, 60Hz, and 80Hz on α -scan, respectively. (b) The frequency response of the micromirror actuated by 150Hz, 160Hz, and 180Hz on β -scan, respectively.



(a)



(b)

Figure 5.7: The frequency transient response of the micromirror with $3\mu\text{m}$ torsion bars driven by the triangle waveform. The driving signal actuated the micromirror on α - and β -scan, respectively. (a) The frequency response of the micromirror actuated by 50Hz ($V_{\text{bias}}=55\text{V}$, $V_{\text{ac}}=45\text{V}$), 200Hz ($V_{\text{bias}}=55\text{V}$, $V_{\text{ac}}=30\text{V}$), 220Hz ($V_{\text{bias}}=55\text{V}$, $V_{\text{ac}}=20\text{V}$), and 250Hz ($V_{\text{bias}}=55\text{V}$, $V_{\text{ac}}=30\text{V}$) on α -scan, respectively. (b) The frequency response of the micromirror actuated by 200Hz ($V_{\text{bias}}=55\text{V}$, $V_{\text{ac}}=45\text{V}$), 400Hz ($V_{\text{bias}}=55\text{V}$, $V_{\text{ac}}=45\text{V}$), 450Hz ($V_{\text{bias}}=55\text{V}$, $V_{\text{ac}}=10\text{V}$), and 480Hz ($V_{\text{bias}}=55\text{V}$, $V_{\text{ac}}=45\text{V}$) on β -scan, respectively.

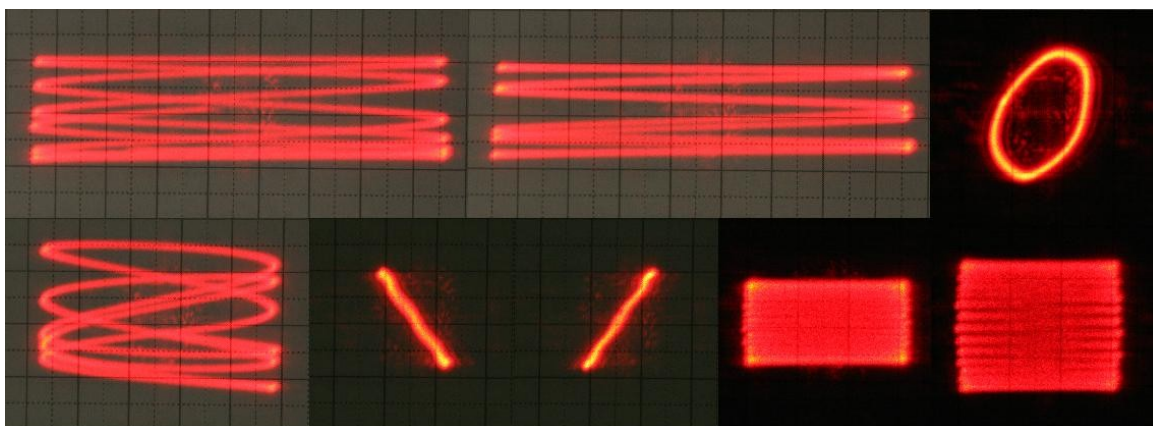


Figure 5.8: The pattern scanning from the micromirror with SW electrodes with $2\mu\text{m}$ torsion bars. Examples of scan pattern for various combinations of amplitude and frequency [83].

In Figure 5.6 and 5.7, the micromirror has a coupling characteristic, namely, if only considered the 1D scanning, the orthogonal direction is affected because of the coupling between α -scan and β -scan[81]. At the small scanning angle, the coupling phenomena are not prominent, but at the large scanning angle, when the micromirror runs on the resonance frequency, the orthogonal direction scanning will oscillate in a small range. In terms of images from the MACROscope with 1-D scanning of the micromirror with $2\mu\text{m}$ torsion bars at 40Hz and 58Hz, as shown in Figure 5.10, the scanning angular deflection of the micromirror at 40Hz is more uniform than that of the micromirror at 58Hz, that is, the image based on 40Hz achieves more better synchronization than that on 58Hz. The 58Hz is close to the resonance frequency of the micromirror on α -scan, as a result, it causes the large coupling effect on β -scan. The repeatability of the micromirror has a little shift, therefore there

exist small ripples on the 20 μ m line image. While at lower scanning frequency, 40Hz, the ripples are not distinct and the 20 μ m line is clearer. The reason is that: when the deflection at one direction scanning under resonance frequency is large, its orthogonal coupling vibration affects the synchronization between the micromirror and control signals.

5.3.3 Images of the MACROscope with MEMS Mirrors

The MACROscope with the MEMS mirror is used to image 5, 10, 20, 50, and 100 μ m grate patterns. The experiment is divided into two phases: i) synchronization test for the micromirror under open-loop control; ii) 2-D image acquisition. The imaging software of the MACROscope synchronizes the galvo-scanner and XYZ-stage assembly with the output signal that is generated by the photo detector in order to display a meaningful real-time image. Its control box generates the signal to drive the galvo-scanner and the XYZ-stage. In the synchronization test phase, the micromirror scans one direction, α -scan, and the XYZ-stage is isolated so as to spatially correlate the data received from the imaging sensor to reflect the repeatability of the micromirror. The optical system of the MACROscope is based on Optical System-I. Meanwhile, to gauge the resolution power, standardized grate patterns with spacing 5, 10, 20, 50, and 100 μ m were scanned. The quality of the image proves to be acceptable when sample patterns are at least 20 μ m apart. Figure 5.10 shows 20 μ m grate pattern images.

For 2-D image acquisition, the MACROscope based on Optical System-II controls the micromirror to scan one direction and moves the XYZ-stage on an orthogonal direction (along with Y-axis). Figure 5.11 shows two images of 20 μ m grate pattern.

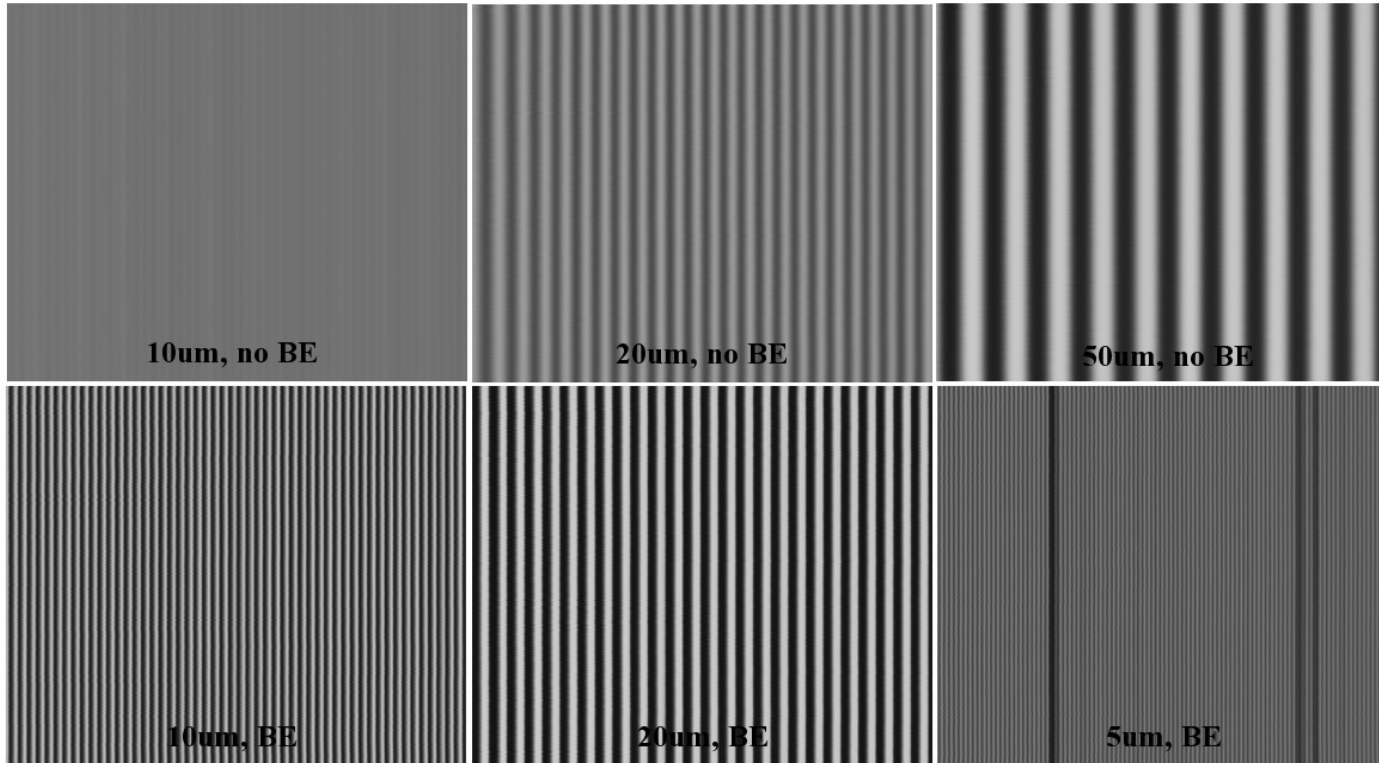


Figure 5.9: The images in terms of the galvo-scanner without XYZ-stage movement. Two optical systems: without Beam Expander and with 4×Beam Expander. The grating patterns are 5, 10, 20, and 50µm. The galvo-scanner works at 40Hz. (Green laser source: $\lambda=532\text{nm}$, the objective lens: M Plan Apo 5, NA=0.14, $f=200$.)

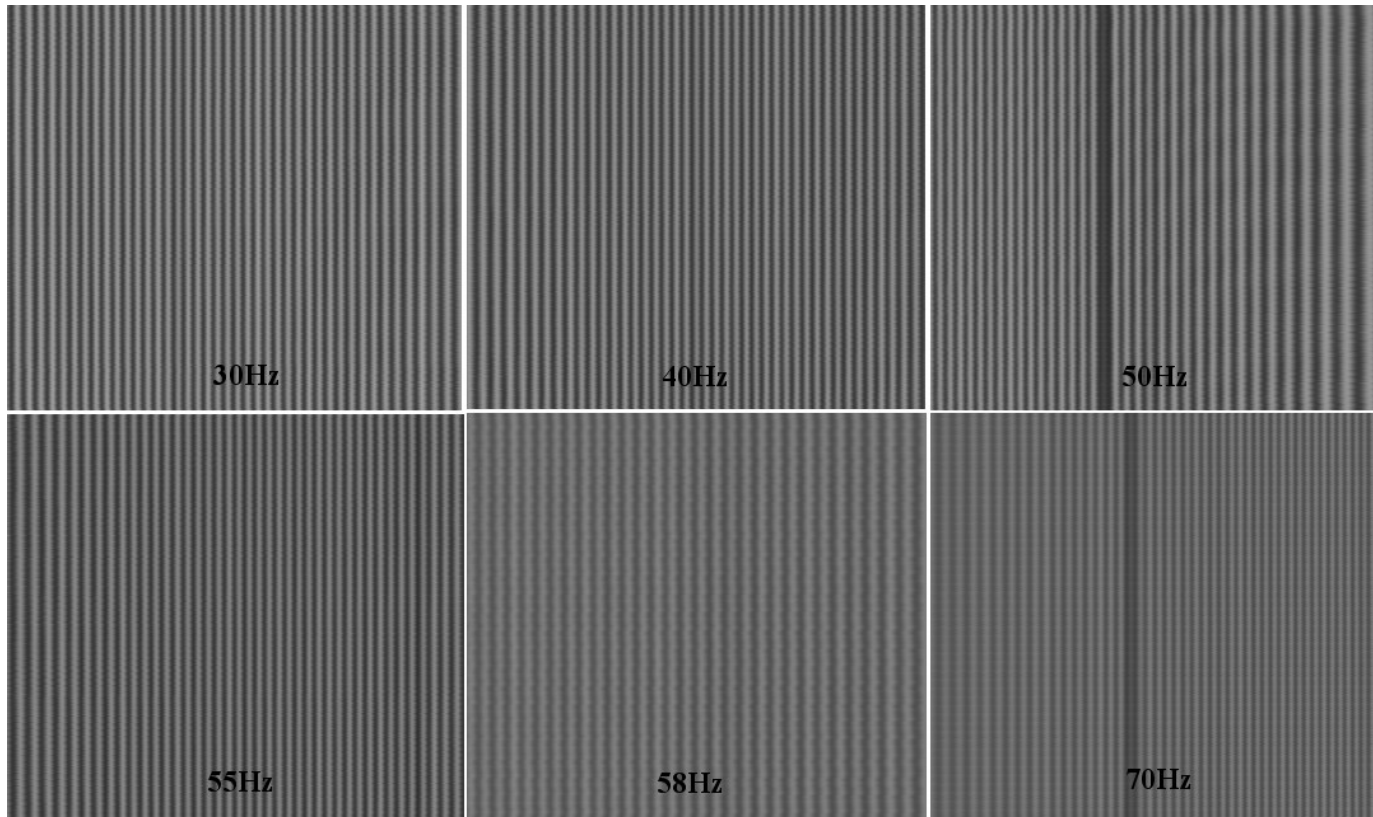


Figure 5.10: The 1-D scanning images in terms of the micromirror with $2\mu\text{m}$ torsion bars. The optical system includes a $4\times$ beam expander with He-Ne laser source ($\lambda=633\text{nm}$), the objective lens: M Plan Apo 5, $\text{NA}=0.14$, $f=200$. The sample is $20\mu\text{m}$ metal lines. The micromirror only scans the 1-D scanning, at α -scan, without the stage movement in order to test synchronization under open-loop control. The frequency ranges from 30Hz to 70Hz.

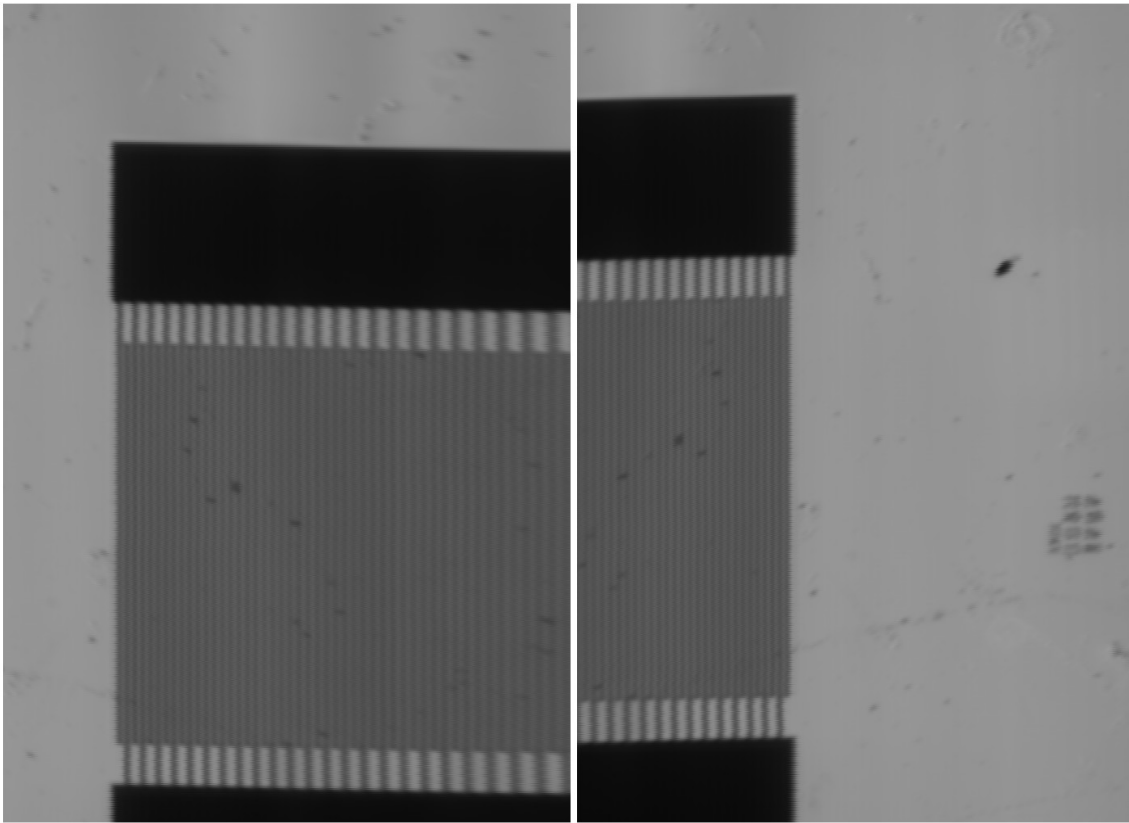


Figure 5.11: 2-D images display $20\mu\text{m}$ metal grating pattern. The micromirror with $2\mu\text{m}$ torsion bars is adopted in the optical system with unitary telescope (Optical System-II). The objective lens is f-theta lens, $\text{NA}=0.14$, $f=200\text{mm}$. The light source is green laser, $\lambda=532\text{nm}$. The frequency of the control signal is 40Hz .

5.3.4 Laser Scanning Microscope System with Micromirror and PIC

A micromirror-based laser scanning microscope system was developed. This system consists of a He-Ne laser source, mirrors, a MEMS mirror with $2\mu\text{m}$ torsion bars, $4\times$ beam expander, beam splitter (BS), objective lens (M pro 2.5, $\text{NA}=0.14$, $f=100$), photodetector and PSD, as shown in Figure 5.12. The imaging process system adopted by this microscope is programmed using Microchip's PIC32MX. The micromirror is actuated to make the laser beam achieve 2-D scan on the grating patterns. The PSD records the corresponding x-y coordinate pair of the laser beam passing through the photodetector and

instantaneously displays the light intensity on the LCD. This approach is referred to as the position-based synchronization method for tracking outputs of the micromirror scan.

The control signal driving the micromirror is a triangle waveform with rounded corners. The control signal is similar to that of the MACROscope. It helps to reduce overshoots of the micromirror due to the discontinuities at the peaks of triangle waves. The amount of time it takes to finish one scan is approximately 200seconds, which is the X-direction of α -scan frequency at 5mHz and the Y-direction scanning at 1Hz due to the slow ADC limitation by the PIC. But this is not the limiting factor of the scanning rate. If a high quality ADC chip were adopted, the data acquisition rate could be increased and the scanning rate might be higher. Figure 5.13 shows the output images on LCD. The sample pattern is at least 50 micrometers in terms of this system. If different objective lens with high numerical aperture were adopted, this system could achieve the sample images with higher resolution.

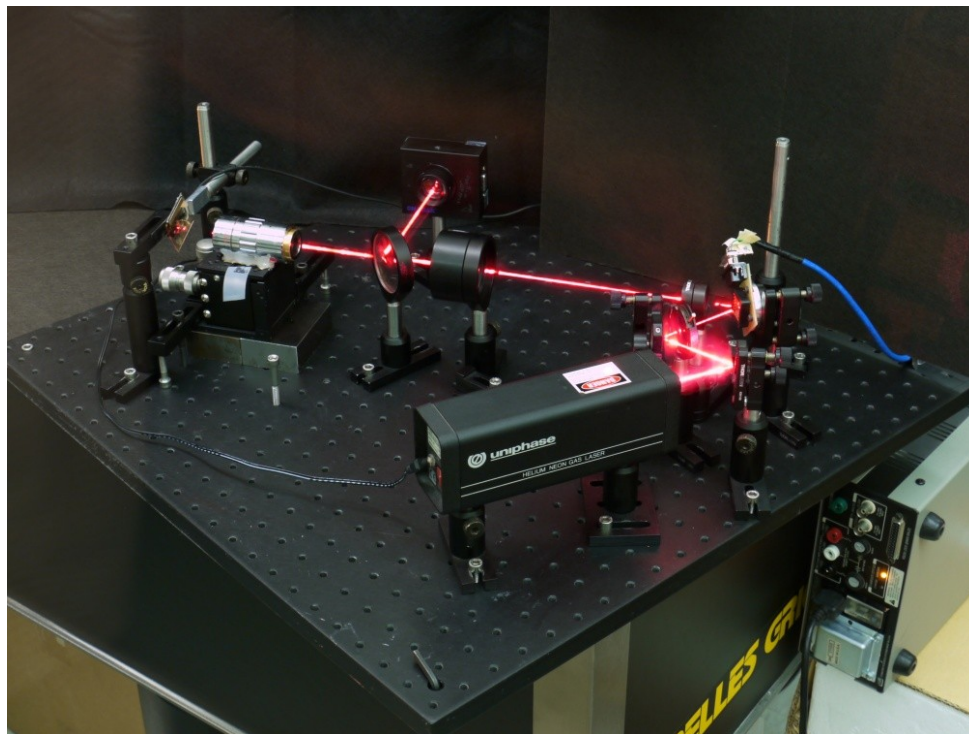
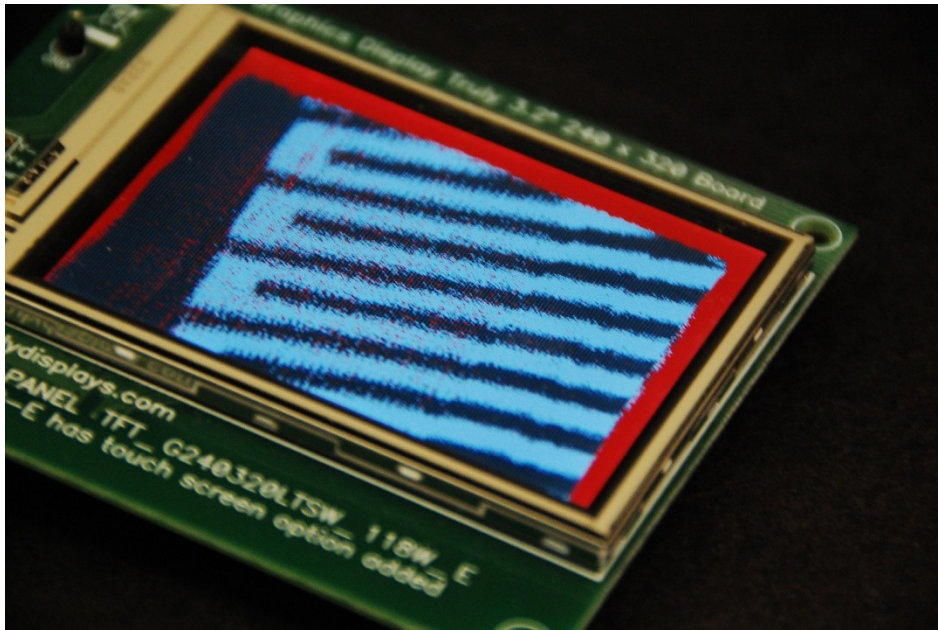
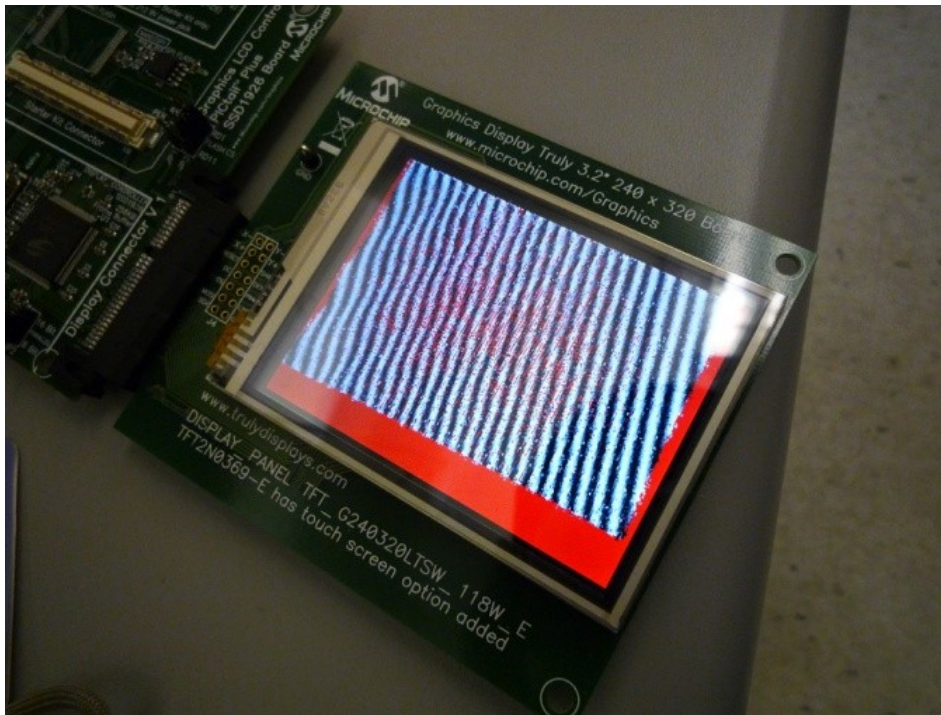


Figure 5.12: The laser scanning microscope system with a MEMS micromirror with $2\mu\text{m}$ torsion bars.



(a)



(b)

Figure 5.13: The grating pattern images from LSMS on PIC LCD. The frame size is 240×320 pixels.

5.4 Conclusion

This chapter presents the micromirror with SW electrodes applied into the MACROscope for imaging. In terms of two optical system configurations, Optical System-I provides higher resolution than Optical System-II due to the beam expander enlarging the beam and increasing the effective numerical aperture. Although the micromirror is actuated under the open-loop control, it could provide acceptable dynamic response at optimized frequency so as to satisfy the synchronization requirement for the system. Moreover, a novel laser scanning microscope system with the micromirror is developed and obtains 2D images. The resolution power for the system is rated at $50\mu\text{m}$ and the image acquisition time is too slow, however, it might be improved by changing objective lens with high NA and using high quality ADC chip on the control circuit.

In this chapter, only the illumination path is shown in Confocal MACROscope system due to simplify the testing process. In order to achieve a real confocal microscope, the system needs to have the following features and changes:

- addition of pin holes after the micromirror such that the reflective or emitted light can be acquired by the sensor,
- reposition of the light sensor-photon multiplier tube (PMT) for the weak signal detection,
- optimization of micromirror scanning range, spacial resolution, and pixels.

Chapter 6

Conclusions and Future Research

6.1 Summary and Conclusions

The work presented in this thesis addresses two major challenges during developing the MEMS mirror: i) the analytical modeling of SW electrodes and 3-end serpentine torsion bars and ii) the novel fabrication process developed in terms of the design of a biaxial micromirror with SW electrodes. Moreover, the development of Micromirror-based MACROscope and the prototype of a Micromirror-based Laser Scanning Microscope provide a system platform for studying the micromirror performance in optical applications.

The SW electrode actuator is a new electrostatic actuator that fills the gap between comb-drive and parallel-plate actuators. There exist two major advantages: obtaining a large angular deflection under a corresponding small drive voltage and possessing a simple fabrication process same as that of parallel-plate actuators. The analytical modeling of SW electrodes and 3-end serpentine torsion bars simulates the static and dynamic characteristics of the biaxial MEMS mirror with SW electrodes very well at small scanning angles. This can be used as a very good reference during the design phases before a commitment to a fabrication runs. Chapter 2 devotes to build the analytical modeling of SW electrodes. In Chapter 3, this analytical modeling is improved in terms of practical design of the MEMS mirror with SW electrodes. The developed analytical modeling is less consuming time than commercial FEM/BEM simulations.

The fabrication process of the biaxial MEMS mirror with SW electrodes is based on SOI wafer, hybrid bulk/surface micromachined technologies and a high-aspect-ratio shadow mask. In order to obtain a large scanning angle, the gap between the micromirror plate and the bottom electrodes is around 300 μm . The height of the SW electrodes is 250 μm . The material of serpentine torsion bars is based on single crystal silicon. Built on a SOI wafer, the thickness of torsion bars is 12 μm accurately. The fabrication process consists of three phases: mirror plate fabrication, SW electrode fabrication and assembly of mirror plate and SW electrodes. The mirror plate fabrication includes front-side fabrication and back-side fabrication on the SOI wafer. The expected thickness of the mirror plate can be achieved. The SW electrode fabrication comprises bulk SW electrodes fabricated on a SOI wafer and a high-aspect-ratio shadow mask. The shadow mask is built on a SCS wafer with the thickness of 250 μm or 285 μm , which patterns bottom electrodes, pads, and wires on the bulk SW electrodes. Those shadow masks can be recycled and used repeatedly. A transparent alignment tool was fabricated and used to assemble the mirror plate and the SW electrodes. The single micromirror fabrication is founded in Chapter 3 and the micromirror array fabrication in Chapter 4. Although the fabrication of micromirror arrays resembles that of the single micromirror, plenty of optimization on mirror array structure design and fabrication parameters is required. Several types of the micromirror with SW electrodes are obtained: single biaxial MEMS mirrors with 3 μm , 2 μm and 1.5 μm 3-end serpentine torsion bars, single biaxial MEMS mirrors with 2-end serpentine torsion bars, and 2 \times 2 and 4 \times 4 micromirror arrays.

In Chapter 5 the performance of a biaxial MEMS mirror with SW electrodes in the MACROscope was studied. The MACROscope system from BPI adopts a galvo-scanner and XYZ-stage to acquire laser beam scanning and gain high resolution images with a large FOV. The biaxial MEMS mirror replaces the galvo-scanner to simplify the design of the MACROscope. In terms of two optical configurations tested in the MACROscope, optical requirements of the system based on a biaxial MEMS mirror are studied. On the other hand, frequency optimization of the MEMS mirror is achieved in terms of the MACROscope control requirements. Meanwhile, a Micromirror-based Laser Scanning Microscope system is built and obtains 2-D images.

6.2 Future Works

This thesis presents the design, fabrication, and characterization of a 2-D SOI MEMS micromirror with SW electrodes for Confocal MACROscope imaging. The single biaxial MEMS mirror with SW electrodes, 2×2 and 4×4 micromirror arrays are obtained in terms of hybrid bulk/surface micromachined technologies. The improvement of Confocal MACROscope integrated with a biaxial micromirror and the prototype of Micromirror-based Laser Scanning Microscope are obtained. For the future direction, they include several works:

i) Improvement on the analytical modeling of SW electrodes at large angular deflection: In this range, the nonlinear property of 3-end serpentine torsion bars and fringe field effects on the electrostatic field need to be understood. Meanwhile, when the MEMS mirror with SW electrodes reaches a large angular deflection, either on α -scan around $\pm 10^\circ$ (mechanical angle), an oscillation phenomenon can be observed. This requires an explanation based on the improved modeling.

ii) Accomplishment on the confocal path of the MACROscope system: Although optical requirements and optimized frequency for the MEMS mirror based on the illumination path of the MACROscope has been obtained, there exists a distance to build a real confocal microscope. In order to build a Micromirror-based Confocal MACROscope, the confocal path is required by adding an optical fiber as a pinhole in the optical system. The relative adjustments and tests have to be implemented.

iii) Develop an endoscopic probe with MEMS mirrors and implement the endoscope with OCT or confocal microscope.

iv) Study control methods for driving micromirror arrays. Apply 2×2 and 4×4 micromirror arrays into confocal microscope to increase effective optical aperture and obtain higher resolution images

Bibliography

- [1] M. J. Madou, *Fundamentals of Microfabrication*, Boca Raton, Fla.: CRC Press c1997
- [2] D. A. Horsley, W. O. Davis, K. J. Hogan, M. R. Hart, E. C. Ying, M. Chaparala, B. Behin, M. J. Daneman, and M.-H. Kiang, "Optical and mechanical performance of a novel magnetically actuated MEMS-based optical switch," *J. Microelectromech. Syst.*, vol.14, no.2, pp.274-84, 2005
- [3] I. W. Jung, Y. A. Peter, E. Carr, J. S. Wang, and O. Solgaard, "Single-crystal-silicon continuous membrane deformable mirror array for adaptive optics in space-based telescopes," *IEEE J. Sel. Topics Quantum Electron.*, vol. 13, no. 2, pp.162-167, 2007
- [4] S. J. Kim, Y. H. Cho, H. J. Nam and J. U. Bu, "Piezoelectrically pushed rotational micromirrors using detached PZT actuators for wide-angle optical switch applications," *J. Micromech. Microeng.*, vol.18, pp.125022 (7pp), 2008
- [5] A. D. Yalcinkaya, O. Ergeneman, H. Urey, "Polymer magnetic scanners for bar code applications," *Sens. Actuators A, Phys.*, vol.135, pp.236-43, 2007
- [6] A. D. Yalcinkaya, H. Urey, D. Brown, T. Montague, and R. Sprague, "Two-axis electromagnetic microscanner for high resolution displays," *J. Microelectromech. Syst.*, vol.15, no.4, pp.786-94, 2006
- [7] H. Xie, Y. Pan, G. K. Fedder, "Endoscopic optical coherence tomographic imaging with a CMOS-MEMS micromirror," *Sens. Actuators A, Phys.*, vol.103, pp.237-241, 2003

- [8] J.T.W.Yeow, V.X.D.Yang, etc, A. Chahwan, M.L. Gordon, B. Qi, I.A.Vitkin, B.C. Wilson, and A.A. Goldenberg, "Micromachined 2-D scanner 3-D optical coherence tomography," *Sens. Actuators A, Phys.*, vol.117, no.2, pp.331-340, 2005
- [9] J.H. Lee, Y. C. Ko, D. H. Kong, J. M. Kim, K. B. Lee, and D. Y. Jeon, "Design and fabrication of scanning mirror for laser display," *Sens. Actuators A, Phys.*, vol.96, pp.223-230, 2002
- [10] H. Miyajima, N. Asaoka, T. Isokawa, M. Ogata, Y. Aoki, M. Imai, O. Fujimori, M. Katashiro, and K. Matsumoto, "A MEMS electromagnetic optical scanner for a commercial confocal laser scanning microscope," *J. Microelectromech. Syst.*, vol.12, no. 3, pp.243-51, 2003
- [11] N. Maluf, K. Williams, *An introduction to microelectromechanical systems engineering*, 2nd ed, Boston ; London : Artech House c2004
- [12] J. C. Tsai and M. C.Wu, "Gimbal-less MEMS two-axis optical scanner array with high fill-factor," *J. Microelectromech. Syst.*, vol.14, no.6, pp.1323-1328, 2005
- [13] L. J. Hornbeck, "Deformable-mirror spatial light modulators," in *Proc. SPIE Critical Reviews Series 1150 Spatial Light Modulators and Applications III*, pp.86-102. 1989
- [14] L. J. Hornbeck, "Current status of the digital micromirror device (DMD) for projection television applications," *IEDM 93, IEEE 1993*, pp.381-384, 1993
- [15] H. Toshiyoshi, W. Piyawattanametha, C. T. Chan, and M. C. Wu, "Linearization of electrostatically actuated surface micromachined 2-D optical scanner," *J. Microelectromech. Syst.* vol.10, no.2, pp.205-214, 2001
- [16] K. Cao, W. Liu, and J. J. Talghader, "Curvature compensation in micromirrors with high-reflectivity optical coatings," *J. Microelectromech. Syst.*, vol.10, no.3, pp.409-417, 2001
- [17] Y. H. Min and Y. K. Kim, "Modeling, design, fabrication and measurement of a single layer polysilicon micromirror with initial curvature compensation," *Sens. Actuators A, Phys.*, vol.78, pp.8-17, 1999

- [18] C. H. Tien, and C. H. Lee, "Optical properties of surface micromachining with randomly distributed etch holes," *Jpn. J. Appl. Phys.*, vol.45,no2A, pp.1015-1017, 2006
- [19] J. Zou, M. Balberg, C. Byrne, C. Liu, and D. J. Brady, "Optical properties of surface micromachined mirrors with etch holes," *J. Microelectromech. Syst.*, vol.8, no.4, pp.506-513, 1999
- [20] C. Pu, S. Park, P. B. Chu, S. S. Lee, M. Tsai, D. Peale, N. H. Bonadeo, and I. Brener, "Electrostatic actuation of three-dimensional MEMS mirrors using sidewall electrodes," *IEEE J. Sel. Topics Quantum Electron.*, vol.10, no.3, pp.472-77, 2004
- [21] S. Kwon, V. Milanovic, and L. P. Lee, "Vertical combdrive based 2-D gimbaled micromirrors with large static rotation by backside island isolation," *IEEE J. Sel. Topics Quantum Electron.*, vol.10, no.3, 2004
- [22] V. Milanovic, G. A. Matus, and D. T. McCormick, "Gimbal-less monolithic silicon actuators for tip-tilt-piston micromirror applications," *IEEE J. Sel. Topics Quantum Electron.*, vol. 10, no. 3, pp.462-71, 2004
- [23] T.D.Kudrle, C.C.Wang, M.G..Bancu, J.C.Hsiao,A.Pareek, M.Waelti, G.A.Kirkos, T.Shone, C.D.Fung, C.H.Mastrangelo, "Single-crystal silicon micromirror array with polysilicon flexures", *Sens. Actuators A, Phys.*, vol.119, no. , pp.559-566, 2005
- [24] K. Murakami, "A miniature confocal optical scanning microscope for endoscope," *in Proc. SPIE MOEMS Display and Imaging Systems III*, vol.5721, Bellingham, WA, 2005
- [25] K. Jia, S. Pal, H. Xie, "An electrothermal tip-tilt-piston micromirror based on folded dual S-shaped bimorphs," *J. Microelectromech. Syst.*, vol. 18, no.5, 2009
- [26] J. Singh, J.H.S. Teo, Y. Yu, C.S. Premachandran, N. Chen, R. Kotlanka, M. Olivo and C.J.R. Sheppard, "A two axes scanning SOI MEMS micromirror for endoscopic bioimaging," *J. Micromech. Microeng.*, vol.18, pp.025001(9pp), 2008

- [27] A. Jain, A. Kopa, Y. Pan, G. K. Fedder, and H. Xie, "A two-axis electrothermal micromirror for endoscopic optical coherence tomography," *IEEE J. Sel. Topics Quantum Electron.*, vol. 10, no. 3, pp.636-642, 2004.
- [28] K. E. Petersen, "Silicon as a mechanical material," in *Proc. IEEE*, vol.70, no.5, pp.420-457,1982
- [29] T. Tsutsumino, Y. Suzuki, N. Sakurai, N. Kasagi, and Y. Sakane, "Nano-metal-ink-based electrode embedded in parylene HARS with the aid of the capillary effect," in *Proc. IEEE 20th Int. Conf. MEMS*, Korea, pp.313-16, 2007
- [30] C.H. Ji and Y.K. Kim, "Electromagnetic micromirror array with single-crystal silicon mirror plate and aluminum spring," *J. Lightwave Tech.*, vol.21, no.3, pp.584-90, 2003
- [31] S. K. Lee, M. G. Kim, J. Y. An, M. H. Jun, S. Yang, and J. H. Lee, "Polymeric (SU-8) optical microscanner driven by electrostatic actuation," in *Proc. IEEE 22nd Int. Conf. MEMS*, pp.955-958, 2009
- [32] C.S. Huang, Y.T. Cheng, J. Chung, W. Hsu, "Investigation of Ni-based thermal bimaterial structure for sensor and actuator application," *Sens. Actuators A, Phys.*, vol.149, pp.298-304, 2009
- [33] L. Wu and H. Xie, "124° rotation angle electrothermal micromirror with integrated platinum heater," *IEEE J. Sel. Topics Quantum Electron.*, vol.13, no.2, 2007
- [34] K. Jia, S. R. Samuelson and H. Xie, "Single-wafer solution and optical phased array application of micro-mirror arrays with high fill factor and large sub-apertures," in *Proc. IEEE Int. Conf. 23th MEMS*, Hongkong, pp.180-183, 2010
- [35] I. J. Cho and E. Yoon, "A low-voltage three-axis electromagnetically actuated micromirror for fine alignment among optical devices," *J. Micromech. Microeng.*, vol.19, pp.085007 (8pp), 2009

- [36] S. H. Hung, H. T. Hsieh and G. D. J. Su, "An electro-magnetic micromachined actuator monolithically integrated with a vertical shutter for variable optical attenuation," *J. Micromech. Microeng.*, vol.18, pp.075003(8pp), 2008
- [37] H. M. Jeong, Y. H. Park, Y. C. Cho, J. Hwang, S. M. Chang, S. J. Kang, H. K. Jeong, J. O. Kim, J. H. Lee, "Slow scanning electromagnetic scanner for laser display," *J. Micro/Nanolith. MEMS MOEMS*, vol.7, no.4, pp.043003-13pp, 2008
- [38] H. Miyajima, "Development of a MEMS electromagnetic optical scanner for a commercial laser scanning," *J. Microlith., Microfab., Microsyst.*, vol.3, no.2, pp.348-57, 2004
- [39] S. Schonhardt, J.G. Korvink, J. Mohr, U. Hollenbach and U. Wallrabe, "Magnetic comb drive actuator," in *Proc. IEEE Int. Conf. 23th MEMS*, Hongkong, China, pp.479-80, 2010
- [40] S. O. Isikman, O. Ergeneman, A. D. Yalcinkaya, and H. Urey, "Modeling and characterization of soft magnetic film actuated 2-D scanners," *IEEE J. Sel. Topics Quantum Electron.*, vol.12, no.2, pp.283-89, 2007
- [41] D. A. Horsley, W. O. Davis, K.J. Hogan, M.R. Hart, E. C. Ying, M. Chaparala, B. Behin, M. J. Daneman, and M. H. Kiang, "Optical and mechanical performance of a novel magnetically actuated MEMS-based optical switch," *J. Microelectromech. Syst.*, vol.14, no.2, pp.274-84, 2005
- [42] S. Brugger and O. Paul, "Resonant magnetic microsensor with uT resolution," in *Proc. IEEE Int. Conf. 21st MEMS*, Tucson, AZ, USA, pp.944-947, 2008
- [43] J. J. Bernstein, T. W. Lee, F. J. Rogomentich, M. G. Bancu, K. H. Kim, G. Maguluri, B. E. Bouma, J. F. DeBoer, "Scanning OCT endoscope with 2-axis magnetic micromirror," in *Proc. SPIE Endoscopic Microscopy II*, vol. 6432, pp.64320L, 2007
- [44] K. H. Kim, B. H. Park, G. N. Maguluri, T. W. Lee, F. J. Rogomentich, M. G. Bancu, B. E. Bouma, J. F. de Boer, and J. J. Bernstein, "Two-axis magnetically-driven MEMS scanning

- catheter for endoscopic high-speed optical coherence tomography,” *Opt. Exp.*, vol.15, no.26, pp.18130, 2007
- [45] J. Bernstein, W.P. Taylor, J. Brazzle, G. Kirkos, J. Odhner, A. Pareek, M. Zai, “Two axis-of-rotation mirror array using electromagnetic MEMS,” *IEEE*, pp275-8, 2003
- [46] M. Jamet, et al., “High-curie-temperature ferromagnetism in self-organized $\text{Ge}_{1-x}\text{Mn}_x$ nanocolumns”, *Nature materials*, vol.5, pp.653-659, 2006
- [47] T. Kawabata, M. Ikeda, H. Goto, M. Matsumoto, and Y. Tsuneji, “The 2-Dimensional micro scanner integrated with PZT thin film actuator,” in *Proc. IEEE 1997 Int. Conf. on Solid-State Sensors and Actuators*, pp.339-342. 1997
- [48] J. M. Zara, and S. W. Smith, “A micromachined high frequency ultrasound scanner using photolithographic fabrication,” *IEEE Trans. Ultrason. Ferroelectr. Freq. Control.*, vol.49, no.7, 2002
- [49] K. H. Koh, T. Kobayashi, F. L. Hsiao and C. Lee, “A 2-D MEMS scanning mirror using piezoelectric PZT beam actuators,” *Procedia Chemistry*, vol.1, pp.1303-1306, 2009
- [50] S. J. Kim, Y. H. Cho, H. J. Nam and J. U. Bu, “Piezoelectrically pushed rotational micromirrors using detached PZT actuators for wide-angle optical switch applications,” *J. Micromech. Microeng.*, vol.18, pp.125022 (7pp), 2008
- [51] C. Lee, F. L. Hsiao, T. Kobayashi, K. H. Koh, P. V. Ramana, W. Xiang, B. Yang, C. W. Tan, and D. Pinjala, “A 1-V operated MEMS variable optical attenuator using piezoelectric PZT thin-film actuators,” *IEEE J. Sel. Topics Quantum Electron.*, vol.15, no. 5, 2009
- [52] P. Muralt, “PZT thin films for microsensors and actuators: where do we stand?”, *IEEE Trans. Ultrason. Ferroelectr. Freq. Control.*, vol.47, no.4, pp.903-915, 2000
- [53] H. Zeng, A. D. Feinerman, Z. Wan, and P. R. Patel, “Piston-motion micromirror based on electrowetting of liquid metals,” *J. Microelectromech. Syst.*, vol.14, no.2, pp.285-94, 2005

- [54] J. Lee, H. Moon, J. Fowler, T. Schoellhammer, C. J. Kim, "Electrowetting and electrowetting-on-dielectric for microscale liquid handling," *Sens. Actuators A, Phys.*, vol.95, pp.259-268, 2002
- [55] I. J. Cho and E. Yoon, "Design and fabrication of a single membrane push-pull SPDT RF MEMS switch operated by electromagnetic actuation and electrostatic hold," *J. Micromech. Microeng.*, vol.20, pp.035028(7pp), 2010
- [56] Y. Eun, H. Na, B. Jeong, J. Lee, "Bidirectional electrothermal electromagnetic torsional microactuators for large angular motion at dc mode and high frequency resonance mode operation," *J. Micromech. Microeng.*, vol.19, pp.(8pp), 2009
- [57] Ph. Robert, D. Saias, C. Billard, S. Boret, N. Sillon, C. Maeger-Pachurka, P. L. Charvet, G. Bouche, P. Ancey and P. Berruyer, "Integrated RF-MEMS switch based on a combination of thermal and electrostatic actuation," in *Proc. IEEE 12th Int. Conf. Solid-State Sens., Actuators, Microsyst. Transducers*, Boston, MA, pp.1714-17, 2003
- [58] A. Alwan and N. R. Aluru, "Analysis of hybrid electrothermomechanical microactuators with integrated electrothermal and electrostatic actuation," *J. Microelectromech. Syst.*, vol.18, no.5, pp.1126-36, 2009
- [59] D. Hah, P. R. Patterson, H. D. Nguyen, H. Toshiyoshi, and M. C. Wu, "Theory and experiments of angular vertical comb-drive actuators for scanning micromirrors," *IEEE J. Sel. Topics Quantum Electron.*, vol.10, no.3, pp.505-513, 2004
- [60] D. Hah, S. T.Y. Huang, J. C. Tsai, H. Toshiyoshi, and M. C. Wu, "Low-Voltage, large-scan angle MEMS analog micromirror arrays with hidden vertical comb-drive actuators," *J. Microelectromech. Syst.*, vol.13, no.2, pp.279-289, 2004

- [61] S. Kwon, V. Milanovic, and L. P. Lee, "Vertical combdrive based 2-D gimbaled micromirrors with large static rotation by Backside island isolation", *IEEE J. Sel. Topics Quantum Electron.*, vol.10, no.3, pp.498-504, 2004
- [62] U. Krishnamoorthy, D. Lee, and O. Solgaard, "Self-aligned vertical electrostatic combdrives for micromirror actuation," *J. Microelectromech. Syst.*, vol.12, no.4, pp.458-64, 2003
- [63] H. Xie, Y. Pan, and G. K. Fedder, "A CMOS-MEMS mirror with curled-hinge combdrives," *J. Microelectromech. Syst.* vol.12, no.4, pp.450-457, 2003
- [64] C. Siu, H. Zeng, and M. Chiao, "Magnetically actuated MEMS microlens scanner for in vivo medical imaging", *Opt. Exp.*, Vol.15, No. 18, 11154-11166, Sept. 2007
- [65] Z. Yaqoob, J. Wu, E. J. McDowell, X. Heng, C. Yang, "Methods and application areas of endoscopic optical coherence tomography", *J. Biomed. Opt.*, vol.11, no.6, pp.1-19, 2006
- [66] B. E. Bouma, G. J. Tearney, *Handbook of Optical Coherence Tomography* , NewYork: Marcel Dekker, 2002
- [67] J.B. Pawley, *Handbook of Biological Confocal Microscopy*, 3rd ed., Berlin: Springer.2006
- [68] J. M. Zara, S. Yazdanfar, K. D. Rao, J. A. Izatt, and S. W. Smith, "Electrostatic micromachine scanning mirror for optical coherence tomography", *Opt. Lett.*, vol.28, no.8, 2003
- [69] T Mitsui, Y Takahashi and Y Watanabe, "A 2-axis optical scanner driven nonresonantly by electromagnetic force for OCT imaging", *J. Micromech. Microeng.*, vol.16, pp.2482-2487, 2006
- [70] T. Xie, H. Xie, G.K. Fedder and Y. Pan , "Endoscopic optical coherence tomography with new MEMS mirror", *Electron. Lett.*, vol.39, no.21, 2003
- [71] L. Wu and H. Xie, "A Dual Reflective Electrothermal MEMS Micromirror for Full Circumferential Scanning Endoscopic Imaging", in *Proc. SPIE*, vol. 6885, 688508-1~8, 2008

- [72] L. Fu, A. Jain, C. Cranfield, H. Xie, and M. Gua, “Three-dimensional nonlinear optical endoscopy”, *J. Biomed. Opt.*, vol.12,no.4, 2007
- [73] J. Woonggyu, T. McC. Daniel, Z. Jun, W. Lei, C.T. Norman, Z.P. Chen, “Three-dimensional endoscopic optical coherence tomography by use of a two-axis microelectromechanical scanning mirror”, *Appl. Phys. Lett.*, vol.88, pp.1-3, 2006
- [74] J. Woonggyu, T.M. Daniel, Y.C. Ahn, A. Sepehr, M. Brenner, B. Wong, N.C. Tien, and Z. Chen, “ In vivo three-dimensional spectral domain endoscopic optical coherence tomography using a microelectromechanical system mirror”, *Opt. Lett.*, vol.32, no.22, pp.3239-3241, 2007
- [75] J. M. Zara, C. A. Lingley-Papadopoulos, “Endoscopic OCT approaches toward cancer diagnosis”, *IEEE Journal of selected topics in quantum electronics*, vol.14, no.1, pp.70-81, 2008
- [76] D. Huang, E. A. Swanson, C. P. Lin, J. S. Schuman, W. G. Stinson, W. Chang, M. R. Hee, T. Flotte, K. Gregory, C. A. Puliafito, J. G. Fujimoto, “Optical coherence tomography,” *Science*, vol.254, pp.1178-1181, 1991
- [77] A. F. Fercher, W. Drexler, C. K. Hitzenberger and T. Lasser, “Optical coherence tomography-principles and applications”, *Rep. Prog. Phys.*, vol.66, pp.239-303, 2003
- [78] M. E. Brezinski, *Optical coherence tomography: Principles and Applications*, Boston: Academic Press, c2006
- [79] A. F. Fercher, “Optical coherence tomography,” *J. Biomed. Opt.*, vol. 1, no. 3, pp. 157–173,1996
- [80] V Prasad, D Semwogerere and Eric R Weeks, “Confocal microscopy of colloids”, *J. Phys.: Condens. Matter* 19, pp.1-25, 2007
- [81] Y. H. Bai, J. T. W. Yeow, B. C. Wilson, “A characteristic study of micromirror with sidewall Electrodes,” *Int. J. Optomechatronics*, vol.1, no.3, pp.231-258, 2007

- [82] Y. H. Bai, J. T.W. Yeow, and B. C. Wilson, "Design, fabrication, and characteristics of a MEMS micromirror with sidewall electrodes," *J. Microelectromech. Syst.*, vol.19, no.3, pp.619-631, 2010
- [83] Y. H. Bai, J. T.W. Yeow, P. Constantinou, S. Damaskinos, and B. C.Wilson, "A 2-D micromachined SOI MEMS mirror with sidewall electrodes for biomedical imaging," *IEEE/ASME Trans. Mechatronics*, vol.15, no.4, pp.501-510, 2010
- [84] W. M. Duncan, T. Bartlett, B. Lee, D. Powell, P. Rancuret, and B. Sawyers, "Dynamic optical filtering in DWDM systems using the DMD," *Solid-state Electron.*, vol.46, pp.1583-1585, 2002.
- [85] F. Khechana, H. van Lintel, J. L. Massieu, S. Ackley, and P. Renaud, "Thermally actuated micro scanner for barcode reader applications," in *Proc. IEEE/LEOS Int. Conf. on Optical MEMS and Their Applications*, pp.57-58, 2005.
- [86] M. E. Motamedi, *MOEMS: micro-opto-electro-mechanical systems*, Washington: SPIE Press. 2005.
- [87] J. Singh, T. Gan, A. Agarwal, Mohanraj, and S. Liw, "3D free space thermally actuated micromirror device," *Sens. Actuators A, Phys.*, vol.123, no.4, pp.468-475, 2005
- [88] Y. Yee, H. J. Nam, S. H. Lee, J. U. Bu, Y. S. Jeon, and S. M. Cho, "PZT actuated micromirror for nano-tracking of laser beam for high-density optical data storage," in *Proc. IEEE 13th Annual Int. Conf. on MEMS*, pp.435-440, 2000
- [89] X. M. Zhang, F. S. Chau, C. Quan, Y. L. Lam, and A. Q. Liu, "A study of the static characteristics of a torsional micromirror," *Sens. Actuators A, Phys.*, vol.90, pp.73-81, 2001
- [90] J. P. Zhao, H. L. Chen, J. M. Huang, and A. Q. Liu, "A study of dynamic characteristics and simulation of MEMS torsional micromirrors," *Sens. Actuators A, Phys.*, vol.120, pp.199-210, 2005

- [91] Z. Hao, B. Wingfield, M. Whiteley, J. Brooks, and J. A. Hammer, "A design methodology for a bulk-micromachined two-dimensional electrostatic torsion micromirror," *J. Microelectromech. Syst.*, vol.12, no.5, pp.692-701, 2003
- [92] Y. Yao, X. Zhang, G. Wang, and L. Huang, "Efficient modeling of a biaxial micromirror with decoupled mechanism," *Sens. Actuators A, Phys.*, vol.120, pp.7-16, 2005
- [93] G. Zhou, F. E. H. Tay, and F. S. Chau, "Macro-modelling of a double-gimballed electrostatic torsional micromirror," *J. Micromech. Microeng.*, vol.13, pp.532-547, 2003
- [94] H. Camon, and F. Larnaudie, "Fabrication, simulation and experiment of rotating electrostatic silicon mirror with large angular deflection," in *Proc. IEEE 13th Annual Int. Conf. on MEMS*, pp.645-650, 2000
- [95] W. Cichalewski, A. Napieralski, H. Camon, and B. Estibals, "Analytical modeling and simulations of a MEMS micromirror – MATLAB implementation," in *Proc. IEEE 7th Int. Conf. CADSM*, pp.360-365, 2003
- [96] D. L. Dickensheets, and G. S. Kino, "Silicon-micromachined scanning confocal optical microscope," *J. Microelectromech. Syst.*, vol.7, no.4, pp.38-47, 1998
- [97] H. Toshiyoshi, and H. Fujita, "Electrostatic micro torsion mirrors for an optical switch matrix," *J. Microelectromech. Syst.* vol.5, no.4, pp.231-237, 1996
- [98] G. Zhu, M. Packirisamy, M. Hosseini, and Y. A. Peter, "Modelling and control of an electrostatically actuated torsional micromirror," *J. Micromech. Microeng.*, vol.16, pp.2044-2052, 2006
- [99] M. A. Hopcroft, W. D. Nix, and T. W. Kenny, "What is the Young's Modulus of silicon?" *J. Microelectromech. Syst.*, vol.19, no.2, pp.229-238, 2010
- [100] S. P. Timoshenko, and J. N. Goodier, *Theory of Elasticity*, 3rd ed. New York: McGraw-Hill. 1970.

- [101] J. Chen, W. Weingartner, A. Azarov, and R. C. Giles, "Tilt-angle stabilization of electrostatically actuated micromechanical mirrors beyond the pull-in point," *J. Microelectromech. Syst.*, vol.13, no.6, pp.988-997, 2004
- [102] O. Degani, E. Socher, A. Lipson, T. Leitner, D. J. Setter, S. Kaldor, and Y. Nemirovsky, "Pull-in study of an electrostatic torsion microactuator," *J. Microelectromech. Syst.*, vol.7, no.4, pp.373-379, 1998
- [103] Y. Nemirovsky, and O. Degani, "A methodology and model for the pull-in parameters of electrostatic actuators," *J. Microelectromech. Syst.*, vol.10, no.4, pp.601-615, 2001
- [104] Z. Xiao, W. Peng, X. T. Wu, and K. R. Farmer, "Pull-in study for round double-gimbaled electrostatic torsion actuators," *J. Micromech. Microeng.*, vol.12, pp.77-81, 2002
- [105] ANSYS Release 8.0 Document.
- [106] D. J. Inman, *Engineering Vibration*, 2nd ed. New Jersey:Prentice Hall. 2001
- [107] F. Pan, J. Kubby, E. Peeters, A. T. Tran, and S. Mukherjee, "Squeeze film damping effect on the dynamics response of a MEMS torsion mirror," *J. Micromech. Microeng.*, vol.8, pp.200-208, 1998
- [108] T.J. Brosnihan, S.A. Brown, A. Brogan, C.S. Gormley, D.J. Collins, S.J. Sherman, M. Lemkin, N.A. Polce, M.S. Davis, "Optical IMEMS-A fabrication process for MEMS optical switches with integrated on-chip electronics," in *Proc. Transducers '03, 12th Int. Conf. Solid State Sens. Actuators, and Micro-Systems*, Boston, MA, 2003, pp.1638-1642
- [109] Y. Yao, X. Zhang, G. Wang, and L. Huang, "Efficient modeling of a biaxial micromirror with decoupled mechanism," *Sens. Actuators A, Phys.*, vol.120, pp.7-16, 2005
- [110] G. K. Fedder, *Simulation of microelectromechanical systems*, Ph.D. dissertation, Eng.-Elect. Eng. Comp. Sci., California Univ., Berkeley, US, 1994

- [111] G. Barillaro, A. Molfese, A. Nannini and F. Pieri, "Analysis, simulation and relative performances of two kinds of serpentine springs," *J. Micromech. Microeng.*, vol.15, no.4, pp.736-746, 2005
- [112] S.P. Timoshenko, and J. M. Gere, *Mechanics of materials*, New York: D. Van Nostrand Company, 1972, pp. 8-11, 348-453
- [113] <http://www.on-trak.com>
- [114] J. H. Park, G. K. Garipov, J. A. Jeon, B. A. Khrenov, J. E. Kim, M. Kim, Y. K. Kim, C. H. Lee, J. Lee, G. W. Na, S. Nam, I. H. Park, and Y. S. Park, "Öbscura telescope with a MEMS micromirror array for space observation of transient luminous phenomena or fast-moving objects," *Opt. Exp.*, vol. 16, no. 25, pp.20249-20257, 2008
- [115] M. Kim, J. H. Park, J. A. Jeon, B. W. Yoo, I. H. Park and Y. K. Kim, "High fill-factor micromirror array using a self-aligned vertical comb drive actuator with two rotational axes," *J. Micromech. Microeng.*, vol.19, pp.035014(9pp), 2009
- [116] U. Krishnamoorthy, K. Li, K. Yu, D. Lee, J.P. Heritage, O. Solgaard, "Dual-mode micromirrors for optical phased array applications," *Sens. Actuators A, Phys.*, vol.97-98, pp.21-26, 2002
- [117] K. Jia, S. R. Samuelson and H. Xie, "Single-wafer solution and optical phased array application of micro-mirror arrays with high fill factor and large sub-apertures," in *Proc. IEEE 23th Int. Conf. MEMS*, Hongkong, China, pp.180-83, 2010
- [118] P. Lane, A. Dlugan, and C. MacAulay, "DMD-enabled confocal microendoscopy," in *Proc. SPIE*, vol.4251, pp.192-198, 2001
- [119] P. F. Mcmanamon, T. A. Dorschner, D. L. Corkum, L. J. Friedman, D. S. Hobbs, M. Holz, S. Liberman, H. Q. Nguyen, D. P. Resler, R. C. Sharp, and E. A. Watson, "Optical phased array technology," in *Proc. IEEE*, vol.84, no.2, 1996

- [120] W. Jung, U. Krishnamoorthy, and O. Solgaard, "High fill-factor two-axis gimbaled tip-tilt-piston micromirror array actuated by self-aligned vertical electrostatic combdrives," *J. Microelectromech. Syst.*, vol. 15, no. 3, pp.563-71, 2006
- [121] G. J. Burger, E. J. T. Smulders, J. W. Berenschot, T. S. J. Lammerink, J. H. J. Fluitman, S. Imai, "High-resolution shadow-mask patterning in deep holes and its application to an electrical wafer feed-through," *Sens. Actuators A, Phys.*, vol.54, pp.669-73, 1996
- [122] M. Minsky, "Microscopy Apparatus," *U.S. Patent*, 301467, 1961
- [123] J. T. Soini, M. Schrader, P. E. Hanninen, and S. W. Hell, "Image formation and data acquisition in a stage scanning 4Pi confocal fluorescence microscope," *Appl. Opt.*, vol.36, no.34, pp.8929-8934, 1997
- [124] W. Denk, J. H. Strickler, and W. W. Webb, "Two-photon laser scanning fluorescence microscopy," *Science*, vol.248, no. 4951, pp.73-76, 1990
- [125] C. L. Hoy, N. J. Durr, P. Chen, W. Piyawattanametha, H. Ra, O. Solgaard, and A. B. Yakar, "Miniaturized probe for femtosecond laser microsurgery and two-photon imaging," *Opt. Exp.*, vol.16, no.13, pp.9996-10005, 2008
- [126] W. Piyawattanametha, R. P. J. Barretto, T. H. Ko, B. A. Flusberg, and E. D. Cocker, "Fast-scanning two-photon fluorescence imaging based on a microelectromechanical systems two-dimensional scanning mirror," *Opt. Lett.*, vol.31, no.13, pp.2018-20, 2006
- [127] H. Miyajima, M. Nishio, Y. Kamiya, M. Ogata, Y. Sakai, and H. Inoue, "Development of two dimensional scanner-on-scanner for confocal laser scanning microscope 'LEXT' Series," in *Proc. IEEE/LEOS Int. Conf. on Optical MEMS and Their Applications*, pp.23-24, 2005
- [128] <http://www.olympusfluoview.com/theory/index.html>

- [129] H. Ra, W. Piyawattanametha, M. J. Mandella, P. L. Hsiung, J. Hardy, T. D. Wang, C. H. Contag, G. S. Kino, and O. Solgaard, "Three-dimensional in vivo imaging by a handheld dual-axes confocal microscope," *Opt. Exp.*, vol.16, no.10, pp.7224-32, 2008
- [130] H. J. Shin, M. C. Pierce, D. Lee, H. Ra, O. Solgaard, and R. Richards-Kortum, "Fiber optic confocal microscope using a MEMS scanner and miniature objective lens," *Opt. Exp.*, vol.15, no.15, pp.9113-9122, 2007
- [131] K. Kumar, K. Hoshino, and X. Zhang, "Handheld subcellular-resolution single-fiber confocal microscope using high-reflectivity two-axis vertical combdrive silicon microscanner," *Biomed Microdevices*, vol. ,pp.653-60, 2008
- [132] K. Kumar, R. Avritscher, Y. Wang, N. Lane, D. C. Madoff, T. Yu, J. W. Uhr, X. Zhang, "Handheld histology-equivalent sectioning laser-scanning confocal optical microscope for interventional imaging," *Biomed Microdevices*, vol.12, pp.223-33, 2010
- [133] H. Gruger, J. Knobbe, T. Egloff, M. Althaus, M. Scholles, H. Schenk, "Scanning photon microscope based on a MEMS 2D scanner mirror," in *Proc. SPIE*, vol.7208, 72080D, 2009
- [134] J. Helfmann, R. Schutz, I. Gersonde, G. Illing, "MEMS-based confocal laser scanning microscope for in vivo imaging," in *Proc. SPIE*, vol.7367, 73671P, 2009
- [135] C. L. Arrasmith, C. A. Patil, D. L. Dickensheets, A. Mahadevan-Jansen, "A MEMS based handheld confocal microscope with Raman spectroscopy for in-vivo skin cancer diagnosis," in *Proc. SPIE*, vol.7169, 71690, 2009
- [136] A. Jain and H. Xie, "Endoscopic microprobe with a LVD microlens scanner for confocal imaging," *IEEE 2006*, pp.168-9, 2006
- [137] K. C. Maitland, H. J. Shin, H. Ra, D. Lee, O. Solgaard, and R. Richards-Kortum, "Single fiber confocal microscope with a two-axis gimbaled MEMS scanner for cellular imaging," *Opt. Exp.*, vol.14, no.9, pp.8604-8612, 2006

- [138] P. Constantinou, T. Nicklee, D. W. Hedley, S. Damaskinos, and B. C. Wilson, "A high-resolution MACROscope with differential phase contrast, transmitted light, confocal fluorescence and hyperspectral capabilities for large-area tissue imaging," *IEEE J. Sel. Topics Quantum Electron.*, vol.11, no.4, pp.766-777, 2005
- [139] G. F. Marshall, *Optical Scanning*, New York: Marcel Dekker Inc. c1991

Appendices

Appendix A

Integral factor of electrode e_{I1} :

$$G_{f\alpha e11} = \iint_{S_{e11}} -y \cdot \left(\frac{\sin \theta}{\theta} \cdot \frac{1}{g - x \cos \alpha \sin \beta + y \sin \alpha} \right)^2 dx dy \quad (\text{A.1})$$

$$G_{f\beta e11} = \iint_{S_{e11}} x \cdot \left(\frac{\sin \theta}{\theta} \cdot \frac{1}{g - x \cos \alpha \sin \beta + y \sin \alpha} \right)^2 dx dy \quad (\text{A.2})$$

$$G_{fz e11} = \iint_{S_{e11}} \cos \theta \cdot \left(\frac{\sin \theta}{\theta} \cdot \frac{1}{g - x \cos \alpha \sin \beta + y \sin \alpha} \right)^2 dx dy \quad (\text{A.3})$$

Integral factor of electrode e_{I2} :

$$G_{f\alpha e12} = \iint_{S_{e12}} -y \cdot \left(\frac{\sin(\pi - \varphi)}{\pi - \varphi} \cdot \frac{1}{Le/2 - x \sin \alpha \sin \beta - y \cos \alpha} \right)^2 dx dy \quad (\text{A.4})$$

$$G_{f\beta e12} = \iint_{S_{e12}} x \cdot \left(\frac{\sin(\pi - \varphi)}{\pi - \varphi} \cdot \frac{1}{Le/2 - x \sin \alpha \sin \beta - y \cos \alpha} \right)^2 dx dy \quad (\text{A.5})$$

$$G_{fz e12} = \iint_{S_{e12}} \cos(\pi/2 - \varphi) \cdot \left(\frac{\sin(\pi - \varphi)}{\pi - \varphi} \cdot \frac{1}{Le/2 - x \sin \alpha \sin \beta - y \cos \alpha} \right)^2 dx dy \quad (\text{A.6})$$

Integral factor of electrode e_{I3} :

$$G_{f\alpha e13} = \iint_{S_{e13}} -y \cdot \left(\frac{\sin(\pi - \psi)}{\pi - \psi} \cdot \frac{1}{Le/2 - x \cos \beta} \right)^2 dx dy \quad (\text{A.7})$$

$$G_{f\beta e13} = \iint_{S_{e13}} x \cdot \left(\frac{\sin(\pi - \psi)}{\pi - \psi} \cdot \frac{1}{Le/2 - x \cos \beta} \right)^2 dx dy \quad (\text{A.8})$$

$$G_{fze13} = \iint_{Se13} \cos(\pi/2 - \psi) \cdot \left(\frac{\sin(\pi - \psi)}{\pi - \psi} \cdot \frac{1}{Le/2 - x \cos \beta} \right)^2 dx dy \quad (\text{A.9})$$

Integral factor of electrode e_{21} :

$$G_{fae21} = \iint_{Se21} -y \cdot \left(\frac{\sin \theta}{\theta} \cdot \frac{1}{g - x \cos \alpha \sin \beta + y \sin \alpha} \right)^2 dx dy \quad (\text{A.10})$$

$$G_{f\beta e21} = \iint_{Se21} x \cdot \left(\frac{\sin \theta}{\theta} \cdot \frac{1}{g - x \cos \alpha \sin \beta + y \sin \alpha} \right)^2 dx dy \quad (\text{A.11})$$

$$G_{fze21} = \iint_{Se21} \cos \theta \cdot \left(\frac{\sin \theta}{\theta} \cdot \frac{1}{g - x \cos \alpha \sin \beta + y \sin \alpha} \right)^2 dx dy \quad (\text{A.12})$$

Integral factor of electrode e_{22} :

$$G_{fae22} = \iint_{Se22} -y \cdot \left(\frac{\sin(\pi - \varphi)}{\pi - \varphi} \cdot \frac{1}{Le/2 - x \sin \alpha \sin \beta - y \cos \alpha} \right)^2 dx dy \quad (\text{A.13})$$

$$G_{f\beta e22} = \iint_{Se22} x \cdot \left(\frac{\sin(\pi - \varphi)}{\pi - \varphi} \cdot \frac{1}{Le/2 - x \sin \alpha \sin \beta - y \cos \alpha} \right)^2 dx dy \quad (\text{A.14})$$

$$G_{fze22} = \iint_{Se22} \cos(\pi/2 - \varphi) \cdot \left(\frac{\sin(\pi - \varphi)}{\pi - \varphi} \cdot \frac{1}{Le/2 - x \sin \alpha \sin \beta - y \cos \alpha} \right)^2 dx dy \quad (\text{A.15})$$

Integral factor of electrode e_{23} :

$$G_{fae23} = \iint_{Se23} -y \cdot \left(\frac{\sin \psi}{\psi} \cdot \frac{1}{Le/2 + x \cos \beta} \right)^2 dx dy \quad (\text{A.16})$$

$$G_{f\beta e23} = \iint_{Se23} x \cdot \left(\frac{\sin \psi}{\psi} \cdot \frac{1}{Le/2 + x \cos \beta} \right)^2 dx dy \quad (\text{A.17})$$

$$G_{fze23} = \iint_{Se23} \cos(\pi/2 - \psi) \cdot \left(\frac{\sin \psi}{\psi} \cdot \frac{1}{Le/2 + x \cos \beta} \right)^2 dx dy \quad (\text{A.18})$$

Integral factor of electrode e_{31} :

$$G_{fae31} = \iint_{Se31} -y \cdot \left(\frac{\sin \theta}{\theta} \cdot \frac{1}{g - x \cos \alpha \sin \beta + y \sin \alpha} \right)^2 dx dy \quad (\text{A.19})$$

$$G_{f\beta e31} = \iint_{Se31} x \cdot \left(\frac{\sin \theta}{\theta} \cdot \frac{1}{g - x \cos \alpha \sin \beta + y \sin \alpha} \right)^2 dx dy \quad (\text{A.20})$$

$$G_{fze31} = \iint_{Se31} \cos \theta \cdot \left(\frac{\sin \theta}{\theta} \cdot \frac{1}{g - x \cos \alpha \sin \beta + y \sin \alpha} \right)^2 dx dy \quad (\text{A.21})$$

Integral factor of electrode e_{32} :

$$G_{fae32} = \iint_{Se32} -y \cdot \left(\frac{\sin \varphi}{\varphi} \cdot \frac{1}{Le / 2 + x \sin \alpha \sin \beta + y \cos \alpha} \right)^2 dx dy \quad (\text{A.22})$$

$$G_{f\beta e32} = \iint_{Se32} x \cdot \left(\frac{\sin \varphi}{\varphi} \cdot \frac{1}{Le / 2 + x \sin \alpha \sin \beta + y \cos \alpha} \right)^2 dx dy \quad (\text{A.23})$$

$$G_{fze32} = \iint_{Se32} \cos(\pi / 2 - \varphi) \cdot \left(\frac{\sin \varphi}{\varphi} \cdot \frac{1}{Le / 2 + x \sin \alpha \sin \beta + y \cos \alpha} \right)^2 dx dy \quad (\text{A.24})$$

Integral factor of electrode e_{33} :

$$G_{fae33} = \iint_{Se33} -y \cdot \left(\frac{\sin \psi}{\psi} \cdot \frac{1}{Le / 2 + x \cos \beta} \right)^2 dx dy \quad (\text{A.25})$$

$$G_{f\beta e33} = \iint_{Se33} x \cdot \left(\frac{\sin \psi}{\psi} \cdot \frac{1}{Le / 2 + x \cos \beta} \right)^2 dx dy \quad (\text{A.26})$$

$$G_{fze33} = \iint_{Se33} \cos(\pi / 2 - \psi) \cdot \left(\frac{\sin \psi}{\psi} \cdot \frac{1}{Le / 2 + x \cos \beta} \right)^2 dx dy \quad (\text{A.27})$$

Integral factor of electrode e_{41} :

$$G_{fae41} = \iint_{Se41} -y \cdot \left(\frac{\sin \theta}{\theta} \cdot \frac{1}{g - x \cos \alpha \sin \beta + y \sin \alpha} \right)^2 dx dy \quad (\text{A.28})$$

$$G_{f\beta e41} = \iint_{Se41} x \cdot \left(\frac{\sin \theta}{\theta} \cdot \frac{1}{g - x \cos \alpha \sin \beta + y \sin \alpha} \right)^2 dx dy \quad (\text{A.29})$$

$$G_{fZe41} = \iint_{Se41} \cos \theta \cdot \left(\frac{\sin \theta}{\theta} \cdot \frac{1}{g - x \cos \alpha \sin \beta + y \sin \alpha} \right)^2 dx dy \quad (\text{A.30})$$

Integral factor of electrode e_{42} :

$$G_{f\alpha e42} = \iint_{Se42} -y \cdot \left(\frac{\sin \varphi}{\varphi} \cdot \frac{1}{Le/2 + x \sin \alpha \sin \beta + y \cos \alpha} \right)^2 dx dy \quad (\text{A.31})$$

$$G_{f\beta e42} = \iint_{Se42} x \cdot \left(\frac{\sin \varphi}{\varphi} \cdot \frac{1}{Le/2 + x \sin \alpha \sin \beta + y \cos \alpha} \right)^2 dx dy \quad (\text{A.32})$$

$$G_{fZe42} = \iint_{Se42} \cos(\pi/2 - \varphi) \cdot \left(\frac{\sin \varphi}{\varphi} \cdot \frac{1}{Le/2 + x \sin \alpha \sin \beta + y \cos \alpha} \right)^2 dx dy \quad (\text{A.33})$$

Integral factor of electrode e_{43} :

$$G_{f\alpha e43} = \iint_{Se43} -y \cdot \left(\frac{\sin(\pi - \psi)}{\pi - \psi} \cdot \frac{1}{Le/2 - x \cos \beta} \right)^2 dx dy \quad (\text{A.34})$$

$$G_{f\beta e43} = \iint_{Se43} x \cdot \left(\frac{\sin(\pi - \psi)}{\pi - \psi} \cdot \frac{1}{Le/2 - x \cos \beta} \right)^2 dx dy \quad (\text{A.35})$$

$$G_{fZe43} = \iint_{Se43} \cos(\pi/2 - \psi) \cdot \left(\frac{\sin(\pi - \psi)}{\pi - \psi} \cdot \frac{1}{Le/2 - x \cos \beta} \right)^2 dx dy \quad (\text{A.36})$$